Physics - Department

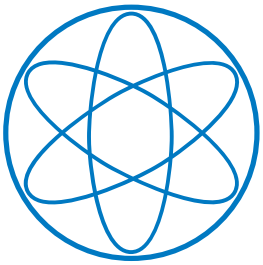

Optimisation of Transition Edge Sensors and Development of Novel Detector Designs to Enhance CRESST Dark Matter Sensitivity

PhD Thesis

by

Francesca Pucci

Technische Universität München
TUM School of Natural Sciences

Optimisation of Transition Edge Sensors and Development of Novel Detector Designs to Enhance CRESST Dark Matter Sensitivity

Francesca Pucci

Vollständiger Abdruck der von der TUM School of Natural Sciences der Technischen Universität München zur Erlangung einer Doktorin der Naturwissenschaften (Dr. rer. nat.) genehmigten Dissertation.

Vorsitz:
Prof. Dr. Björn Garbrecht

Prüfende der Dissertation:
1. Prof. Dr. Stefan Schönert
2. Priv.-Doz. Dr. Bela Majorovits

Die Dissertation wurde am 02.07.2024 bei der Technischen Universität München eingereicht und durch die TUM School of Natural Sciences am 26.09.2024 angenommen.

Abstract

Over the past century, scientists have collected numerous pieces of evidence pointing towards the existence of dark matter and have proposed several models to account for them. These findings have driven an unprecedented experimental effort to uncover the nature of dark matter. These experiments can be broadly divided into three main categories: direct detection, indirect detection and collider experiments.
Direct detection experiments seek to observe interactions between dark matter particles and standard model particles within the controlled environment of an experiment. The CRESST experiment aims at directly detecting dark matter particles through their scattering off a target nuclei in cryogenic calorimeters operated at around 15 mK. These calorimeters consist of a scintillating absorber crystal equipped with a tungsten Transition Edge Sensor (W-TES) coupled to an auxiliary crystal, also equipped with a W-TES, used to detect the scintillation light. Cryogenic calorimeters are particularly effective in probing dark matter particles with sub-GeV masses, and currently, CRESST provides the best sensitivity to this mass range under standard assumptions. This thesis explores various ways to enhance the sensitivity of the CRESST experiment.
Chapter 1 provides an introduction to dark matter, and chapter 2 delves into the principles and techniques of direct detection. Chapter 3 describes the CRESST experiment in detail, while chapter 4 explains the working principles of the W-TES.
In chapter 5, the focus is on optimising the design of W-TES, particularly the phonon collectors. The study suggests that the TES sensitivity can be improved by modifying the present design.
Chapter 6 investigates sputtering as a method for mass-producing W-TES in anticipation of the upcoming CRESST upgrade. In this upgrade, the number of readout channels will be increased to 288, leading to an increase in the number of detectors from $\mathcal{O}(10)$ to $\mathcal{O}(100)$. This work establishes a reliable procedure for producing superconducting tungsten thin films on various substrate materials.
Chapter 7 addresses the Low Energy Excess (LEE), the major limitation to the sensitivity of many low-mass dark matter direct detection experiments. It provides an overview of the insight gained by the CRESST collaboration and introduces the doubleTES, a novel detector module designed to investigate the LEE. Results from above-ground measurement campaigns demonstrate the doubleTES detectors' ability to distinguish

events originating in the bulk of the target crystal and events originating in close proximity to the sensors.

Zusammenfassung

Im Laufe des letzten Jahrhunderts haben Wissenschaftler zahlreiche Beweise für die Existenz dunkler Materie gesammelt und mehrere Modelle vorgeschlagen, um sie zu erklären. Diese Erkenntnisse haben zu einer beispiellosen experimentellen Anstrengung geführt, um die Natur der dunklen Materie zu ergründen. Diese Experimente lassen sich grob in drei Hauptkategorien einteilen: direkter Nachweis, indirekter Nachweis und Beschleuniger-Experimente.
Bei Experimenten zum direkten Nachweis wird versucht, die Wechselwirkungen zwischen Teilchen der dunklen Materie und Teilchen des Standardmodells in der kontrollierten Umgebung eines Experiments zu beobachten. Das CRESST-Experiment zielt auf den direkten Nachweis von Teilchen der dunklen Materie durch deren Streuung an einem Atomkern in kryogenen Kalorimetern, die bei etwa 15 mK betrieben werden. Diese Kalorimeter bestehen aus einem szintillierenden Absorberkristall, der mit einem Wolfram-Übergangskantensensor (W-TES) ausgestattet wird. Ein zweiter Kristall, ebenfalls mit einem W-TES ausgestattet, dient zum Nachweis des Szintillationslichts. Kryogene Kalorimeter sind besonders effektiv bei der Suche nach dunklen Materie mit Massen unterhalb des GeV-Bereichs, und derzeit bietet CRESST unter Standardannahmen die beste Empfindlichkeit für diesen Massenbereich.
In dieser Arbeit werden verschiedene Möglichkeiten zur Verbesserung der Empfindlichkeit des CRESST-Experiments untersucht.
Kapitel 1 bietet eine Einführung in die dunkle Materie, und Kapitel 2 befasst sich mit den Prinzipien und Techniken des direkten Nachweises. Kapitel 3 beschreibt das CRESST-Experiment im Detail, während Kapitel 4 die Funktionsprinzipien des W-TES erklärt.
In Kapitel 5 liegt der Schwerpunkt auf der Optimierung des Designs von W-TES, insbesondere der Phononenkollektoren. Die Studie legt nahe, dass die TES-Empfindlichkeit durch eine Änderung des derzeitigen Designs verbessert werden kann.
Kapitel 6 untersucht das Sputtern als Methode für die Massenproduktion von W-TES im Hinblick auf das bevorstehende CRESST-Upgrade. Bei diesem Upgrade wird die Anzahl der Auslesekanäle auf 288 erhöht, was zu einer Erhöhung der Anzahl der Detektoren von $\mathcal{O}(10)$ auf $\mathcal{O}(100)$ führt. Diese Arbeit etabliert ein zuverlässiges Verfahren zur Herstellung supraleitender Wolfram-Dünnschichten auf verschiedenen Substratmaterialien.

Kapitel 7 befasst sich mit dem Low Energy Excess (LEE), der größten Einschränkung der Empfindlichkeit vieler Experimente zum direkten Nachweis massearmer dunkler Materie. Es gibt einen Überblick über die von der CRESST-Kollaboration gewonnenen Erkenntnisse und stellt den doubleTES vor, ein neuartiges Detektormodul, das zur Erforschung des LEE entwickelt wurde. Die Ergebnisse von oberirdischen Messkampagnen zeigen, dass die doubleTES-Detektoren in der Lage sind, zwischen Ereignissen, die in der Hauptteil des Zielkristalls entstehen, und Ereignissen, die in unmittelbarer Nähe der Sensoren entstehen, zu unterscheiden.

“C’è un’ape che se posa
su un bottone de rosa:
lo succhia e se ne va...
Tutto sommato, la felicità
è una piccola cosa."

— Trilussa

Contents

1 Introduction to Dark Matter **1**
1.1 Evidences for Dark Matter . . . 1
1.1.1 Coma Cluster . . . 1
1.1.2 Rotation velocity of Spiral Galaxies . . . 2
1.1.3 Bullet Cluster . . . 3
1.1.4 Cosmic Microwave Background . . . 5
1.2 Structure Formation . . . 7
1.3 Dark Matter Candidates . . . 8
1.3.1 Thermal Production . . . 9
1.3.2 Non-thermal production . . . 10

2 Dark Matter Searches **11**
2.1 Detection Techniques . . . 11
2.1.1 Collider Searches . . . 12
2.1.2 Indirect Searches . . . 12
2.1.3 Direct Searches . . . 13
2.2 Direct Dark Matter Detection . . . 13
2.2.1 Dark Matter Distribution in the Milky Way . . . 14
2.2.2 Detection Principles and Interactions . . . 14
2.2.3 Detection Challenges . . . 18
2.3 Experimental Approaches . . . 20
2.3.1 Ionisation Signal . . . 20
2.3.2 Light Signal . . . 22
2.3.3 Heat signal . . . 23
2.4 Current Status . . . 23

3 The CRESST experiment **25**
3.1 Experimental setup . . . 25
3.1.1 Shieldings . . . 25
3.1.2 Cryostat . . . 29
3.2 CRESST Phases . . . 29
3.2.1 CRESST-III Detector Modules . . . 30

3.2.2 CRESST-III Results . . . 32
3.2.3 Future plans . . . 33

4 Transition edge sensors for dark matter searches 35
4.1 Cryogenic calorimeters . . . 35
4.1.1 Transition edge sensors . . . 36
4.2 Detector Thermal Model . . . 37
4.2.1 Heat Capacities . . . 37
4.2.2 Phonon Populations . . . 39
4.2.3 Thermal Couplings . . . 40
4.2.4 Signal Formation . . . 42
4.2.5 Phonon Collectors . . . 46
4.3 SQUID readout . . . 48
4.4 Noise . . . 49

5 Optimisation of CRESST sensor design 51
5.1 Motivation . . . 51
5.2 Standard CRESST sensor . . . 52
5.3 Experimental Procedure . . . 54
5.4 R&D on optimisation of new sensor designs . . . 55
5.4.1 Phonon Collectors Thickness . . . 56
5.4.2 Phonon Collectors Architecture . . . 59
5.4.3 Magnetic Shield on Phonon Collectors . . . 66
5.5 Conclusions . . . 70

6 Sputtering the W-TES 71
6.1 Motivation . . . 71
6.1.1 The CRESST Upgrade . . . 71
6.1.2 TES Evaporation . . . 72
6.2 Tungsten Superconductivitity . . . 74
6.3 W-TES Production via Magnetron Sputtering . . . 77
6.3.1 The DC Magnetron Sputtering Process . . . 78
6.3.2 Previous Results . . . 79
6.4 Sputter Machine 581 . . . 79
6.4.1 Commissioning . . . 82
6.4.2 Experimental Procedure . . . 82
6.4.3 Characterisation and Results . . . 83
6.4.4 Stress on W thin films . . . 87
6.5 Conclusions and Outlook . . . 88

7 The doubleTES **91**
7.1 Motivation . . . 91
7.1.1 The Hunt for Low Energy Excess . . . 92
7.2 DoubleTES Detector Module . . . 96
7.2.1 Description . . . 96
7.2.2 Production details . . . 96
7.3 Data Analysis . . . 98
7.3.1 Trigger . . . 100
7.3.2 Pulse Parameter Calculation . . . 100
7.3.3 Threshold Estimation . . . 101
7.3.4 Working Point Cut . . . 102
7.3.5 Quality Cuts . . . 103
7.3.6 Energy Calibration . . . 104
7.3.7 Absorber Events Cut . . . 106
7.3.8 Survival Probability . . . 106
7.4 $CaWO_4$ doubleTES . . . 107
7.4.1 Experimental set-up . . . 107
7.4.2 Measurements . . . 108
7.4.3 Thermal Analysis . . . 109
7.4.4 Performance Studies and Results . . . 115
7.4.5 Conclusions . . . 131
7.5 Silicon-on-sapphire doubleTES . . . 131
7.5.1 Design and Motivation . . . 131
7.5.2 Experimental set-up . . . 132
7.5.3 Test Results . . . 132
7.5.4 Conclusions . . . 141
7.6 Underground Measurement and Outlook . . . 142

8 Conclusions and Outlook **145**

Bibliography **147**

Chapter 1

Introduction to Dark Matter

The term "dark matter" denotes a type of matter that does not absorb, reflect or emit light, yet it is influenced by gravity.
This component of our Universe is currently the subject of an unprecedented experimental effort to unveil its nature. Since the 1930s, scientists have collected various pieces of evidence in favour of its existence and proposed several models to account for them.
Based on these observations, scientists estimate that dark matter constitutes 26% of the total energy density of the Universe and that it should have existed for much of the lifetime of the Universe. Many more characteristics of dark matter have been inferred from these observations based on the Standard Cosmological Model. This chapter will present evidence supporting dark matter's existence, furthering our comprehension of the Universe based on the Standard Cosmological Model. An overview of potential mechanisms of dark matter production in the early Universe, along with a short discussion on possible candidates, will conclude this chapter.

1.1 Evidences for Dark Matter

This section will present some of the evidence collected for the existence of dark matter. We will first jump back to 1933 to explore the earliest hints of something unknown in the Universe. Following that, we will move to the second milestone - the studies of galaxies' rotation curves in the 1970s. We will then bring our attention to the critical observation of the Bullet Cluster's behaviour from 2006. Lastly, we will briefly outline the constraints from the cosmic microwave background.

1.1.1 Coma Cluster

During the 1920s-1930s, a number of scientists began to contemplate the existence of dark matter, making it challenging to pinpoint the first appearance of such a concept.

In 1933, Swiss astrophysicist Fritz Zwicky published a paper containing the first piece of evidence for dark matter [1]. His work aimed to measure the mass of the Coma galaxy cluster. Zwicky employed two distinct methods to confirm his findings, seeking to strengthen his results through cross-validation. The first method involved observing the cluster and measuring its luminosity to deduce its mass. Examining nearby stellar systems, he determined the calibration of mass per unit of light. Using this approach, Zwicky estimated the total mass of the Coma galaxy cluster to be $M_{Coma} = 800 \cdot 10^9\, M_{Sun} \sim 1.6 \cdot 10^{45}\, g$.
The second approach began with the premise that gravity depends on the cluster's mass. Assuming the cluster to be at equilibrium, it is possible to apply the viral theorem, which relates kinetic energy (E_{kin}) and potential energy (E_{pot}) through $E_{kin} = -1/2\, E_{pot}$. The kinetic energy of the cluster was determined by analysing the velocities of particles within it. Then, the total mass could be inferred through the equation:

$$M = \frac{5}{3}\frac{\langle v^2 \rangle R}{G} \tag{1.1}$$

The estimation of $\langle v \rangle$ was derived from the Doppler shift radiation of eight galaxies in the cluster, yielding a velocity dispersion. Zwicky obtained an average velocity of 1019 km/s, which is relatively accurate, given that current measurements provide $\langle v \rangle$=1082 km/s [2]. Employing this second method, Zwicky obtained a total mass of $M_{Coma} = 3 \cdot 10^{47}\, g$ for the Coma cluster.
Combining his observations [1, 3], Zwicky noted a discrepancy of two orders of magnitude between the masses obtained from the two methods. Remarkably, the discrepancy holds today, even though reduced to a factor 50 only (to compare with the factor 200 obtained by Zwicky), because of some errors in Zwicky's first method of computing the Coma cluster mass.
One way to resolve this discrepancy is by postulating that an important portion of the gravitational mass was not accounted for when considering luminous matter.

1.1.2 Rotation velocity of Spiral Galaxies

During the 1970s, some scientists directed their focus towards the investigation of the rotational velocity dispersions of spiral galaxies.
As most of a galaxy's luminous mass is located at its centre, at large distances from the galactic centre, we anticipate its gravitational potential to scale inversely with the distance. Thus, according to Kepler's third law of motion, stars at large distances from the galactic centre should orbit around it with a velocity that scales inversely with the square root of their distance from the centre ($v \propto 1/\sqrt{r}$). Figure 1.1 depicts the expected rotational velocity curve.

Extensive studies of the rotational velocity curves of several spiral galaxies from the group of Vera Rubin, Kent Ford and Norbert Thonnard [5–7] revealed a strikingly different behaviour. Contrary to expectations, the rotational velocity of galaxies does

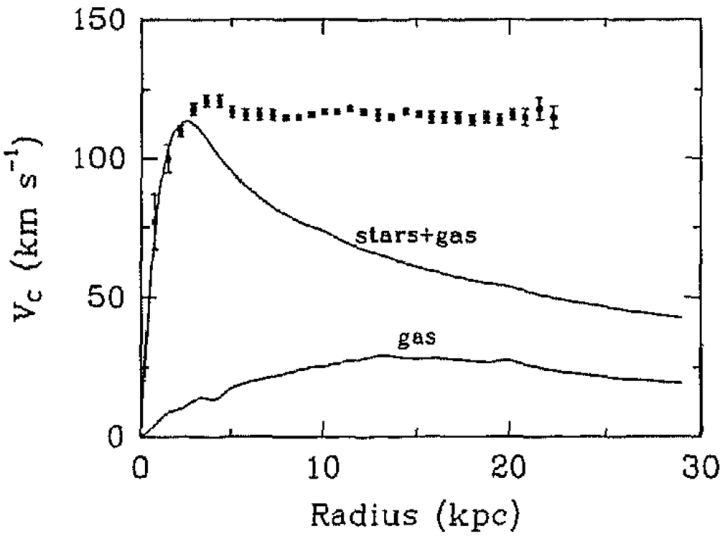

Figure 1.1: Representation of the problem of galaxy rotational curves. Here, the observed rotational velocity curve of the NGC 6503 galaxy is plotted (dots) together with the curves predicted for the gas and stars components and the gas component only. Image taken from [4].

not drop off beyond the galaxy bulge. Instead, it maintains a relatively constant velocity up to distances well beyond the galactic centre. Figure 1.2 illustrates the observed rotation curves of multiple galaxies.

These flat rotation curves might imply that $M(r) \propto r$ even outside the radius of the galactic bulge, where the luminous matter predominantly resides, thus suggesting the existence of a "dark halo" extending beyond the stellar distribution [8]. The hypothesis of the existence of a dark halo still holds, with galaxies believed to be embedded in an extended halo of dark matter stretching far beyond visible matter. The density profiles of these extended halos are derived from simulations of collisionless dark matter (NFW [9] or Einasto [10] are widely used models).

Another way of explaining the observed rotational velocity dispersions of spiral galaxies is assuming that Newtonian gravity does not describe such vast systems (moving with an acceleration smaller than $1.2{\cdot}10^{-10}\,\mathrm{m/s^2}$) and must be modified accordingly. A description of this possibility is beyond the scope of this thesis and can be found in [11].

1.1.3 Bullet Cluster

All systems studied so far represent equilibrium systems, where both baryonic and dark matter have reached thermal equilibrium. An excellent example of a non-equilibrium

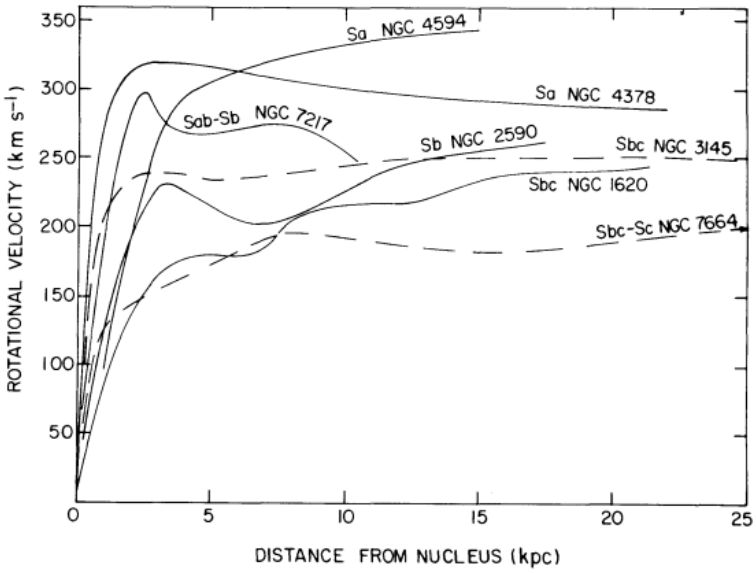

Figure 1.2: Observed rotational velocity curves for seven galaxies. Image taken from [6].

system is a collision of clusters, such as the Bullet cluster.
The 1E 0657-56 galaxy cluster (also known as Bullet cluster) is a new cluster formed by the collision of two large clusters. As two galaxy clusters collide, their gas clouds interact, leading to mutual heating and deceleration of their motion. On the other hand, the stars in the two clusters are compact objects, which minimises the probability of interaction and allows them to continue their motion. As a result, the gas is slowed down with respect to the stars, which instead continue their motion.
In the observation of the Bullet cluster, the gas distribution was identified through its emission of X-rays. Subsequently, gravitational lensing techniques were utilised to map out the gravitational field and thus infer the mass distribution. These investigations revealed a mass distribution aligned with the stellar distribution. A picture of the Bullet cluster highlighting the different populations observed is provided in Figure 1.3.
As for the rotational curves of spiral galaxies, we can assume a scenario where a large dark matter halo surrounds each cluster to explain this observation. Since the observed mass distribution is coherent with the stellar distribution, we hypothesise that dark matter is collisionless. Under this hypothesis, these two halos would pass through each other, influenced solely by the gravitational pull of the other cluster. Thus, dark matter would continue its motion, along with the stars, while the gas remains behind.
In light of this, when physicists observed the Bullet cluster in 2006 [13], they referred to it as the "first direct empirical proof of the existence of dark matter". Furthermore, the Bullet cluster observation provides insights into the potential self-interaction of

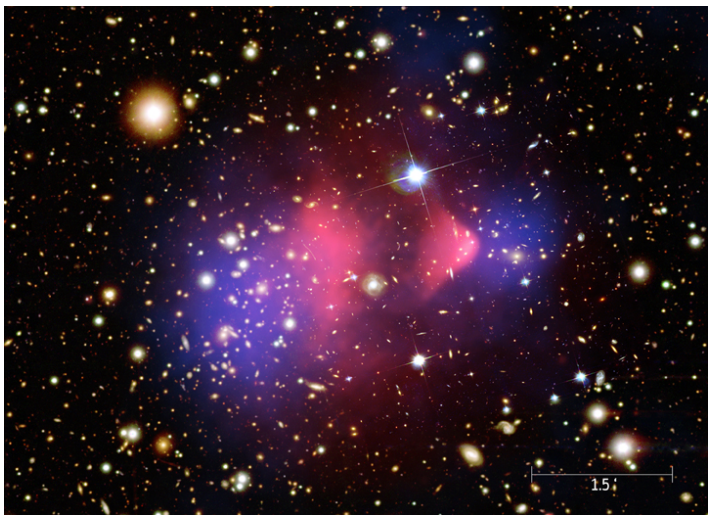

Figure 1.3: The Bullet cluster. This figure contains three superimposed pictures. The first layer is the optical image representing the distribution of stars. The second layer is the hot gas distribution, inferred through X-rays and represented in pink. The third layer represents the gravitational potential, obtained with gravitational lensing techniques and represented in blue. Image taken from [12].

dark matter. Self-interactions would have led to a deceleration of the motion of the halos, allowing to place constraints on such interactions. Recent studies have permitted self-interaction rates up to $\sigma/m \sim 2\,cm^2/g$ [14].

1.1.4 Cosmic Microwave Background

Another striking evidence supporting the presence of dark matter in the Universe stems from observations of the very early Universe, mainly through the cosmic microwave background (CMB). Experiments studying the CMB started providing results pointing towards the existence of dark matter in the early 2000s and allowed the constraining of the fraction of the Universe made of dark matter in 2018.
To comprehend the CMB observations, a brief review of the thermal history of the Universe is essential.

Short Thermal History of the Universe

By examining the early Universe, we can infer constraints on the amount of matter and radiation present in the Universe. Particularly, we can relate the present abundance of baryons to information from the Big Bang Nucleosynthesis (BBN), and we can constrain the amount of radiation in the early Universe through the epoch of Recombination [15].

BBN: BBN initiates when the temperature of the Universe (T_{Uni}) drops to $T_{Uni} \approx 1\,\text{MeV}$. Before this temperature is reached, the proton and neutrons are in thermal equilibrium. When this temperature is reached, instead, protons cannot decay into neutrons anymore. [16] When the temperature of the Universe drops well below the deuterium binding energy, approximately when $T_{Uni} \approx 100\,\text{keV}$, light elements such as deuterium and helium are synthesised. By examining the present abundance of these light elements, constraints on the ratio between the number of protons and neutrons (n_p/n_n), as well as between the number of baryons and photons (n_b/n_γ), can be established [17]. Notably, the latter is related to the baryonic density in the Universe (Ω_b) via:

$$\frac{n_b}{n_\gamma} = \frac{\rho_c}{\langle m \rangle n_\gamma^0} \Omega_b \tag{1.2}$$

where ρ_c denotes the critical density of the Universe, $\langle m \rangle$ represents the mean mass per baryon (i.e. approximately the proton mass) and n_γ^0 is the present day photon number density [17].

Recombination: Recombination denotes the epoch when hydrogen atoms begin to form through the combination of electrons and protons. This era begins when $T_{Uni} \sim 0.4\,\text{eV}$ [18]. During this phase, the Universe transitions from being an ionised plasma to being neutral. Consequently, photons, which scatter very efficiently off charged particles but not nearly as efficiently off neutral particles, can freely stream in the Universe, leading to what is known as the "surface of last scattering", when $T_{Uni} \sim 0.1\,\text{eV}$. At this temperature, the high energy tail of photons falls below 13.6 eV (the hydrogen atoms binding energy) and almost all of the electrons have recombined. The CMB provides a snapshot of the Universe at this surface [19].

The CMB temperature landscape is a picture of the density landscape of the Universe at the surface of last scattering (see Figure 1.4). It exhibits small perturbations seeded by inflationary processes. These density fluctuations oscillate over time, influenced by the competing effects of gravity and radiation pressure [20]. Gravity tends to increase the density of overdense regions in the plasma, attracting more matter towards them. Conversely, radiation pressure pushes particles, tightly coupled to a photon field, away from each other, leading to a decrease in density.
The CMB offers a glimpse into these fluctuations when the Universe was just a few hundred thousand years old (at a redshift of 1000). These fluctuations can only be explained with a matter component that experiences gravity but not radiation pressure. This matter component should be approximately five times larger than the baryonic matter component. Hence, the CMB anisotropy stands as compelling evidence for the existence of dark matter, indicating that it has existed since the early Universe.

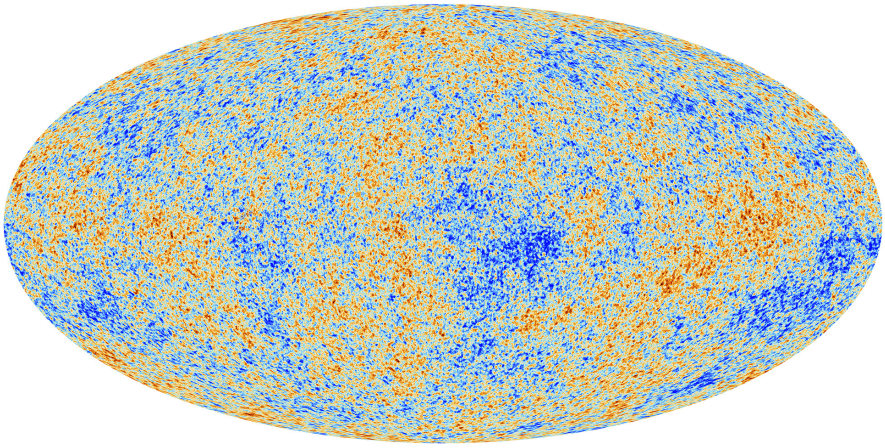

Figure 1.4: Image of the anisotropies of the CMB seen by the European Space Agency's (ESA) Planck mission, ©ESA. The picture shows temperature fluctuations on the surface of last scattering, corresponding to regions of slightly different densities. These regions represent the seeds of all future structures: the stars and galaxies of today. The image is obtained from the 2018 Planck data [21].

The 2018 analysis of the Planck experiment [21] allowed for the constraint of the fraction of the Universe in its radiation (Ω_{rad}), matter (Ω_m) and dark energy (Ω_Λ) components:

$$\begin{aligned} \Omega_{rad} &= 9 \cdot 10^{-4} \\ \Omega_m &= 0.3153 \pm 0.0073 \\ \Omega_\Lambda &= 0.6847 \pm 0.0073 \end{aligned} \tag{1.3}$$

The radiation fraction of the Universe is precisely known, as the temperature of the blackbody radiation is accurately measured. The density of matter consists of baryonic matter, for which $\Omega_b \sim 0.049$ and dark matter, for which $\Omega_{DM} \sim 0.266$. The determination of the matter fraction in the Universe was achieved by combining the Planck data with gravitational lensing information.

1.2 Structure Formation

Understanding the formation of structures in the Universe, such as galaxies and clusters, is crucial for unveiling the nature of dark matter. Dark matter, being the dominant matter component, accrete first, with baryonic matter subsequently falling into the formed gravitational potential wells. The structure formation mechanism holds valuable information regarding the velocity of dark matter particles when they decouple [22].

N-body simulations are conducted to study this phenomenon. These simulations explore two limiting scenarios: relativistic and non-relativistic dark matter cases.

Hot Dark Matter Dark matter is relativistic and can freely stream throughout the Universe when it decouples from the Standard Model at the surface of last scattering. At this stage, the particles possess too much kinetic energy to accrete into small structures. Instead, they form large structures first, subsequently fragmenting to create smaller ones. This process is known as "top-down" structure formation [23].

Cold Darm Matter Dark matter remains non-relativistic throughout all relevant epochs for structure formation. Its slow movement allows it to easily form small clumps, as its kinetic energy is smaller than the potential energy of even small bound structures. Consequently, small clumps form first and subsequently accrete into larger structures. This process is known as the "bottom-up" scenario [22]. In this scenario, small relic overdense regions within larger dark matter halos should persist today.

Currently, comparisons between N-body simulations and observational data on the abundance of small-scale structures in the Universe favour the cold dark matter scenario, characterised by bottom-up structure formation [24, 25].

1.3 Dark Matter Candidates

The evidence presented so far suggests the existence of a new type of matter, the nature of which remains unknown. Despite this, these observations have provided some insights into the properties of these particles. Firstly, they must be massive, as evidenced by their gravitational interaction. Additionally, they are likely stable or at least have very long lifetimes (longer than the age of the Universe), given their presence in both present-day rotational velocity curves and the early Universe (as observed in the CMB). Dark matter is also non-luminous, as evidenced by the absence of direct observations. Lastly, it is non-relativistic, as proved by considerations of galaxy dynamics, that allowed for an estimation of the average speed of dark matter particles.
Combining all of this information, scientists proposed various dark matter candidates, accounting for the nature and behaviour of these particles. Their possible mass spans a wide range, from $10^{-21}\,\mathrm{eV}$ [26] to the Planck mass ($\sim 10^{18}\,\mathrm{GeV}$) [27]. One way to categorise the plethora of dark matter candidates is to consider the mechanisms that led to the presence of the measured relic density of dark matter in the Universe today. These "production mechanisms" can be thermal or non-thermal. The distinction lies in whether dark matter has ever been in thermal equilibrium with the Standard Model.

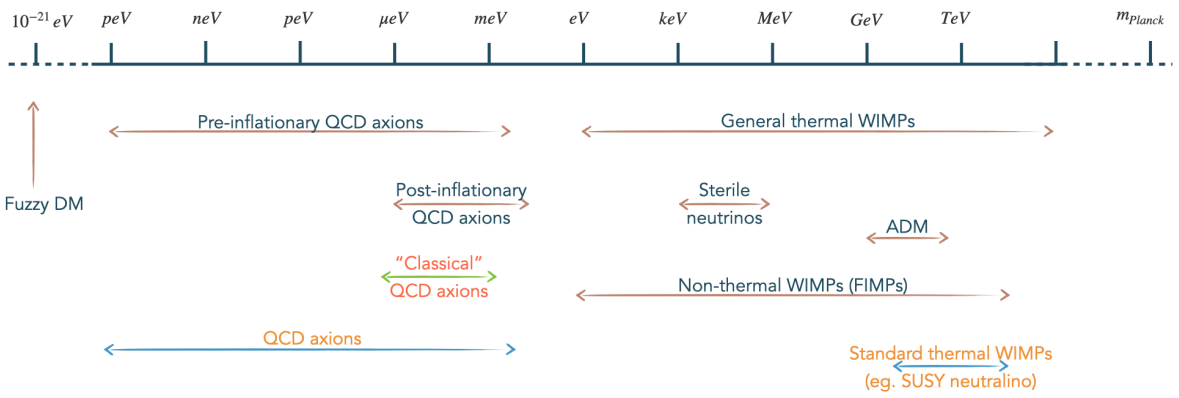

Figure 1.5: Several possible dark matter candidates in the allowed mass range. Image reproduced from [28].

1.3.1 Thermal Production

In a thermal scenario, during the early Universe, dark matter was thermally coupled to the Standard Model plasma through interactions of the form:

$$DM + DM\,(+DM...) \longleftrightarrow SM\,particles \tag{1.4}$$

These processes occurred rapidly enough to maintain thermal equilibrium in the early Universe, meaning that dark matter's annihilation and production rate were equal. This equilibrium was broken once the temperature of the Universe dropped below the dark matter mass; thus, its production could no longer persist. Consequently, the dark matter density started falling exponentially. As the Universe expanded, there came a point when the expansion rate (H) exceeded the annihilation rate (Γ). At this point, the dark matter bath decoupled from the Standard Model, and its density settled at the current abundance. This transition is known as freeze-out [29].
Freeze-out can occur whether dark matter particles are relativistic or non-relativistic. However, assuming dark matter to be a hot relic, the current abundance cannot be obtained [30]. Alternatively, assuming dark matter as a cold relic leads to the Weakly Interacting Massive Particles (WIMPs) hypothesis.

WIMPs

The search for WIMPs has been a focal point in dark matter research for several years. Their popularity stems from the so-called "WIMP miracle", which offers a potential solution to the dark matter enigma through new physics at the electroweak scale.
Assuming dark matter at the electroweak scale (i.e. $m_{DM} \approx 100\,\mathrm{GeV/c^2}$) interacting weakly with the Standard Model results in the exact relic density presently observed.

The constraints on the coupling can be relaxed, allowing the WIMPs to interact with the SM sector through any mediator, including unknown ones. This leads to a much broader possible mass range (refer to Figure 1.5), spanning from $\mathcal{O}$(eV) (constrained by freeze-out abundance [31]) to $\mathcal{O}$(100s TeV) (limited by Unitarity arguments [32]). In this context, the lighter the dark matter candidates, the weaker the coupling to the SM they possess.

While numerous other dark matter candidates have been proposed over the years [28,33], providing a comprehensive description of these possibilities is beyond the scope of this work.

1.3.2 Non-thermal production

Scientists proposed a variety of production mechanisms in the non-thermal scenario. One such possibility is the freeze-in mechanism. In this description, initially, there is either no dark matter or only a small amount of it, which is decoupled from the Standard Model plasma. In this scenario, dark matter production occurs despite the weak interaction strength between dark matter and SM particles, but no annihilation. As the temperature of the Universe drops below the mass of the dark matter particle, its abundance freezes in and remains roughly constant at its current value [34].

Another possible non-thermal production mechanism is via the spontaneous breaking of the Peccei-Quinn symmetry [35]. Proposed to solve the strong CP problem [36], this mechanism introduces the axion field that could be a dark matter candidate. This field naturally evolves towards a local minimum, solving the CP problem and allowing for an estimation of the axion mass through its coupling with the Standard Model quarks:

$$m_a \approx \frac{f_\pi m_\pi}{f_a}\left[\frac{m_u m_d}{(m_u+m_d)^2}\right]^{1/4} \approx 0.6\,meV\left(\frac{10^{10}\,GeV}{f_a}\right) \tag{1.5}$$

where m_π is the pion mass ($m_\pi \approx 135\,\text{MeV}$), f_π its effective coupling ($f_\pi \approx 93\,\text{MeV}$), m_u is the mass of the up quark ($m_u \approx 2.2\,\text{MeV}$), m_d is the mass of the down quark ($m_u \approx 4.7\,\text{MeV}$) [37] and $1/f_a$ is the axion field coupling.
The axion coupling is proportional to its mass. To allow axions to constitute 100% of the dark matter in the Universe, masses below $10^{-3}\,\text{eV}$ are required. Such small masses (which can go down to the peV scale) naturally result in very small couplings, explaining why accelerator searches could not search for axions [38].

Chapter 2

Dark Matter Searches

In the previous chapter, we delved into the evidence of the existence of dark matter. Together with the absence of observation, these findings made dark matter one of the most investigated mysteries of our times. Consequently, numerous experiments have been devised, approaching the search for dark matter from different perspectives.
These search efforts can broadly be categorised into three main types: direct detection, indirect detection and collider searches. Figure 2.1 offers a schematic overview of the different approaches.
In the initial sections of this chapter, a brief overview of these searching techniques will be provided. Subsequently, we will delve into direct detection, offering a concise explanation of the detection principles and interactions involved. Following this, we will present various experimental techniques utilised in direct detection studies. This chapter will conclude by presenting the current status of direct searches for dark matter.

2.1 Detection Techniques

Dark matter detection is extremely challenging, particularly considering that gravitational interaction is the only confirmed interaction of dark matter particles with baryonic matter. Consequently, the potential interactions of dark matter particles are highly uncertain, resulting in a vast parameter space awaiting exploration.
Various approaches exist to this search, differentiated according to the process they target for detection, as depicted in Figure 2.1. Collider searches seek to detect dark matter particles produced during the interaction of SM particles. Indirect searches intend to detect the SM products resulting from an interaction of dark matter particles. Finally, direct searches aim to observe the scattering of dark matter particles off SM particles.

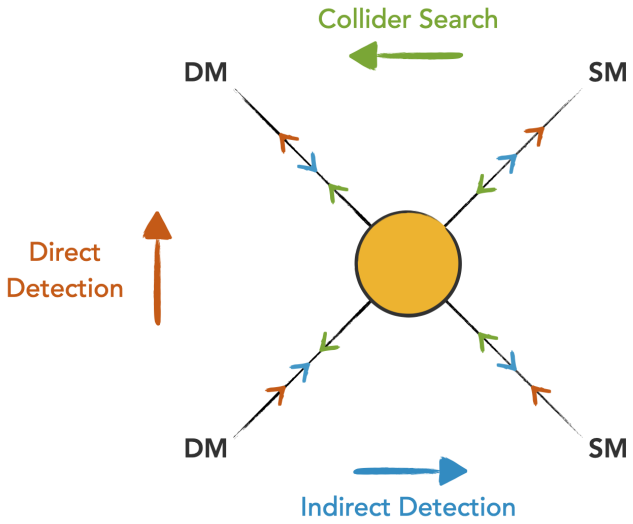

Figure 2.1: Schematic representation of the different dark matter detection techniques.

2.1.1 Collider Searches

Collider searches intend to detect dark matter by observing their production at colliders, primarily at the Large Hadron Collider (LHC) [39]. Since dark matter particles will not leave a direct signature in detectors, the focus is on studying the missing energy. Detecting this signal poses several challenges, among which two are the most prominent.

- Discovering a new particle at the LHC would represent a significant advancement in particle physics. However, such a discovery does not inherently imply that the detected particle is a dark matter candidate, and it would necessitate confirmation from different detection techniques.

- Given the limited timescales involved in these searches (up to the timescale needed to traverse the entire detector), the dark matter particles' lifetime cannot be probed.

Despite these challenges, numerous searches are ongoing at the LHC (see, e.g. [40,41]).

2.1.2 Indirect Searches

In most WIMP models, these particles' annihilation rate is comparable to the annihilation rate in the early Universe [42]. Consequently, they should generate observable SM signals if a sufficiently high dark matter density is present. Indirect searches seek

to detect the resulting SM particles or their secondary effects [43].
Gravitationally bound objects, such as galaxies or clusters, contain overdense regions where dark matter annihilation or decay can produce energetic SM particles. These regions are preferred targets for observation, as the higher density enhances the observation probability.
Indirect searches complement direct searches by offering a better reach at high masses and the ability to set constraints on the lifetime of dark matter. Additionally, searches looking for an annihilation signal can directly measure the mass of dark matter by observing the monochromatic signal resulting from their annihilation into a purely SM final state. However, interpreting an indirect signal can be challenging, as other astrophysical processes can mimic dark matter signals.
Numerous indirect searches are ongoing, mainly focusing either on detecting γ rays, cosmic rays, neutrinos, or antimatter particles [44, 45]. These searches primarily utilise telescopes, and they can be grouped according to the mass range they aim to observe:

- 100 MeV-1 TeV: space-based telescopes, such the Fermi Gamma-ray space telescope [46]
- 100 GeV-10s TeV: ground-based Cherenkov telescopes, such as MAGIC [47]
- few TeV-100s TeV: water-based Cherenkov telescopes, such as HAWC [48]

2.1.3 Direct Searches

Direct detection of dark matter involves detecting the effect of a dark matter particle coming from the galactic halo, interacting with a SM particle within the controlled environment of an experiment. In the following sections, we will delve into the principles, challenges, and potential detection techniques employed in direct searches of WIMPs. It is worth noting that the detection of axions and axion-like particles (ALPs) follows entirely different principles [49], which are beyond the scope of this thesis.

2.2 Direct Dark Matter Detection

As mentioned earlier, direct detection of dark matter poses significant challenges. To progress in this search, it is crucial to consider the fundamental principles underlying direct detection. Specifically, focus should be placed on:

- Assessing the expected rate of dark matter interactions with the detector material;
- Identifying potential sources of background signals that could be mistaken for dark matter;

- Recognise the distinctive experimental signatures indicative of dark matter interactions within the specific experimental set-up.

2.2.1 Dark Matter Distribution in the Milky Way

First, it is essential to understand the distribution of dark matter particles and their potential interaction rate to comprehend how dark matter and baryonic matter interact in a detector.
The assumption is that these particles are distributed within isothermal spherical halos, characterised by a Maxwell-Boltzmann velocity distribution [50], mathematically represented as:

$$f(v) = \frac{N}{\sqrt{\pi^{3/2} v_s^3}} e^{-v^2/(v_s^2)} \tag{2.1}$$

Where v denotes the dark matter velocity dispersion, v_s represents the velocity of the observational point in the Solar System ($v_s = 220\ km/s$), and N is a renormalisation factor. The local density of dark matter near the Earth can be computed as the average of a small volume within a few hundred parsecs of the Sun. While the commonly used value for calculations in dark matter searches corresponds to $\rho_0 = 0.3\,\mathrm{GeV/c^2}$, present studies suggest a higher local dark matter density [51].

2.2.2 Detection Principles and Interactions

The primary hypothesis of direct searches is that dark matter particles interact with SM particles not only gravitationally but also via some other interaction, often imagined as similar to the weak one. The exact nature of this interaction is not crucial for finding a signal in direct detection experiments. It should only be stronger than the gravitational one, which is too weak in an Earth-based experiment to be within detection reach.
In the following, our focus will be on nuclear scatterings of dark matter particles. Detailing all possible interaction scenarios for dark matter is beyond the scope of this thesis [52–55].

Nuclear Scattering in the Laboratory Frame

The Solar System moves in the Universe with an average velocity of approximately 220 km/s. When examining the interaction in the laboratory frame, we can consider an elastic scattering between a WIMP moving with a velocity of approximately 220 km/s and a target nucleus at rest, as depicted in Figure 2.2. This viewpoint leads the dark matter particle to be non-relativistic (with $\beta = \mathrm{v/c} \approx 7.34{\cdot}10^{-4}$).
Thus, interactions with SM particles mostly remain elastic for masses up to $\sim$1 TeV, as the dark matter particles do not possess enough energy to break the nuclei. Despite the elastic nature of the considered interactions, the potential influence of spin interactions [56] has to be accounted for. By adhering to energy and momentum conservation

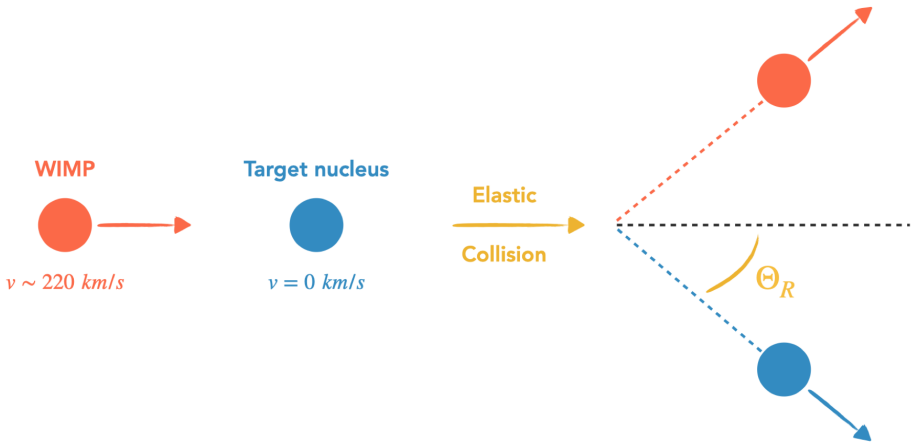

Figure 2.2: Schematic representation of a WIMP scattering off a target nuclei in the laboratory frame. Here, the target nucleus can be considered at rest while the WIMP moves towards it with the average velocity of dark matter in the Milky Way.

principles, the maximum energy transfer to the recoiling nucleus can be determined as follows:

$$E_R^{max} = 2 \cdot \frac{\mu^2 v^2}{m_T} \tag{2.2}$$

where μ denotes the reduced mass of the system ($\mu = (m_{WIMP}\, m_T)/(m_{WIMP} + m_T)$), v represents the initial WIMP velocity and m_T stands for the mass of the target nuclei. Two limiting scenarios can be explored:

1. $m_{WIMP} \gg m_T$: in this scenario $\mu \longrightarrow m_T$, yielding $E_R^{max} \approx 2 m_T v^2$. The maximum energy transfer for a nuclear recoil remains constant, dependent solely on the mass of the target.

2. $m_{WIMP} \ll m_T$: in this case $\mu \longrightarrow m_{WIMP}$, resulting in $E_R^{max} \approx 2 \cdot (m_{WIMP}^2 v^2)/m_T$. The maximum recoil energy scales quadratically with the WIMP mass, leading to lower energy spectra for WIMP masses that are significantly lighter than the target nuclei. Considering the finite threshold of real detectors, this usually results in a decreased sensitivity. Hence, light nuclei are preferred for light WIMP searches [57].

The minimum WIMP velocity required for a NR event of energy E_R can be derived and expressed as:

$$v_{min} = \sqrt{\frac{m_T E_R}{2\mu^2}} \tag{2.3}$$

Thus, lighter dark matter particles necessitate a larger initial velocity to generate a NR.

Scattering rates in a detector

Taking into account the complexity of the scattering process, an accurate estimation of the expected scattering rates in a detector can be obtained. Several considerations come into play:

- WIMPs exhibit a velocity distribution $f(\vec{v})$ rather than a fixed velocity value.
- The detector, situated on Earth, undergoes motion around the Sun and the Galactic centre.
- The scattering occurs coherently on nuclei, which are composite particles. Form factors that account for their structures have to be considered.
- The underlying spin dependence of the interaction can influence the cross-section and the form factors.
- Due to energy resolution and threshold considerations in detectors, as well as potential energy loss in the physical process, the observed energy may not correspond to the entire recoil energy.

Taking all of this into account, calculations [50] allow us to formulate the differential event rate as:

$$\frac{dR}{dE_R} = \frac{\rho_0}{m_{WIMP}\, m_T} \int_{v_{min}}^{v_{esc}} v f(\vec{v}) \frac{d\sigma_{WIMP}}{dE_R} d\vec{v} \tag{2.4}$$

ρ_0 denotes the local dark matter density in our Milky Way region, and σ_{WIMP} represents the WIMP-nucleus interaction cross-section and v_{esc} indicates the escape velocity of our galaxy. This equation comprises various contributions from various fields of physics. Astrophysics knowledge is needed to estimate the local dark matter density. The WIMP-nucleon cross-section can be converted into the WIMP-nucleus one through nuclear physics calculations. Lastly, particle physics defines the scattering framework.

Cross Sections

Considering the non-relativistic nature of the scattering process and the considerations outlined for the interaction, the interaction cross-section can be expressed as:

$$\frac{d\sigma}{dE_R} = \left[\left(\frac{\sigma}{dE_R} \right)_{SI} + \left(\frac{\sigma}{dE_R} \right)_{SD} \right] = \frac{m_T}{2\mu^2 v^2} \left[\sigma_0^{SI} F_{SI}^2 + \sigma_0^{SD} F_{SD}^2 \right] \tag{2.5}$$

Where the subscripts SI and SD refer to spin-independent and spin-dependent interactions, respectively, while the $F_{SI/SD}$ denote the respective nuclear form factors,

accounting for the approximation of the scattering off a nucleus as a whole.
For spin-independent interactions, the cross-section is:

$$\sigma_0^{SI} = \frac{4\mu^2}{\pi} \left[Z f_p + (A - Z) f_n \right]^2 \tag{2.6}$$

Where Z is the atomic number of the target atom, A is its mass number, and $f_{p/n}$ are the form factors of protons/neutrons. It is commonly assumed that the distinction between protons and neutrons cannot be resolved, hence the preference for heavy target nuclei ($\sigma \propto A^2$).
For spin-dependent interactions, we can write a simplified cross-section that does not account for interactions between the neutrons and protons of the atoms:

$$\sigma_0^{SD} = \frac{32 G_F^2 \mu^2}{\pi} \frac{(J+1)}{J} \left[a_p \langle S_p \rangle + a_n \langle S_n \rangle \right]^2 \tag{2.7}$$

where J stands for the angular momentum, $a_{p/n}$ denote the individual couplings to protons/neutrons and $\langle S_{p/n} \rangle$ are the spin expectations of the two [50].

Annual Modulation

Previously, we noted that determining the velocity of WIMPs involves analysing the motion of the Sun around the centre of the Milky Way, considering also the Earth's orbit around the Sun. This motion has a much lower velocity, such that the ratio of the orbital velocity to the solar velocity is $\mathrm{v}_{orbit}/\mathrm{v}_{Sun} \approx 0.07$.
However, this motion inherently results in annual modulation [58]. During half of the year, the combination of the Earth's and Sun's motion results in the summation of their velocity. Conversely, for the other half of the year, the combination of their motions leads to a subtraction. Figure 2.3 provides a schematic representation of this behaviour.
Although this effect can be utilised in the search for WIMPs, its magnitude is only a few per cent. Therefore, observing several interactions ($\mathcal{O}(100)$) is necessary to study annual modulation effectively.

Directionality

In its orbit around the Galactic centre, the Sun-Earth system moves towards the Cygnus constellation. The ability to discern the direction of recoils could offer improved insight into the signal and unprecedented background rejection [59]. Due to this motion, assuming an anisotropic dark matter halo, the recoil spectrum peaks in the direction opposite to our motion towards Cygnus.
Highly sensitive detectors could investigate the daily modulation of this signal attributed to Earth's rotation about its own axis. The event rate in the forward direction is expected to be one order of magnitude larger than in the backward direction.

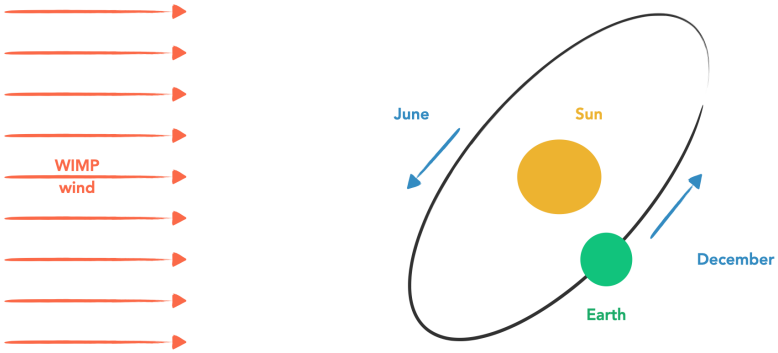

Figure 2.3: Schematic representation of the motion of the Earth around the Sun combined with their common motion around the Galactic centre, through a dark matter halo at rest. When the Earth's velocity sums with the Sun's velocity, the rate will be enhanced (maximum in June), while when it subtracts, it will be damped (minimum in December). Image reproduced from [58].

Detectors capable of measuring the direction of nuclear recoils with high angular resolution would require only a few tens of events to distinguish a dark matter interaction from background events [61], which exhibit no preferred direction. In light of this, a large experimental effort towards directional detectors is underway [62].

2.2.3 Detection Challenges

The main challenge for direct dark matter searches is represented by the various backgrounds that need to be mitigated via dedicated measures [28]. The anticipated event rate overall is exceedingly low, prompting direct detection experiments to be designed to minimise the background in the region of interest (ROI) and obtain a cleaner signal. The major background contributions will be outlined, followed by the most common mitigation strategies.

Backgrounds

Electronic recoil (ER) backgrounds are generated by β and γ particles interacting electromagnetically with the electrons of the target. This background originates from the decay of various radioactive isotopes. A different source of ER background stems from the elastic scattering of low-energy solar neutrinos with atomic electrons. However, the cross-section for these interactions is extremely small, rendering this background far from the present experiments' reach.

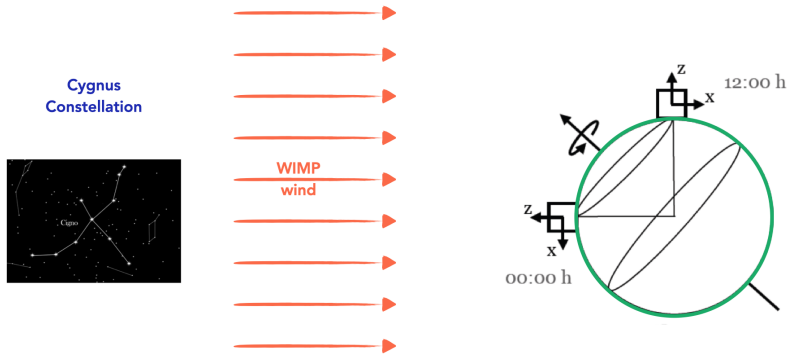

Figure 2.4: Schematic representation of the directionality of the WIMP signature on Earth. Due to the Earth's motion, this directionality presents a daily modulation. Image reproduced from [60].

Another significant source of background is represented by the α particles. While these particles typically deposit too much energy to fall into the ROI, if they lose enough energy into insensitive parts of the detectors, their signal can become significant.
A critical background for WIMP searches is represented by nuclear recoils, which can mimic the WIMP signal. These recoils can be induced by neutrons originating from different sources, including (α,n) reaction, spontaneous fissions, or cosmic ray muons interactions. A source of NR background arises from the coherent scattering of neutrinos (from various sources) off target nuclei, producing recoils, which cannot be distinguished from the WIMPs ones on an event-by-event basis. This background is nowadays known as the neutrino fog.

Mitigation Strategies

Mitigation strategies for these experiments are often summarised with the definition of "low-background techniques" [63] and are common to most direct detection experiments.
Placing direct detection experiments in underground laboratories, where the experimental set-up is shielded by an overburden of rock, effectively reduces the flux of cosmogenic muons (see Figure 2.5), also reducing the muon-induced neutron background, with further mitigation achieved by incorporating a muon veto system.
Additionally, employing either massive and compact shields (e.g. made of Pb, Cu, PE or larger shields) or larger shields constructed from lighter isotopes (such as water or argon) aids in reducing the flux of αs, βs, γs and n from the environment, thus the electronic and nuclear recoil backgrounds.
The design of detectors is crucial for minimising backgrounds. Thus, detectors and

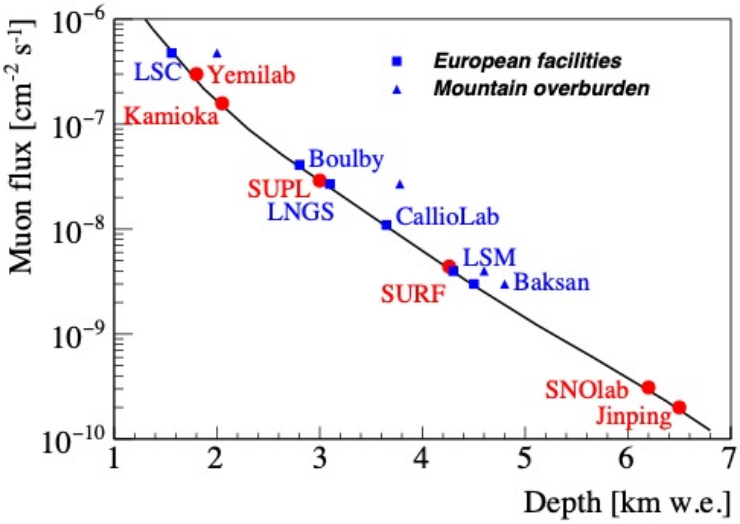

Figure 2.5: Muon flux in underground laboratories. The solid line represents the muon flux as a function of depth for a flat overburden. For laboratories located under a mountain, the real flux has an angular dependence. Image taken from [64].

target materials are selected and treated to minimise the radioactive contamination and further activations. Whenever possible, target materials are purified from contaminations.
Fiducialisation of the detector volume often assists in reducing backgrounds at the detector surface.

2.3 Experimental Approaches

Since a particle interaction in a detector can create different types of signals, various approaches to the direct detection of dark matter exist. An overview of possible detection techniques based on the type of signal chosen for detection is provided below.
Three main signals can be read out in a particle detector, and they can be utilised and combined to directly detect dark matter: charge, light and heat signals. Figure 2.6 presents a list of the current direct detection experiments, categorised based on the detection channels used.

2.3.1 Ionisation Signal

An ionisation signal is created when an electron is either excited or ejected from an atom, forming an electron-hole (e^--h) pair. By applying electric fields to the target

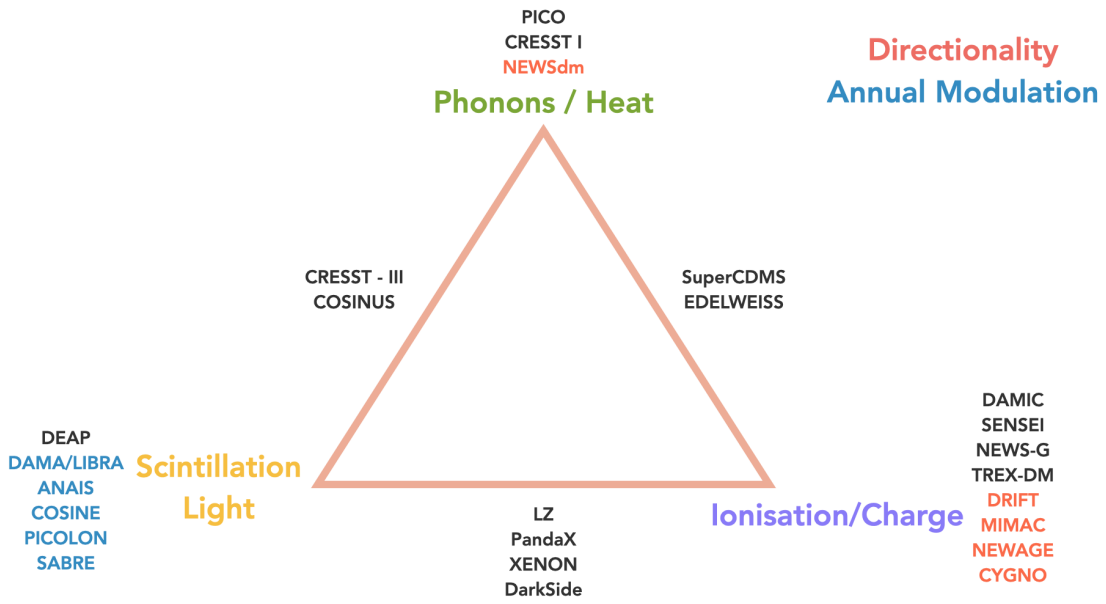

Figure 2.6: List of direct dark matter detection experiments, based on their energy readout channels. The experiments are listed near the readout channel they use or between two channels if they use a combination.

material, the free electron can traverse the material and, in some cases, undergo amplification. Typically, the drifting motion leads the ionisation signal towards a charge detector.
There are two main types of detectors using ionisation signals: liquid noble detectors and semiconductor-based ones.

Semiconductor Detectors Semiconductors are widely used in the hunt for dark matter. An energy deposition in a material of this type leads to the creation of a charge signal, which is proportional to the deposited energy. There exist two main kinds of detectors employing superconductors: cryogenic detectors and charge-coupled devices.
Cryogenic Detectors Semiconductors need a very tiny amount of energy to create an e^--h pair, corresponding to an average energy of 2.9 eV in Ge and 3.6 eV in Si, resulting in an excellent energy resolution [65].
However, detectors of this type have a rather slow time constant ($\tau \sim 1\,\mu$s). Moreover, constructing large-scale detectors (beyond a few kg scale) is currently not feasible.
The state-of-the-art for these searches is p-type point contact HPGe detectors, which enable the construction of kg-scale detectors and can achieve thresholds down to ap-

proximately $\sim 160\text{eV}_e e$ [66].
Charge-coupled Devices (CCDs) CCDs essentially consist of arrays of capacitors (pixels), electrically coupled to each other and typically made of Si. The charge signal is drifted through an applied electric field towards the pixel gate until readout. This readout scheme enables the 3D spatial reconstruction of an event.
Experiments utilising this technique are typically searching for dark matter-electron interactions [67]. The state of the art for these detectors is represented by Skipper CCDs, enabling multiple non-destructive charge measurements, leading to single-charge resolution and sub-electron noise thresholds [68].

Noble Liquids Detectors Argon (Ar) and Xenon (Xe) are very good scintillators and can be ionised easily. They are used in the liquid state to build massive, dense and compact dark matter targets, which already reached the ton-scale [69].
One of the main applications of this technology is dual-phase time projection chambers (TPC). These TPCs can read out different signals: the primary and the secondary scintillation light and the ionisation signal. Combining these signals, the position of the interaction can be precisely reconstructed while reaching a very high energy resolution and a very good ER/NR discrimination [70]. This ER/NR discrimination is perdormed through the ratio of the ionisation to the scintillation signal and in liquid Ar detectors also through pulse shape discrimination.

2.3.2 Light Signal

Scintillating materials emit light when they absorb radiation, which various types of light detectors can employ to study dark matter interactions.
Typically, only a small percentage of the deposited energy is emitted as scintillation light. The light signal is often combined with other detection techniques for particle discrimination.

Noble Liquids Detectors Single-phase liquid noble gas detectors only read out the scintillation signal from Ar, and they have a very simple design: a spherical target is surrounded by photomultipliers [71]. Pulse shape discrimination can be used for signal discrimination and, thus, background reduction. With these detectors, the position of the interaction can be reconstructed.

Scintillating Crystals Employing scintillating crystals, such as NaI(Tl) and CsI(Tl), large mass detectors can be constructed. Thanks to the large atomic mass of the atoms of these crystals, they exhibit high sensitivity to spin-independent interactions. However, these materials often have high levels of intrinsic background.
Large-mass scintillating crystals are often used to search for the annual modulation of the dark matter signal [72].

2.3.3 Heat signal

Two types of heat signals can be distinguished: phonon signal and superheating.

Phonon Detectors Collecting the heat (thermal or non-thermal phonons) signal involves measuring the slight temperature increase induced by particle interactions. To detect such a tiny increase, operating phonon detectors at cryogenic temperatures is imperative to mitigate thermal noise, and lowering their heat capacity is fundamental to achieve optimal sensitivity.
Various types of thermometers can measure this signal [73]. In chapter 4, we will discuss one of them, the transition edge sensor, in detail.
The measured energy represents the total deposited energy in these detectors, allowing for an excellent energy resolution. The energy needed to create phonons can be as low as few meV.

Bubble Chambers Bubble chambers utilise superheated liquids maintained at temperatures just above their boiling points as dark matter detectors. A local phase transition occurs in such liquids, creating a bubble if the energy deposited into a certain micro-scale volume surpasses a specific threshold. Tuning the bubble chambers' parameters, these thresholds can be controlled to enhance background discrimination [74], rendering bubble chambers almost insensitive to ER.
The signal is captured with stereoscopic cameras, enabling precise recording of the amount of bubbles and their positions. This type of detector has significant drawbacks: the impossibility of measuring the recoil energy and a large dead time resulting from the time required to achieve a superheated state. Typically, liquids containing fluorine (F) are used for spin-independent searches, while liquids containing iodine (I) are used for spin-dependent searches [75].

2.4 Current Status

The current status of the spin-independent and spin-dependent dark matter searches are shown in Figure 2.7 and Figure 2.8, respectively. A portion of the parameter space has been explored by combining the exclusion limits provided by various experiments. Looking at the plots, it becomes evident how different searching techniques exhibit varying degrees of sensitivity to different regions of the parameter space. Therefore, a collaborative effort is required to comprehensively explore the entire parameter space.

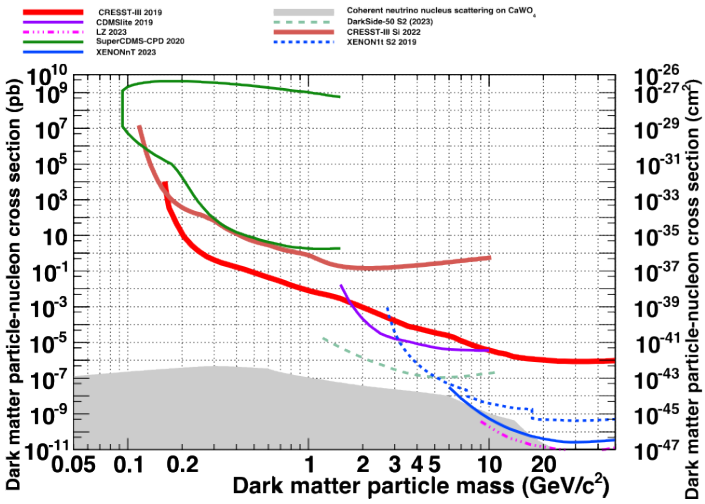

Figure 2.7: Current status of the direct detection experiments for spin-independent dark matter-nucleus scattering.

.

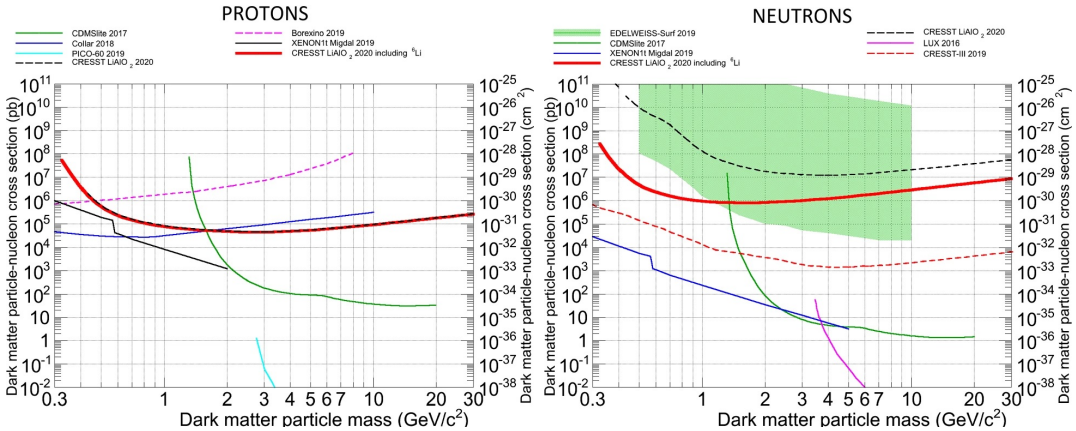

Figure 2.8: Current status of the direct detection experiments for spin-dependent dark matter-nucleon interaction, for proton (*left*) and neutron (*right*). Image taken from [76].

Chapter 3

The CRESST experiment

The Cryogenic Rare Event Search with Superconducting Thermometers (CRESST) experiment is situated at the underground Laboratori Nazionali del Gran Sasso (LNGS) in Italy. CRESST uses cryogenic calorimeters operated at a few mK to directly detect dark matter particles through their elastic scattering off target nuclei, as described in section 2.2. When a particle interacts with one of the target nuclei, it deposits energy in the crystal, leading to a measurable increase in the sensors' temperature. The working principles of these detectors will be detailed in chapter 4.
The first part of this chapter will focus on delineating the facilities of the CRESST experiment, the principal backgrounds, and the shielding utilised to mitigate them. Subsequently, our attention will be directed toward the CRESST-III detector modules and their design. The chapter will conclude with the most recent results obtained by the CRESST experiment, along with future plans.

3.1 Experimental setup

The CRESST facility is located in the Hall A of the LNGS (see Figure 3.1), where a 1400 m of overburden of rock, corresponding to 3800 m.w.e. (meters of water equivalent), provides an effective shielding against cosmic rays radiation (see Figure 2.5). To further mitigate the effects of remaining backgrounds, CRESST utilises multiple passive shielding layers.

3.1.1 Shieldings

In the LNGS environment, the most significant sources of background are electrons, gammas (γ), αs from natural radioactivity, and neutrons resulting from environmental radioactivity or muon-induced reactions.
To mitigate these backgrounds, CRESST employs multiple passive shielding layers (shown in Figure 3.2). In the following, the various shieldings will be introduced

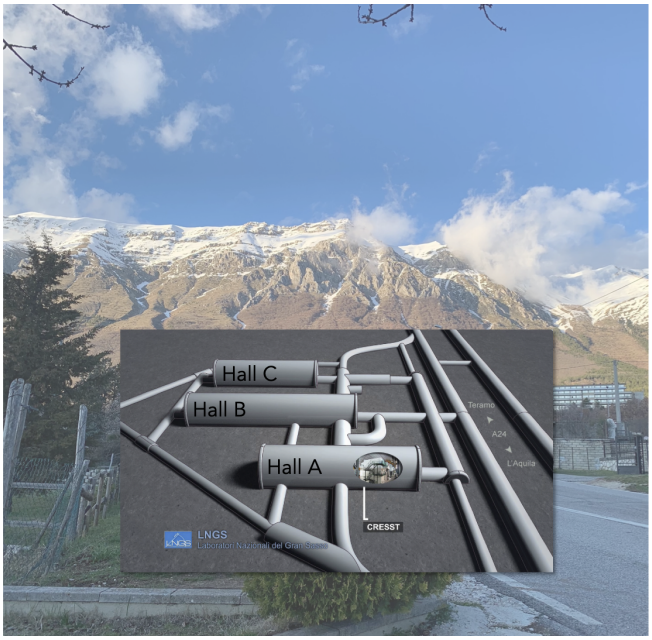

Figure 3.1: Location of the CRESST experiment in the Hall A of the LNGS.

from the outermost to the innermost, emphasising their contribution to the overall background reduction.

Polyethylene

Polyethylene (PE, $C_2H_4)_n$ is a plastic material created from the polymerisation of ethylene (C_2H_4).
The outermost shield of the CRESST cryostat is constructed from this material, as it is highly effective in moderating the neutrons, which are primarily originating from cosmic muons interacting in the rocks and from radioactivity (see section 2.2.3). Light elements are preferred for this purpose due to kinematic reasons.
However, neutrons can also arise from interactions of cosmic muons with the inner lead or copper shields. This background can pose a significant risk if the muon veto system does not detect the primary muons. An inner layer of PE is positioned close to the detectors to address this concern.
The outer PE layer is 40 cm thick and weighs approximately 10 t, while the inner layer is 3.5 cm thick.

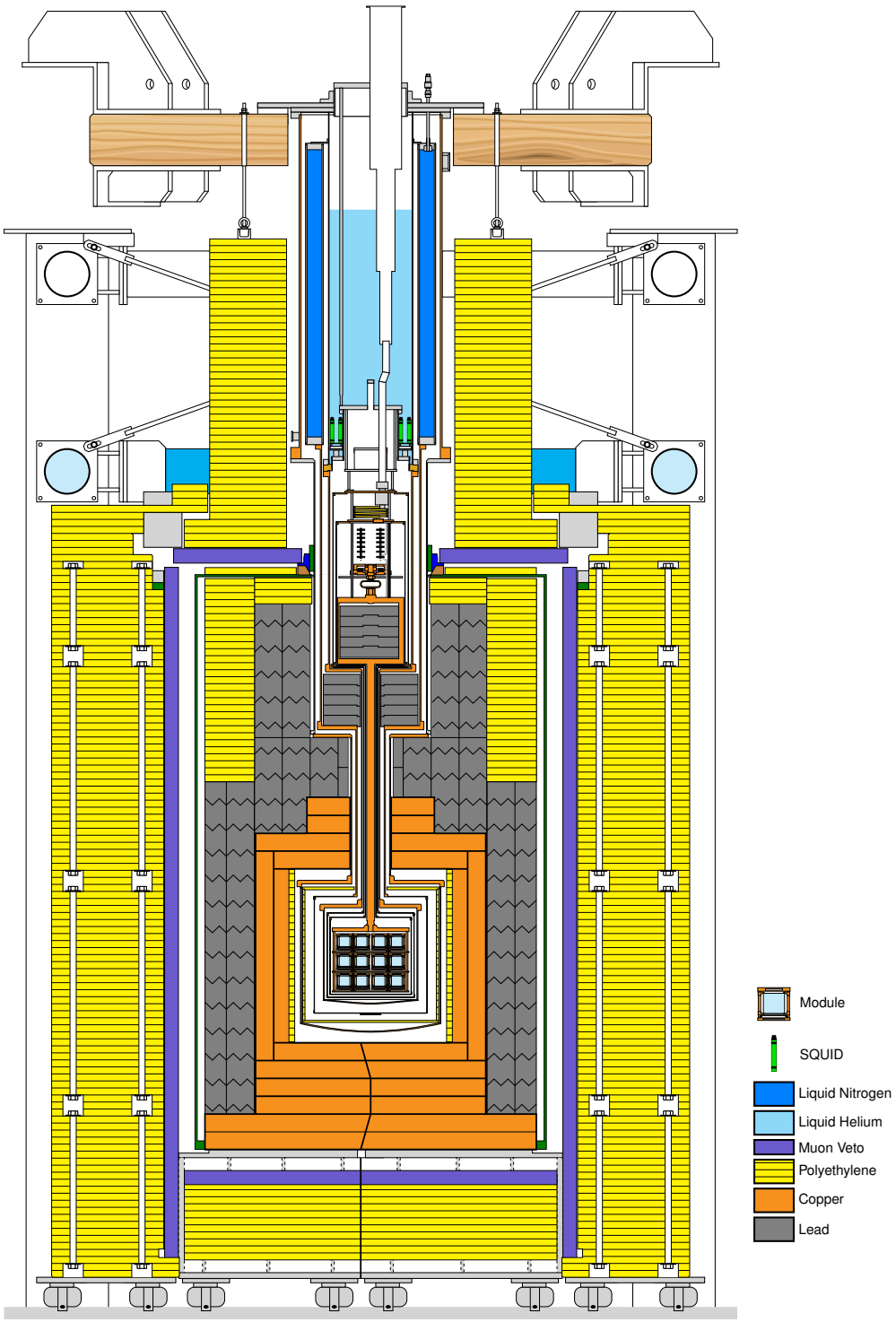

Figure 3.2: Schematic drawing of the CRESST setup, highlighting the shielding layers and the positioning of the detector modules and SQUIDs electronics. Picture taken from [77]

Muon Veto

The muon veto system serves as the only active shielding layer of the CRESST experimental setup. It comprises 20 plastic scintillator panels read out by photomultiplier tubes (PMTs), providing a geometrical coverage of 98.7%.
While muons are not a dangerous background for CRESST, they can interact in the materials surrounding the experimental volume, generating secondaries (e.g. neutrons) that could mimic a dark matter signal. Tagging the muons entering the cryostat allows the discrimination of muon-induced events during the analysis.

Radon Box

The radon box is airtight and continuously flushed with nitrogen, and it encloses the CRESST experimental volume within the muon veto. The primary objective of this system is to protect the experiment against any surface contamination of ^{210}Po originating from radon (Rn) decay.
Rn represents a significant background for underground rare event searches, although it was not discussed in section 2.2.3.
^{222}Rn arises from the decay of ^{238}U and is a noble gas that does not interact with surrounding materials. It possesses an average lifetime of 3.82 days, allowing it sufficient time to escape from rocks into the experimental halls and contaminate the materials surrounding the experimental volume. Following the decay of ^{222}Rn, the decay chain progresses rapidly until it reaches the long-lived isotope ^{210}Pb, with a lifetime of approximately 22.3 years. This daughter nucleus can adhere to surfaces exposed to ^{222}Rn, leading to contamination. The decay chain further proceeds with the short-lived isotopes ^{210}Bi (with a lifetime of approximately 5 days) and ^{210}Po (with a lifetime of about 138 days) before reaching the stable isotope ^{206}Pb. This decay potentially represents a dangerous background, as ^{210}Po decays to a ^{206}Pb nucleus possessing 103 keV of energy, via the emission of an α particle, with an energy of 5.3 MeV. Two possible signatures can contaminate the ROI, both coming from the recoil of the ^{206}Pb nucleus in the absorber crystal, depending on the location of the ^{210}Po contamination. If the contamination is on the surface of the crystal itself, during the ^{210}Po decay, the total ^{206}Pb energy is deposited in the absorber, together with part of the energy of the α particle, thus depositing an energy larger than 103 keV. Conversely, if the surface of the detector's housing is contaminated, the recoil energy detected in the absorber is lower than 103 eV, as the nucleus loses part of its energy reaching the target crystal. This latter scenario can contaminate the ROI down to threshold.
The level of ^{222}Rn at LNGS is measured to be about 50 $\mathrm{Bq \cdot m^{-3}}$ [78].

Lead

A 20 cm thick layer of radiopure lead, for a total weight of 24 t, is placed inside the radon box to shield against natural radioactivity.
Thanks to its high atomic number and density, lead is particularly effective for shielding against γ rays. In contrast, even a thin layer of lead easily stops α and β particles, as they lose energy primarily through ionisation.
The primary sources of these types of backgrounds are the decay chains of ^{40}K, ^{235}U, ^{238}U and ^{232}Th.

Copper

Avoiding ^{210}Pb contamination of the lead is nearly impossible, as some level of radioactive contamination is also present in low-radioactivity lead. Consequently, an inner shield of Cu 14 cm thick, weighing 10 t is employed to shield against the γs and βs originating from the lead. Indeed, Cu can be purified at a level of 99.99%, thus it is a particularly convenient choice for low-background experiments.

3.1.2 Cryostat

As previously mentioned, CRESST operates cryogenic calorimeters at mK temperatures. These extremely low temperatures are reached using a commercial dilution refrigerator, specifically an Oxford Instruments 1000S.
The mixing of two helium isotopes, ^{3}He and ^{4}He, provides the cooling power for such a refrigerator. More details on the working principle of dilution refrigerators can be found in [79].
In the CRESST facility, the cryostat is positioned on top of the various shieldings previously described, while the detector modules are housed in the so-called carousel (see Figure 3.2), thermally coupled to the cryostat through a 1.3 m long Cu cold finger. This design ensures that the experimental volume has direct lines of sight only with low-radioactivity materials, minimising potential sources of background radiation.

3.2 CRESST Phases

In 1984, scientists L. Stodolsky and A.K. Drukier of the Max Planck Institute for Physics (MPP) conceived the idea of utilising cryogenic detectors for neutrino detection. Although their first idea did not yield the desired results, this innovative concept laid the foundation for developing cryogenic particle detectors.
Fast forward to 1993, when a collaborative effort between MPP and the Technical University of Munich (TUM) focused on advancing cryogenic detector technology. This collaboration led to the proposal of an experiment at the LNGS aimed at detecting

dark matter, employing transition edge sensors (TESs). Originally named the "Munich Dark Matter Search", in 1996, the project expanded to include participation from groups at Oxford and LNGS, and its name was changed to CRESST.

CRESST was placed in Hall B at the LNGS (see Figure 3.1). In its initial phase, CRESST-I, the experiment utilised four sapphire crystals, each weighing 262 g. Published in 2003 [80], the results from this phase established leading exclusion limits for WIMPs with a mass around 1 $\mathrm{GeV/c^2}$.

At that time, despite extensive efforts to shield the experiment and select radiopure materials, the remaining backgrounds remained too high to make further progress with the existing detectors. Consequently, CRESST incorporated the readout of a secondary signal for background discrimination. This involved changing the target material to $CaWO_4$, which emits scintillation light that can be used for distinguishing electron recoils from nuclear recoils (more details in the following). Additionally, $CaWO_4$ offered the advantage of its heavy W nucleus.
Before the beginning of this second phase, CRESST-II, the experiment was moved from Hall B to Hall A (where it is still located). In 2004, first results from two $CaWO_4$ crystals, with a mass of 300 g were published [81].
Subsequently, the electronics system underwent upgrades, enabling the simultaneous operation of 33 detectors. New post-upgrade results were published in 2015 [82].
The technology of the TES employed by CRESST allowed for low energy thresholds, enabling the exploration of low-mass dark matter candidates, a rapidly growing area of interest during those years.

The natural progression for the collaboration was to further reduce the energy thresholds, extending the accessible dark matter mass range to masses below a few $\mathrm{GeV/c^2}$. With this goal, the detector design for the next phase of the CRESST experiment, known as CRESST-III, was modified. The detector modules employed in CRESST-III will be described in detail in the following.

3.2.1 CRESST-III Detector Modules

The standard CRESST-III detector module is made of a $20\times20\times10\,\mathrm{mm^3}$ $CaWO_4$ crystal as the main absorber, weighing approximately 24 g and equipped with a W-TES. This crystal size was chosen to lower the energy thresholds and explore lower WIMP masses [83, 84]. Additionally, each module includes an auxiliary thin crystal, measuring $20\times20\times0.4\,\mathrm{mm^3}$, made of silicon-on-sapphire and also equipped with a W-TES for light detection. The housing of the detector module is fully covered in reflective, scintillating foil, optimising light collection for the light detector and enhancing its signal. Figure 3.3 shows a schematic drawing and a photo of a standard CRESST-III detector,

highlighting all components.

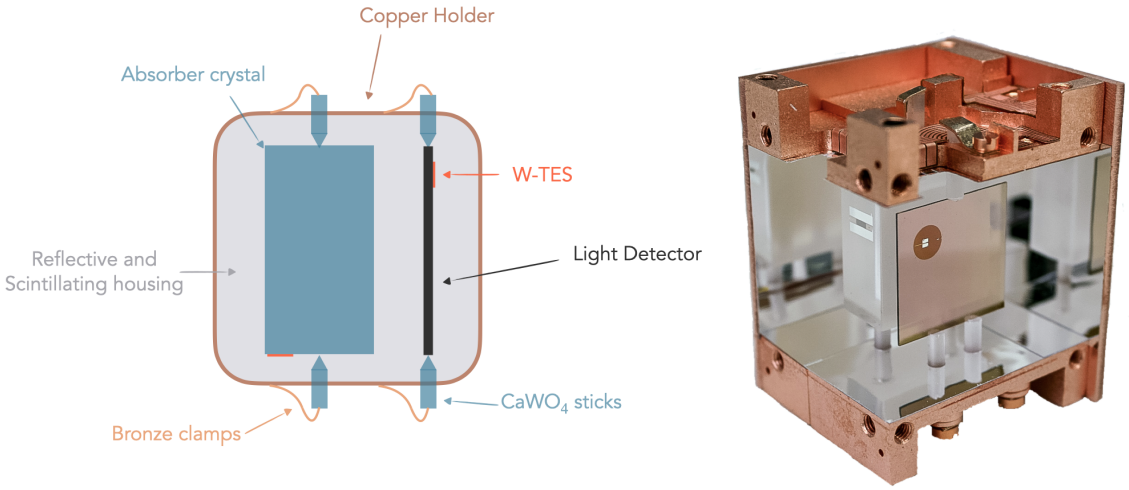

Figure 3.3: Standard CRESST-III detector module. *Right:* Schematic drawing showing the different components of the module. *Left:* Photo of an open module.

As previously mentioned, detecting scintillation light enables background discrimination on an event-by-event base. Electron recoils, mainly caused by γs and βs, produce more scintillation light than nuclear recoils. The light yield is defined as the ratio of the energy measured in the light channel to that in the phonon channel,

$$LY = \frac{E_{light}}{E_{phonon}} \tag{3.1}$$

and it quantifies the difference between ER and NR. Figure 3.4 illustrates a schematic representation of a light yield plot, where the light yield is plotted on the y-axis and the phonon energy (representing the total deposited energy) on the x-axis. The light measured for electron recoils is normalised to 1 at the energy of the calibration source, while nuclear recoils exhibit significantly quenched light emission. This distinction allows for the discrimination between nuclear and electron recoils, thereby reducing background levels.

With the CRESST technology, several materials can be employed as main absorbers. Non-scintillating materials can also be considered for specific applications. This is a great advantage of this type of technology, as multiple materials enable the exploration of different portions of the parameter space and the study of different types of interactions.

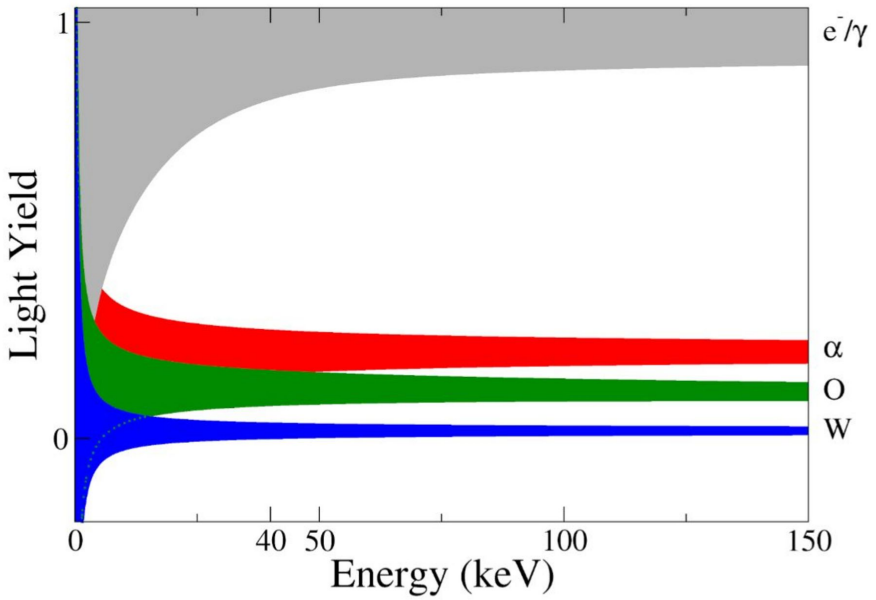

Figure 3.4: Schematic drawing of the light yield plot, taken from [85].

3.2.2 CRESST-III Results

The design goal for these detectors was to achieve thresholds below 100 eV, an objective that was successfully achieved, with the so-called Detector A reaching a threshold as low as 30.1 eV.
This achievement led to exclusion limits, published in 2019, which remain the best limits in a significant portion of the parameter space for masses below 1 GeV/c^2, under standard assumptions [86]. However, during the first measurement campaign of CRESST-III, the collaboration reported the first observation of an increase in event rate with energies below 200 eV. Numerous other experiments have then reported similar observations, and this background is currently well known as the "Low Energy Excess" (LEE) [87]. A detailed discussion of this background and CRESST's strategies for exploring it can be found in section 7.1. Subsequent measurement campaigns from CRESST focused on understanding this background while still delivering competitive results in dark matter searches. Spin-dependent interactions were studied using lithium aluminate crystals, yielding highly competitive outcomes [76]. Furthermore, the lowest reachable dark matter mass was lowered thanks to the use of a thin silicon wafer [88], with a threshold of 10 eV.

3.2.3 Future plans

In February 2024, new detector modules were mounted in the CRESST cryostat for the current measurement campaign, the so-called Run37. This run focuses on understanding the origin of the LEE, employing two newly designed detector modules: the doubleTES (see chapter 7) and the miniBeaker (see [89] for details).

Looking ahead, the long-term plan for CRESST involves upgrading the electronics system to enable the operation of 288 channels simultaneously, corresponding to approximately 100 detector modules. The goal of this upgrade is to increase the collected exposure while lowering the energy threshold of the detectors. More details on the upgrade can be found in section 6.1.
Once the mystery of the LEE is resolved, the bottleneck in enhancing the dark matter reach of the CRESST experiment will be the collected exposure and thresholds of the sensors. Increasing the collected exposure will enable CRESST to probe lower cross sections for WIMP-nucleon interactions. Lowering the thresholds will enable CRESST to probe a new, unexplored portion of the parameter space.

Chapter 4

Transition edge sensors for dark matter searches

Cryogenic detectors play a pivotal role in the search for dark matter, particularly in probing low-mass regions of the parameter space. The first use of such detectors in elementary particle physics experiments traces its origins to the 1930s. In the 1990s, these detectors underwent significant development, inspired by the proposals by Fiorini and Niinikoski [90], as well as by Moseley, Mather and McCammon [91] in 1984.
Presently, cryogenic detectors find extensive applications across various disciplines, from probing the mysteries of dark matter and neutrinos to studying the cosmic microwave background.
This chapter will begin with an overview of cryogenic calorimeters and their fundamental working principles. Subsequently, attention will shift towards a specific type of sensor for cryogenic calorimeters, namely Transition Edge Sensors (TES). Section 4.2 will delve into the detailed thermal model governing these detectors. Section 4.3 will provide a brief overview of the SQUIDs readout system, and section 4.4 will concisely present the primary noise sources in cryogenic calorimeters.

4.1 Cryogenic calorimeters

Calorimeters are detectors designed to collect and measure the total energy deposited when a particle interacts in the detector. In cryogenic calorimeters, the energy is measured subsequently to its conversion into heat.
The heat signal corresponds to elementary excitations of the crystalline lattice of a solid, with energies of $\mathcal{O}$(meV). Therefore, these calorimeters must be operated at extremely low temperatures to prevent thermal excitations of the signal mediators.
The signal measured by a cryogenic calorimeter is proportional to the ratio of the deposited energy and the heat capacity $\Delta T = \Delta E/C$. Operating these detectors at low temperatures also lowers their heat capacity, thus enhancing the signal.

Cryogenic calorimeters also benefit from the absence of quenching, as all of the deposited energy is converted into heat without any loss.

4.1.1 Transition edge sensors

The elementary excitations of the crystalline lattice of a solid are lattice vibrations, commonly referred to as phonons. The phonons excited by an energy deposition in a cryogenic calorimeter can be read out through several types of sensors. A detailed description of the numerous possibilities is beyond the scope of this thesis and can be found in [92].
In this work, we will focus on the sensors utilised in the CRESST experiment, the transition edge sensors (TES). TES are superconducting films stabilised in the phase transition between their normal conducting and superconducting state in the so-called "operating point". Figure 4.1 illustrates the TES working principle: the resistance of a superconducting thin film experiences a steep dependency on its temperature during this phase transition.
When energy is deposited in the absorber $\mathcal{O}$(keV), it leads to a temperature rise $\mathcal{O}(\mu\text{K})$ in the TES, resulting in a change in the film's resistance $\mathcal{O}(\text{m}\Omega)$, measured with the SQUID readout system.

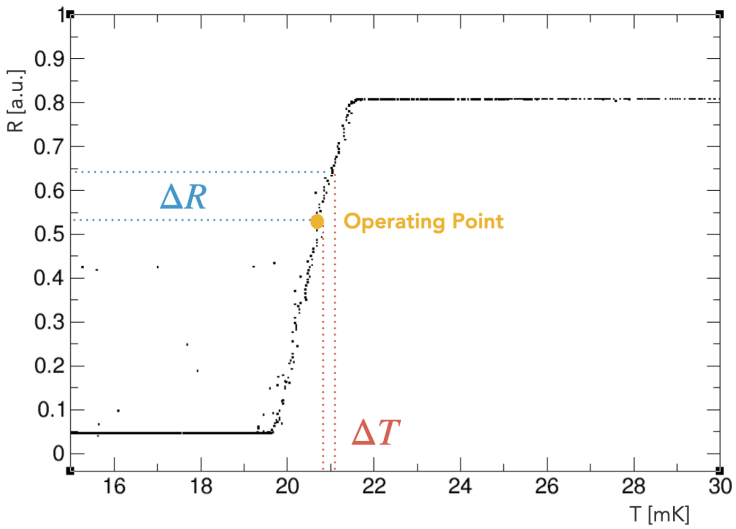

Figure 4.1: Schematic representation of the TES working principle. The operating point in the normal to superconducting phase transition is highlighted. When the temperature of the sensor increases, its resistance also increases accordingly, and it can be measured through a SQUID readout system.

4.2 Detector Thermal Model

In this section, we will present the thermal model that describes the evolution of the observed pulses. This model was first developed in 1995 by Franz Pröbst et al. [93], and it is schematically shown in Figure 4.2. The detectors under consideration comprise an absorber crystal (the most common ones are $CaWO_4$, Al_2O_3 and Si), where incoming particles interact, a tungsten superconducting thin film, acting as a thermometer (W-TES), and a gold thin structure, thermally connecting the sensor and the heat bath.

4.2.1 Heat Capacities

Understanding the formation of the signal in the TES requires a description of the heat capacities of the various components of the detector.
In general, the heat capacity (C) of a body determines the extent to which its temperature can rise given a certain energy deposition:

$$C = \frac{Q}{\Delta T} \tag{4.1}$$

where Q is the heat transferred to the material. The heat capacity is closely linked to the thermodynamic properties of the system under analysis, thus requiring different descriptions for different materials. The specific heat denotes the ratio between the heat capacity of the body and the mass of a material (c = C/M).

Non-Metals

The lattice specific heat (c_{ph}) is the dominant contribution to the heat capacity of crystalline dielectric materials. The Debye model describes the behaviour of these materials, indicating that at temperatures below the Debye temperature (Θ_D), phonons begin to "freeze out". The value of Θ_D varies significantly depending on the material, with higher values observed for lattices composed of light and strongly bound atoms and lower values for those composed of heavy and weakly bound atoms [79].
Applying the Debye models, the specific heat of crystalline dielectric materials (c_{ph}) for temperatures below $\Theta_D/10$ can be expressed as [79]:

$$c_{ph}(T) = \frac{12}{5}\pi^4 N_a k_B \left(\frac{T}{\Theta_D}\right)^3 = 1944 \left(\frac{T}{\Theta_D}\right)^3 \doteq AT^3 \tag{4.2}$$

Where N_a denotes the number of lattice atoms per mole. The Debye temperatures of materials commonly used in CRESST as absorbers are listed in Table 4.1.
Due to the cubic dependence on temperature, the specific heat of these materials is strongly suppressed at low temperatures. This feature also characterises pure semiconductors. Consequently, crystalline dielectric and pure semiconductors are highly suitable absorber materials for cryogenic calorimeters.

	$CaWO_4$	Al_2O_3	Si
Θ_D [K]	228	1041	648
$\nu_D = k_B\Theta_D/h$ [THz]	4.8	21.7	13.5

Table 4.1: Debye temperatures (Θ_D) and Debye frequencies ($\nu_D = k_B\Theta_D/h$) of the materials most commonly used as absorbers in CRESST.

Metals

Metals feature nearly freely moving conduction electrons, which can be thermally excited along with lattice vibrations. Thus, the total specific heat of a metal comprises two components: the lattice component (c_{ph}) and an electronic component (c_e). These components can be treated separately within the Born-Oppenheimer approximation, owing to the substantial mass difference between nuclei and electrons [94]. For temperatures below the Fermi temperature (T_F), the specific heat of the electronic system is described as [79]:

$$c_e(T) = \frac{\pi^2}{2} N_e k_B \frac{T}{T_F} \doteq \gamma T \tag{4.3}$$

where γ represents the material-dependent Sommerfeld constant and N_e denotes the number of conducting electrons per mole.
Consequently, the total specific heat capacity of a metal can be written as:

$$c = c_{ph} + c_e = AT^3 + \gamma T \tag{4.4}$$

For temperatures below 1K, the phonon contribution to the specific heat capacity can be neglected, as the linear dependence on T renders the electronic component dominant. Table 4.2 provides the values of the relevant parameters for the metals utilised in the CRESST TESs.

Superconducting Metals

The heat capacity of superconducting metals also consists of two components: the lattice and the electronic components. In the absence of a magnetic field, the transition to superconductivity is a second-order phase transition, characterised by a jump in the specific heat but no latent heat [95].
This jump in the specific heat is solely attributed to a jump in the electronic component. Indeed, the material possesses a new "degree of freedom" in this state, corresponding to the possibility of entering the superconducting state [79]. For simple superconductors, like Al, the BSC theory of superconductivity [95] predicts the jump to be:

$$\Delta c_e = 1.43\gamma T_C \tag{4.5}$$

	Tungsten (W)	Aluminium (Al)	Gold (Au)
T_C [mK]	15	1180	-
T_F [K]	2700	134900	63900
Θ_D [K]	383	428	162
γ [mJ·mol^{-1}· K^{-2}]	1.01	1.356	0.729

Table 4.2: Transition temperatures (T_C), Fermi temperatures (T_F), Debye temperatures (Θ_D) and Sommerfeld constants (γ) for the metals used in the CRESST thermometers.

Thus, below the transition temperature, the electronic component of the specific heat decreases exponentially. The remaining phonon contribution dominates the total heat capacity when the temperature falls below $T_C/2$.

4.2.2 Phonon Populations

When a particle interacts within the absorber, it generates high-frequency ($\mathcal{O}$(THz)) non-thermal phonons with energies in the meV scale. The initial spectrum of these phonons depends on the interaction type. Nuclear interactions deposit energy through local deformations of the crystal lattice, exciting non-thermal acoustic phonons across a broad frequency range. On the other hand, electronic interactions predominantly create optical phonons, which rapidly ($\mathcal{O}$(100 ps)) decay into acoustic phonons with half of the material's Debye frequency (refer to Table 4.1). Thus, electron recoils initially lead to an almost monoenergetic frequency distribution.
In both cases, these acoustic phonon populations decay to a thermal distribution due to lattice anharmonicity, with a decay rate that strongly depends on frequency [93]:

$$\Gamma_{decay} \propto \nu^5 \tag{4.6}$$

As a result of this pronounced frequency dependence, decay begins rapidly, leading to a phonon population with a mean frequency of $\mathcal{O}$(100 GHz). Any difference in the phonon frequency distributions originating from the different types of interactions is hereby washed out. Following this first rapid decrease of the average phonon frequency, the decay continues at a much slower rate, with the mean phonon frequency remaining nearly constant over the timescale of the sensor response.
During this time, the non-thermal phonons undergo a few surface reflections and uniformly fill the crystal in a timescale of the order of a few μs for the detectors under consideration.
These non-thermal phonons can either directly be absorbed by the free electrons of the thermometer or thermalise within the absorber, mainly through surface inelastic reflections, before being transmitted to the phonon system of the thermometer. In the former scenario, there is a time-dependent power input on the electron system of the

metal film ($P_e(t)$). Conversely, in the latter scenario, the thermalisation of non-thermal phonons generates a power input into the phonon system of the absorber ($P_a(t)$) that can be transmitted to the electron system of the thermometer through the weak coupling between its electron and phonon systems.
To comprehend the signal originating from these processes, we need to analyse the thermal couplings between the various components of the detector, which determine the energy transport into the thermometer.

4.2.3 Thermal Couplings

A particle interaction in the absorber creates a non-equilibrium situation where the various sub-systems of the calorimeter assume different temperatures. The temperature of the electron system of the thermometer dictates its resistance, affecting the measured signal. Due to these temperature discrepancies among the sub-systems, heat flow occurs between them until equilibrium is restored. The temporal evolution of the signal depends on the couplings between the different thermal sub-systems of the detector.

Kapitza Coupling

When the non-thermal phonons, which fill the entire absorber volume shortly after a particle interaction, reach the absorber-thermometer interface, they can either be transmitted to the thermometer or reflected back into the absorber. The transmission probability can be computed within the theory of anisotropic elastic continua [96].
The energy flux per unit area and time across the boundary of two materials denoted as $\dot{Q}_{1\to2}$, can be computed by summing over all modes and wave vectors of incident phonons [93]:

$$\dot{Q}_{1\to2} = \left\langle \frac{E}{V} \right\rangle \frac{1}{2} \langle v_\perp \alpha \rangle \tag{4.7}$$

Here, $\langle E/V \rangle$ denotes the average energy density of the phonons in the first material (the absorber), $v_\perp$ is the component of the phonon group velocity perpendicular to the interface, α represents the transmission probability, and thus $\langle v_\perp \alpha \rangle$ defines the transmission of the incident phonons over the interface averaged over modes and wave vectors of the incident phonons. This equation can be utilised to compute the energy transmission of both thermal and non-thermal phonons, as the transmission through an ideal boundary is independent of the phonons frequency.
The heat boundary conductance of thermal phonons, referred to as Kapitza conductance (G_K), can be computed following [93]:

$$G_K = \frac{\dot{Q}_{1\to2}(T+\Delta T) - \dot{Q}_{2\to1}(T)}{\Delta T} = \frac{C}{2V} \langle v_\perp \alpha \rangle \propto T^3 \tag{4.8}$$

where C/V denotes the heat capacity per unit volume of the absorber. The cubic temperature dependence arises from the heat capacity of a dielectric absorber.

Electron-Phonon Coupling

The electron-phonon coupling (G_{ep}) characterises the thermal interaction between the absorber and the electrons of the thermometer. Since the metal film is stabilised in the transition between its normal and superconducting state, where only a few electrons are bound in Cooper pairs, the phonons of the absorber interact with the remaining free electrons. G_{ep} depends on the mean free path of phonons (ℓ_p). Therefore, this interaction depends on the frequency of the phonons (ω) and consequently differs for thermal and non-thermal phonons.
The mean free path of the phonons can be described by the product $\ell_p = q \cdot \ell_e$. Here, q represents the phonon wave vector, and ℓ_e is the electron mean free path, predominantly influenced by scatterings on the crystal's impurities. Thus, ℓ_e remains temperature independent, and the phonons' mean free path's temperature dependence is solely attributable to their wave vectors' temperature dependence.

Thermal Phonons At low temperatures, when $q \cdot \ell_e \ll 1$ for thermal phonons, the mean free path of both longitudinal and transverse phonons is proportional to ω^{-2}. The temperature dependence of the electron-phonon coupling can be expressed as [97, 98]:

$$G_{ep} \propto T^5 \tag{4.9}$$

Consequently, the electron system in the thermometer and the phonon system in the thermometer, as well as the absorber's phonon system, are thermally decoupled. This results in a significant slowdown of the thermal signal.

Non-thermal Phonons For non-thermal phonons, where $q \cdot \ell_e \gg 1$, the mean free path of longitudinal and transverse phonons is given by the Pippard model [99]. Longitudinal phonons induce density variations, resulting in strong interactions with the electrons of the thermometer due to associated space charge effects. The mean free path for inelastic scattering for longitudinal phonons is proportional to ω^{-1}. Conversely, transverse phonons do not involve density variations, hence no space charge effects, and they exhibit minimal interaction with the electrons of the thermometer.
Non-thermal photons absorbed by the thermometer quickly thermalise due to their strong interaction with the electron system. As a consequence, the temperature of the electron system increases rapidly. The thermal decoupling of the electron and phonon systems results in an overheating of the electrons in the thermometer compared to the absorber. Therefore, the thermometer's sensitivity is primarily determined by the heat capacity of the thermometer itself for non-thermal phonon signals, while it is not directly affected by the heat capacity of the absorber. The absorber only influences the sensitivity of the thermometer through its phonon transport properties.

Coupling to the Heat Bath

The thermal coupling of the detectors to the heat bath (G_{eb}) is realised through structures made of a normal conducting metal. In the CRESST-III detectors, this coupling consists of a thin gold film deposited on the absorber and connected to the heat bath via a gold bond wire. The strength of this coupling defines the thermal relaxation time of the thermometer through:

$$\tau = \frac{C_e}{G_{eb}} \tag{4.10}$$

where C_e denotes the heat capacity of the electron system of the thermometer. According to the Wiedemann-Franz law [100], the heat conductance of a gold coupling structure is given by:

$$G_{eb} = \frac{LT}{R} \tag{4.11}$$

where R represents the residual resistance of the gold structure at temperature T, and L is the Lorenz number, $L = 2.45{\cdot}10^{-8}\,W{\cdot}\Omega{\cdot}K^{-2}$ [79]. By altering the geometry of the gold structure, this coupling can be adjusted to meet experimental requirements.
The absorber is also directly thermally coupled to the heat bath via the coupling G_{ab}. The main contribution to G_{ab} accounts for the direct thermal coupling of the absorber to the bath through the mechanical mounting of the crystal, resulting in a heat outflow. The expected temperature dependence of this coupling is $G_{ab} \propto T^3$ [93].

4.2.4 Signal Formation

A model for signal formation in cryogenic calorimeters, which encompasses the described processes, has been developed and is elaborated in [93]. Figure 4.2 presents a schematic representation of this thermal model, wherein the detector comprises three weakly coupled sub-systems, each characterised by a heat capacity C and temperature T.
The primary assumption of this model is the categorisation of phonons into two classes, thermal and non-thermal phonons, without considering a continuous frequency distribution. As previously mentioned, due to their strong interaction, the non-thermal phonons entering the thermometer deliver a direct power input $P_e(t)$ on its electron system. Conversely, the thermalisation of the high-frequency phonons in the crystal results in a direct power input into the absorber's thermal phonons $P_a(t)$.

Considering that the heat capacity of the thermometer's phonon system is negligible compared to its electron system, we can introduce an effective coupling between the electrons of the thermometer and the phonons of the absorber (G_{ea}), defined as:

$$G_{ea} = \left(\frac{1}{G_{ep}} + \frac{1}{G_K}\right)^{-1} \tag{4.12}$$

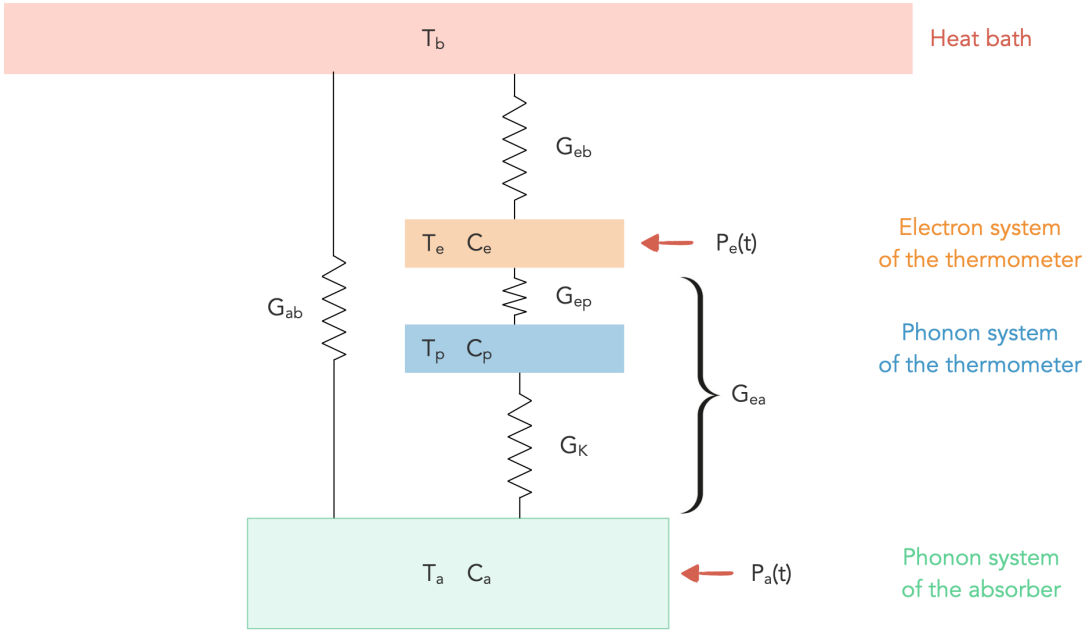

Figure 4.2: Schematic representation of the thermal model of the detector. T_b is the temperature of the heat bath, and T_e and T_a are the temperatures of the thermometer's electron system and the absorber's phonon system, respectively. In contrast, their heat capacities are C_e and C_a. $P_e(t)$ and $P_a(t)$ are the power inputs from the non-thermal phonons into these systems. G_{ea}, G_{eb}, G_{ab}, G_{ep} and G_K are the thermal conductances. Image reproduced from [93].

To model the pulse formation, we assume that a particle interaction in the absorber deposits energy ΔE, generating high-frequency phonons filling the entire absorber volume V_a, with a uniform energy density $\Delta E/V_a$. We consider the thermalisation rate independent of their frequency and let ϵ represent the fraction of phonons thermalised in the thermometer (thus (1-ϵ) is the fraction thermalised in the absorber). We can express the time-dependent power inputs in the electron system of the thermometer and the phonon system of the absorber as:

$$P_e(t) = P_0 e^{-t/\tau_n}, \qquad P_a(t) = \frac{1-\epsilon}{\epsilon} P_e(t) \tag{4.13}$$

where P_0 represents the initial power input to the thermometer and τ_n denotes the effective time constant for the thermalisation of the non-thermal phonon population. The initial power input to the thermometer can be written as

$$P_0 = \frac{\epsilon \Delta E}{\tau_n} \tag{4.14}$$

while the effective thermalisation accounts for two competing effects: the thermalisation in the thermometer and in the crystal, thus:

$$\tau_n = \left(\frac{1}{\tau_{film}} + \frac{1}{\tau_{crystal}} \right)^{-1} \tag{4.15}$$

Where τ_{film} and $\tau_{crystal}$ denote time constants for the thermalisation in the thermometer and crystal, respectively. We can write τ_{film} as:

$$\tau_{film} = \frac{\tau_0}{\bar{\eta}}, \qquad \tau_0 = \frac{2V_a}{A\langle v_\perp \alpha \rangle} \tag{4.16}$$

where $\bar{\eta}$ is the effective absorption probability of the high-frequency phonons transmitted into the thermometer and τ_0 the ideal thermalisation time for ϵ=1 and $\bar{\eta}$=1. We can then define the fraction of phonons thermalised in the thermometer ϵ

$$\epsilon = \frac{\tau_{crystal}}{\tau_{film} + \tau_{crystal}} \tag{4.17}$$

The initial power into the thermometer P_0 exclusively depends on the area of the thermometer and the phonons transmission and absorption probabilities (α and $\bar{\eta}$, respectively)

$$P_0 = \frac{\epsilon \Delta E}{\tau_n} = \frac{\Delta E}{\tau_{film}} \tag{4.18}$$

The simple exponential structure of $P_e(t)$ is a consequence of the assumption of the frequency independence of the thermalisation rate.
After the power inputs $P_e(t)$ and $P_a(t)$, the temperatures of the thermometer's electron systems (T_e) and absorber's phonon system (T_a) increase, and the different thermal couplings then drive their relaxation to the initial condition. The signal formation in the detectors described so far is summarised by two differential equations for the time-dependent temperatures of the sub-systems involved:

$$C_e \frac{dT_e}{dt} + (T_e - T_a)G_{ea} + (T_e - T_b)G_{eb} = P_e(t) \tag{4.19}$$

$$C_a \frac{dT_a}{dt} + (T_a - T_e)G_{ea} + (T_a - T_b)G_{ab} = P_a(t) \tag{4.20}$$

where T_b represents the temperature of the heat bath, and C_e and C_a are the heat capacities of the electrons in the thermometer and phonons in the absorber, respectively. Assuming that at t=0 T_a=T_e=T_b, these equations can be solved for the thermometer signal $\Delta T_e(t) \doteq T_e(t) - T_b$ [93]

$$\Delta T_e(t) = \Theta(t) \left[A_n \left(e^{-t/\tau_n} - e^{-t/\tau_{in}} \right) + A_t \left(e^{-t/\tau_t} - e^{-t/\tau_n} \right) \right] \tag{4.21}$$

where the step function $\Theta(t)$ accounts for the assumption that the homogeneous distribution of non-thermal phonons is formed instantaneously after the energy deposition. This solution has two components: a non-thermal component originating from the direct absorption of non-thermal phonons in the thermometer, with amplitude A_n:

$$A_n = \frac{P_0\left(\frac{1}{\tau_{in}} - \frac{G_{ab}}{C_a}\right)}{\epsilon\left(\frac{1}{\tau_t} - \frac{1}{\tau_{in}}\right)\left(\frac{1}{\tau_{in}} - \frac{1}{\tau_n}\right)}\left(\frac{\frac{1}{\tau_t} - \frac{G_{ab}}{C_a}}{G_{eb} - \frac{C_e}{C_a}G_{ab}} - \frac{\epsilon}{C_e}\right) \tag{4.22}$$

and a thermal component, generated by the temperature rise of the absorber as measured by the thermometer, with amplitude A_t:

$$A_t = \frac{P_0\left(\frac{1}{\tau_t} - \frac{G_{ab}}{C_a}\right)}{\epsilon\left(\frac{1}{\tau_t} - \frac{1}{\tau_{in}}\right)\left(\frac{1}{\tau_t} - \frac{1}{\tau_n}\right)}\left(\frac{\frac{1}{\tau_{in}} - \frac{G_{ab}}{C_a}}{G_{eb} - \frac{C_e}{C_a}G_{ab}} - \frac{\epsilon}{C_e}\right) \tag{4.23}$$

There are three time constants involved in the thermometer signal:

- τ_n: the lifetime of non-thermal phonons, describing their thermalisation, as described in equation 4.15;
- τ_{in}: the thermal relaxation time of the thermometer;
- τ_t: the thermal relaxation time of the absorber.

We can define two constants, a and b:

$$a = \frac{G_{ea} + G_{eb}}{C_e} + \frac{G_{ea} + G_{ab}}{C_a}, \qquad b = \frac{G_{ea} + G_{eb} + G_{ea} + G_{ab} + G_{eb} + G_{ab}}{C_e C_a} \tag{4.24}$$

and express the thermal relaxation times of the thermometer and the absorber as:

$$\tau_{in} = \frac{2}{a + \sqrt{a^2 - 4b}}, \qquad \tau_t = \frac{2}{a - \sqrt{a^2 - 4b}} \tag{4.25}$$

For the detectors used in CRESST, the heat capacity of the thermometer is much smaller than that of the absorber ($C_e \ll C_a$) and the thermal coupling between phonons and electrons is strongly suppressed ($G_{ea} \to 0$) because of the low operating temperature ($\sim 15\,\mathrm{mK}$). Therefore, we can write the time constants as:

$$\tau_{in} \approx \frac{C_e}{G_{eb}}, \qquad \tau_t \approx \frac{C_a}{G_{ab}} \tag{4.26}$$

In light of this, the thermometer's relaxation time can be controlled by the thermal conductance of the thermometer to the heat bath, defined by the gold thermal link between the metal film and the bath. The coupling between the absorber and the heat bath instead defines the absorber's relaxation time.
The thermometers described by this model can be operated in two modes, depending on the ratio of τ_{in} to τ_n, which controls the character of the non-thermal component: bolometric and calorimetric mode.

Bolometric Mode

A thermometer for which $\tau_{in} \ll \tau_n$ is a bolometer. In such a detector, A_n is positive, indicating that the phonons flow out of the thermometer faster than they flow into it. Here, τ_{in} represents the rise time and τ_n the fast decay time of the signal. The amplitude of the non-thermal component is:

$$A_n \approx \frac{P_0}{G_{eb}} = \frac{\epsilon \Delta E}{\tau_n G_{eb}} \tag{4.27}$$

Thus, the amplitude of the non-thermal component is directly proportional to the initial power input in the thermometer. Bolometers are designed to measure the flux of non-thermal phonons in the thermometer. In this mode, the thermal component rises with the time constant τ_n and decays with the time constant τ_t.

Calorimetric Mode

A thermometer for which $\tau_{in} \gg \tau_n$ is a calorimeter. In such a detector, A_n is negative, indicating that the phonons flow faster into the thermometer than they flow out of it. The thermal relaxation time τ_{in} is sufficiently long for the thermometer to integrate over the non-thermal phonons power input $P_e(t)$, with a lifetime of τ_n. The amplitude of the non-thermal component is given by:

$$A_n \approx -\frac{\epsilon \Delta E}{C_e} \tag{4.28}$$

Moreover, in this mode, the thermometer measures the total energy of the high-frequency phonons absorbed in the thermometer, hence the name "calorimetric mode". The heat capacity of the thermometer plays a crucial role in determining the non-thermal signal amplitude.
In calorimetric mode, the lifetime of the non-thermal phonons defines the rise time of both the thermal and the non-thermal components. The decay time of the latter is defined by τ_{in}, while τ_t represents the decay time of the thermal component.

4.2.5 Phonon Collectors

In calorimetric mode, when the thermometer's dimensions are minimised to the point where the effective lifetime of the non-thermal component of the signal is governed by $\tau_{crystal}$ (i.e. when $\tau_{film} \ll \tau_{crystal}$, such that from eq. 4.15 we obtain $\tau_n \to \tau_{crystal}$), the amplitude of the non-thermal signal component becomes independent of the thermometer's size. However, decreasing the thermometer's dimensions results in a lowered film's heat capacity and, thus, an enhanced signal. The thickness of the W thin film is typically chosen around 180-200 nm to ensure an efficient absorption of non-thermal phonons. Therefore, the only remaining possibility is to reduce its area. This, however,

comes at the cost of a reduction of the phonon collecting surface, which counteracts the potential gain due to the decreased heat capacity. In this limit, the signal can be enhanced by reducing the W area, and with it the heat capacity of the sensor, and by incorporating at the same time phonon collectors. These collectors consist of superconducting metal films (in CRESST-III, typically made by a bilayer of 180-200 nm of W and 1 μm of Al) with a transition temperature much higher than the operating temperature, which therefore possesses a negligible heat capacity. They can absorb non-thermal phonons and transmit their energy to the thermometer, thereby enhancing the signal without increasing the sensor's heat capacity [101].
Non-thermal phonons reaching the phonon collectors contribute to the signal through their interaction with the Cooper pairs of the superconducting materials. Phonons with energies higher than twice the band gap (Δ) of the chosen superconducting material can break the Cooper pairs into quasiparticles (similar to free electrons). The quasiparticles created in this process propagate in the material, losing energy through the spontaneous emission of phonons. As long as these emitted phonons have energies above $2 \cdot \Delta$, they can break additional Cooper pairs and enhance the quasiparticle signal. When the created quasiparticles have energies below $2 \cdot \Delta$, they emit sub-gap phonons that cannot break Cooper pairs and that dominantly diffuse back to the main absorber, resulting in a partial loss of the energy initially transmitted by non-thermal phonons. Accounting for these processes, the theoretical phonon collection efficiency for the conversion of an energy E to a quasiparticle population has been computed to be $E/1.68$ [102].
However, there are other processes that can contribute to the signal loss. The quasiparticles generated in the collectors have to diffuse to (or stay in) regions where they can interact with the electron system of the TES to contribute to the measured temperature signal in the TES. Among the signal loss mechanisms, the recombination of quasiparticles to Cooper pairs before their interaction with the electron system of the phonon collectors is the dominant one [103]. Impurities in the collector material tend to collect and trap quasiparticles, lowering their diffusion length and leading to recombinations to Cooper pairs, which results in a signal loss.
Thus, the phonon collectors efficiency is strongly related to the diffusion properties of the quasiparticles in the chosen collectors material and to their lifetime therein. The thickness and the quality of the material used as phonon collectors are crucial in defining the efficiency of the system in collecting phonons.
Once the quasiparticles reach the thermometer (having a zero energy gap), they relax by releasing their energy in the thermometer's electron system, increasing its temperature.

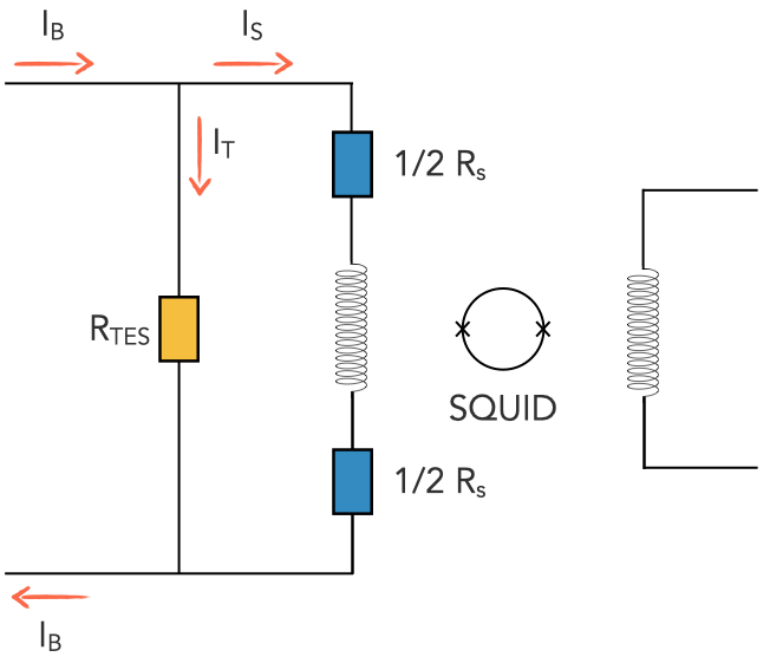

Figure 4.3: Schematic representation of the readout circuit used to measure the thermometer resistance R_{TES}. A constant bias current (I_B) is sent through two parallel branches, one with the thermometer and the other one with two shunt resistors for a total resistance of R_S and the input coil of the SQUID. The current flowing through the thermometer branch is I_T, while T_S denotes the current flowing through the SQUID. The output voltage of the SQUID is proportional to the current flowing through its input coil.

4.3 SQUID readout

The readout of the thermometer's signal is accomplished using a Superconducting QUantum Interference Device (SQUID), which measures the variations in the resistance of the metal film resulting from changes in its temperature.
A constant bias current (I_B) is supplied by a current source and divided between two parallel branches. One branch includes the detector, characterised by a temperature-dependent resistance ($R_{TES}(T)$), while the other contains the shunt resistors (with a total constant resistance of R_S) connected in series with the input coil of the SQUID. A SQUID consists of two Josephson junctions connected in parallel on a superconducting loop. Figure 4.3 depicts the readout scheme employed in CRESST and in this work.
The current flowing into the SQUID branch can be expressed as:

$$I_S = I_0 \frac{R_{TES}(T)}{R_{TES}(T) + R_S} \tag{4.29}$$

As a result, any change in the resistance of the thermometer leads to a corresponding variation in the branching of the bias current, which the SQUID then measures. Following an energy deposition in the absorber, the resistance of the thermometer increases; thus, I_S increases as well. Consequently, this change induces a variation in the magnetic flux coupled to the SQUID via the input coil. The SQUID essentially is a flux-to-voltage transducer, converting this magnetic flux variation into an output voltage. This output voltage exhibits periodicity with respect to the applied magnetic flux Φ, with the period of one quantum flux $\phi_0 = h/2e \approx 10 \cdot 10^{-15}$ Wb [104]. In CRESST, these devices are operated in flux-locked mode, where a separate feedback coil maintains the flux through the SQUID loop constant, effectively eliminating the periodicity of the response. In this mode, the output voltage of the SQUID is linearly related to the applied magnetic flux (defined by I_S):

$$V_{out} = \xi \left(\Phi + n\Phi_0\right) \tag{4.30}$$

where ξ denotes the flux to voltage transfer coefficient of the SQUID system. By employing this technique, changes in flux ranging from much less than a single flux quantum to many flux quanta can be accurately measured. However, the main limitation of this mode stems from the existence of a sequence of stable points resulting from the periodicity of the SQUIDs. Consequently, the maximum rate of flux change that the feedback electronics can compensate for (slew rate) is limited. If a signal surpasses the slew rate of the feedback electronics, it can induce an offset in the readout voltage of a factor $\xi n\phi_0$ (i.e. a flux quantum loss), leading to a different baseline of the SQUID after the event. Nonetheless, these devices offer exceptional sensitivity and thus represent a particularly advantageous choice for reading out the signals produced by superconducting thermometers.
In CRESST, commercially available DC-SQUIDs are used, mounted in the liquid helium dewar of the cryostat, and connected to the detectors via twisted pairs of superconducting wires.

4.4 Noise

The presence of noise originating from diverse sources has the potential to limit the performance of cryogenic detectors. A theoretical model addressing the noise observed in CRESST was developed in [105]. A brief overview of the various contributions to noise in CRESST will be given below.

Thermal Noise Thermal or phonon noise arises from random energy fluctuations among the detector's sub-systems. The main contribution to this noise component comes from random energy exchanges in the thermal link connecting the thermometer to the heat bath, leading to fluctuations in the thermometer's temperature.

Johnson-Nyquist Noise This type of noise originates from the thermometer, the shunt resistance, and the SQUIDs.
The thermometer and the shunt resistors essentially are resistors, where electrons undergo random motion due to thermal agitation. These agitations manifest as Johnson-Nyquist noise, independent of the applied bias current. The shunt resistances are installed in the cryostat and thermally coupled to the heat bath to minimise these thermal agitations and, consequently, the noise.
The Josephson junctions of DC-SQUIDs incorporate thin-film shunt resistors in parallel, which generate Johnson-Nyquist noise in the SQUID loop. This noise component is solely dependent on the characteristics of the SQUIDs.

$1/f$ Noise A $1/f$ noise is observed in these types of detectors, and it seems to be related to local resistance fluctuations in the thermometer film on a microscopic scale [106]. For instance, these fluctuations may stem from defects or stress in the lattice structure. This noise dominates at low frequencies and tends to increase for operating points in the lower part of the superconducting transition. For further insights, refer to [83, 105, 106].

Other Noise Sources Various external factors can introduce additional noise into the detectors. External disturbances, like magnetic field variations, electrical interferences, vibrations, or temperature fluctuations of the heat bath, are among the potential noise sources. The experimental setup in CRESST is meticulously designed to minimise these contributions. Measures such as shielding against magnetic fields, employing stable electrical connections, dampening vibrations, and actively controlling the temperature of the heat bath help minimise external disturbances.

Chapter 5

Optimisation of CRESST sensor design

In order to further extend the physics reach of the CRESST experiment, various studies were performed aiming to fine tune the sensor design. Specifically, these studies targeted the collection efficiency of the phonon collectors. Thus, different aspects, like the geometry, composition and thickness of the material were studied. The first part of this chapter summarises the results of these tests. Later on, an innovative design of the sensor design aiming to shield external magnetic field is presented. The chapter concludes by presenting future prospects in achieving more sensitive sensors for the CRESST experiment.

5.1 Motivation

The CRESST III detectors reached extremely low energy threshold of 30 eV for nuclear recoils, which led to an unprecedented sensitivity to dark matter particles down to a mass of 160 MeV. Continuous efforts are underway in CRESST aiming at achieving a better signal to noise ratio, and an even better sensitivity. In this regard, CRESST is continuously working on reducing the background, fine tuning analysis techniques and developing detector with lower and lower thresholds.
Figure 5.1 presents an overview of the dependencies of the pulse model parameters on the detector properties, based on the model developed in section 4.2. As it can be seen from the Figure, the model accounts for numerous variables, depending on many characteristics of both, the absorber crystal and the thermometer. These parameters are interconnected with non-linear equations, making the optimisation and design of improved detectors a very challenging task.

Starting from the in-depth study that conducted to the thermal model [93], numerous investigation have been performed within CRESST with the aim of enhancing the detectors' sensitivity. In [107], the properties of quasiparticles diffusion in aluminium

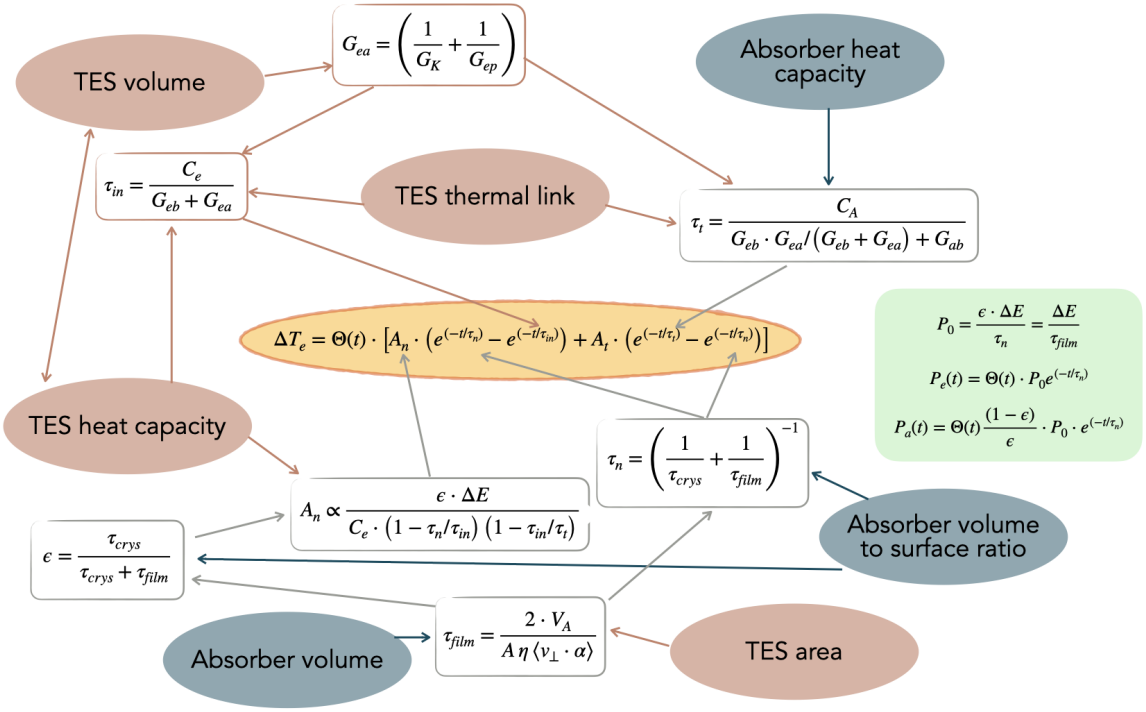

Figure 5.1: Overview of the parameters describing the thermal model of our cryogenic calorimeters based on superconducting thermometers, described in section 4.2. The dependencies of each parameter on TES and absorber characteristics are highlighted. Image reproduced from [107].

are studied to assess the efficiency of the phonon collectors. In [108] the dimensions of the TES are investigated, along with the properties of the thermal link.
Given the complexity of the system, in this work, we decided to perform multiple test, each targeting a specific aspect of the design, to break the complex scheme in Figure 5.1 into small pieces, easy to address.
We developed an experimental procedure to be followed in each of the tests, optimised for comparing results of differently designed sensors.

5.2 Standard CRESST sensor

It is crucial to assess the current state of the art in sensor design and production, before diving into the various modifications attempted to further optimise the sensors. The various stages of the production of a standard CRESST III TES are shown in Figure 5.2.
This design was the result of extensive studies, presented in [83]. These studies were

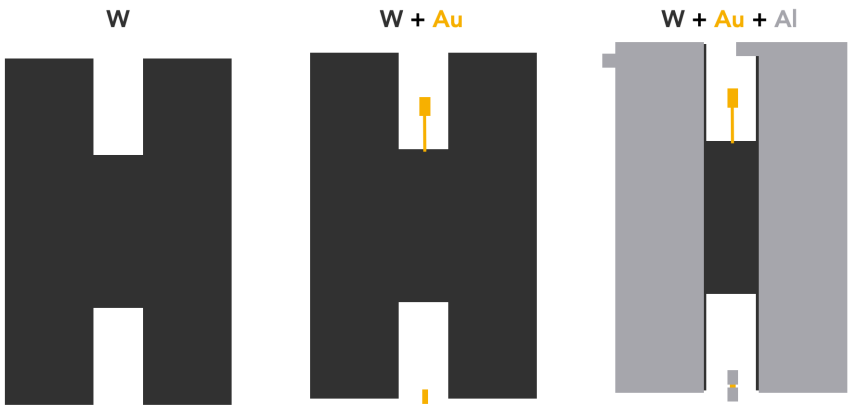

Figure 5.2: Schematic representation of the production steps to structure a TES in its standard design for CRESST.

performed during the transition from the CRESST II to the CRESST III Phase. For the latter, the crystals dimensions were drastically reduced by a factor 10, to allow for reaching a lower energy threshold [83]. The dimensions of the thermometer were also reduced, to match the new crystal size. In CRESST III, the detectors are operated in calorimetric mode, which benefits from very small thermometer dimensions and from the presence of phonon collectors. These phonon collectors, made of aluminium in CRESST, allow for enhanching the signal collection, without adding to the heat capacity of the sensors, as detailed in section 4.2.5.

The TES production process (see Figure 5.2) begins with the deposition of a H-shaped tungsten (W) film, with a thickness of ∼180-200 nm. This superconducting film is itself the thermometer. More details about the possible W deposition processes are given in chapter 6. The second step of the sensor's production consists in the deposition of gold (Au) for the thermal link and its bondpad and for the heater. The thermal link is the thermal connection between the TES and the heat bath and its properties are fundamental, because they define the thermal coupling between the two, as discussed in section 4.2. A gold wire connects the thermal link to the heat bath, allowing for the thermal relaxation of the sensor to its operating temperature after a particle interaction. The heater element is essentially a transistor, where a current can be injected. Injecting a constant current flow in the heater, we can stabilise the TES in the middle of its transition. The last element to be deposited is aluminium (Al). This material is deposited though an electron beam evaporation, with a thickness of 1 μm and it is used for the bondpads of the heater element, and for the phonon collectors. As aforementioned, the phonon collectors are essential to our sensors, as they enhance the signal collecting the athermal phonons generated in particle interactions in the crystal,

without adding to the heat capacity of our sensors. Indeed, Al is superconducting below 1.2 K, and therefore at our operating temperature ∼15 mK its heat capacity is negligible. The phonon collectors also serve as bondpads to allow for the electrical connections of our sensor.

5.3 Experimental Procedure

Since this is a comparative study, aiming at comparing different sensors designs to find the optimal one in terms of sensitivity, it is very important to follow a strict experimental methodology, to ensure the independence of the results from other experimental variations which are not under investigation. Because of this, we devised an experimental procedure and followed the same procedure for all our tests. We identified two main sources where we could introduce systematic errors: fabrication and data taking.

Fabrication Comparing results of different sensors types is challenging, due to the fact that experimental conditions (such as production parameters, or measurement noise conditions) may change. To avoid the introduction of such uncertainties, testing all the detectors to be compared in a study in one single measurement is fundamental. Furthermore, producing sensors on different crystals might also lead to uncertainties that are not quantifiable, due to both, the possible differences in the crystals structures and surfaces and the differences in the deposition processes.
Keeping all of this in mind, we decided to deposit different sensors to be compared on the same absorber crystal. This choice aims at minimising the variations originating from the deposition process and from the measurements.

Data Taking The ultimate figure of merit for our comparative studies is the energy threshold of the final detector that we aim at after carrying out all the optimisations. The energy threshold of any particular detector is driven by the signal-to-noise ratio of the detector. The signal in our case is a change in voltage per unit energy deposition, i.e. mV/keV. But this can not directly be used to compare performance of different detectors, simply because different conditions during measurement (e.g. noise, or SQUIDs characteristics) have a strong influence on the result.
On the other hand, if one can extract the true temperature rise per unit energy deposition, that would be a fundamental characteristics of the detector and hence it could be used to compare performance of different detectors. The temperature rise per unit energy deposition can be extracted from mV/keV by using the transition curve of the detector, as will be detailed in the following.
For such a comparison, having a known energy deposition (to be used as our unit energy) is fundamental. To this scope, we utilise ^{55}Fe as a calibration source, emitting two X-rays at 5.89 and 6.49 keV in its decay (see section 7.3.6 for more details). It should be pointed out that, since we have multiple sensors on the same substrate, it

is unavoidable that they interfere with each others' measurements. To minimise this effect, we only inject a bias current through one sensor at a time, keeping the other sensors unbiased. Indeed, a bias current injected in the sensor directly injects power to the absorber thereby altering its temperature.
The measurement protocol comprises two phases: in a first phase we record the transition curve of a single detector, and in a second phase we collect data to obtain an energy spectrum, where the peaks of the ^{55}Fe calibration source are well distinguishable. To record the transition curve of a sensor, we perform a slow temperature sweep of the mixing chamber temperature. The mixing chamber is very slowly warmed up and subsequentely very slowly cooled back down to its base temperature, using a dedicated heater. The resistance of the tungsten thin film is recored throughout this procedure.
For the second phase, we collect data with each sensor individually. To minimise the measurements differences, we apply the same bias current to each of the studied TES. From the data, we can extract the saturation value and therefore infere the operating point of the detector in the transition curve previously recorded, via:

$$V_{OP} = V_{TOT} - V_{SAT} \tag{5.1}$$

where V_{OP} represents the operating point, V_{TOT} is the total amplitude of the transition curve measured with the same bias used to collect data, and V_{SAT} denotes the amplitude of saturated pulses in volts.
To evaluate the temperature rise due to the energy deposition of the 5.89 keV X-rays from the calibration source, we firstly evaluate the amplitude of this peak in the spectrum. Then, we exploit the transition curve to infer the corresponding temperature variation in the TES, as shown in Figure 5.3.

5.4 R&D on optimisation of new sensor designs

Different aspects of the current sensor design could be further optimised, to get more sensitive detectors. Among those, the heat capacity of our sensors could be reduced, employing thinner tungsten films, or the thermal link could be optimised, ensuring a long enough integration time of the power input, the phonon collectors themselves could be optimised in terms of their geometry, thickness, material composition, etc., and finally the sensors could be shielded from external magnetic fields. In this study, we focused on studying different phonon collectors, by studying the effect of their thickness, geometry and material composition (single layer of aluminium or bilayer of tungsten and aluminium as in the present design) on the thermometers' sensitivity.
Optimising the design of the phonon collectors is a non-trivial task.
The distance a quasiparticle travels by diffusion within a time t can be computed as:

$$L(t) = \sqrt{\frac{\langle v_g \rangle \ell_q t}{3}} = \sqrt{Dt} \tag{5.2}$$

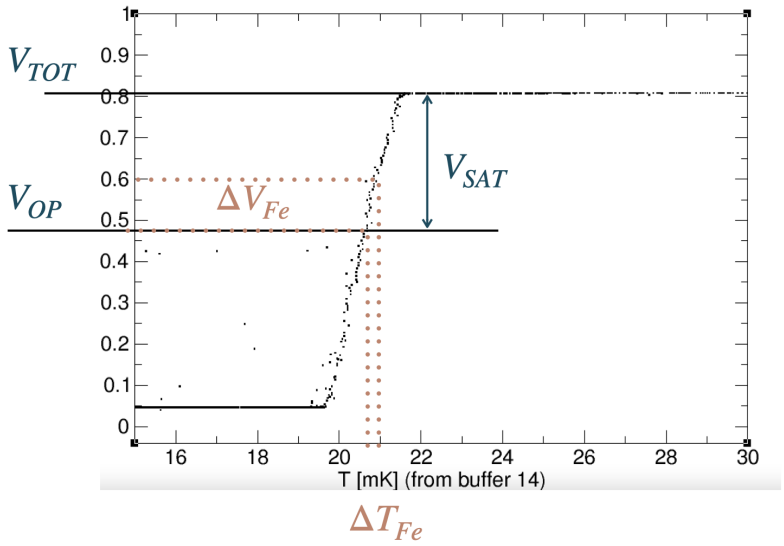

Figure 5.3: Schematic representation of the procedure to evaluate the rise of the sensors' temperature due to the energy deposition of the 5.89 keV X-ray emitted by the ^{55}Fe source.

where ℓ_q denotes the mean free path of quasiparticles, $\langle v_g \rangle$ represents their group velocity at the detector's operating temperature and D is the diffusion constants. The mean free path of quasiparticles is determined by the elastic scattering on impurities and lattice defects, and, if the thickness of the collectors is comparable to ℓ_q, by surface scatterings. Thus, high quality aluminium films are necessary to maximise the diffusion length of quasiparticles. This diffusion length determines the maximum size of phonon collectors, and it is also influenced by the film thickness. If the diffusion length of the quasi-particles is smaller than the distance they have to travel before reaching the thermometer, the signal will be degraded. On the other hand, too small phonon collectors might be ineffective.
Recent studies (see [107, 108]) showed that there is room for improvement, and that the design of the sensors need to vary when employing different absorber crystals.
Many aspects of the sensors design can still be studied, taking into account the characteristics of the system under investigation, e.g. the quasi-particles diffusion lengths in different materials, or the phonon relaxation time in the crystal.

5.4.1 Phonon Collectors Thickness

The thickness of the phonon collectors is one of the factors determining the phonon collection efficiency of our sensors. They should be thick enough, to maximise the phonon collection efficiency, but they should not be too thick, as it would imply increased

technical difficulties (especially concerning the evaporation process), while the number of surface scattering the quasi-particles undergo before reaching the thermometer would not be strongly influenced. This matter was already discussed in [107], in the context of studying the quasiparticle diffusion in superconducting phonon collectors. This work advises for an increase in the phonon collectors thickness, supported by the experimental studies presented, and by the findings of Yen et al. [109].
Following the results presented in [107], a first study on the thickness of phonon collectors was presented in [110], resulting in an improvement in the detector's performance when increasing the thickness of the aluminium in the phonon collectors from 1 μm to 3 μm. The choice of 3 μm for the thick phonon collectors was motivated by the studies in [107] showing that at this thickness the plateau in collection efficiency is reached.
In the setup described in [110], the ^{55}Fe calibration source was placed closer to the sensors with thicker phonon collectors. This could mimic an artificially higher temperature rise on the sensors with thicker phonon collectors if there is some position dependence. Therefore, we decided to begin our systematic study starting from the phonon collector thickness, repeating the test presented in [110].
For this test we used the same sample used in [110] (see Figure 5.4), presenting the four TES deposited on a $20\times20\times0.4\,\mathrm{mm}^3$ silicon-on-sapphire (SOS) crystal. The two TES with thin phonon collectors are named TES-thin1 and TES-thin2, while the two sensors with thick phonon collectors are named TES-thick3 and TES-thick4. The ^{55}Fe

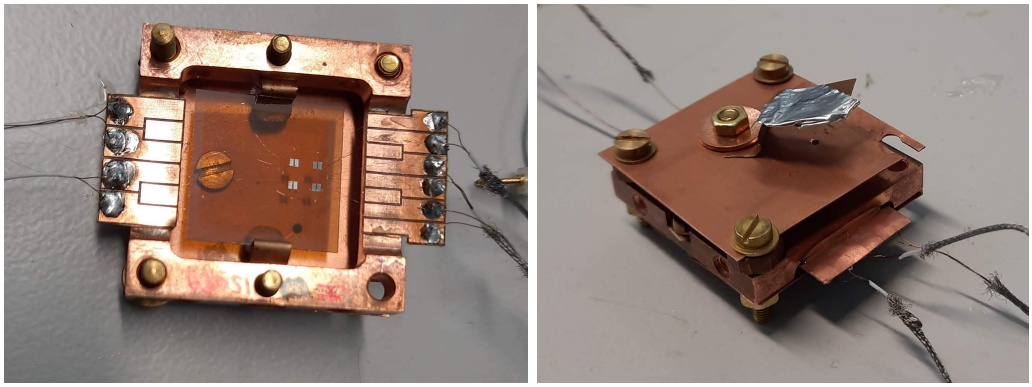

Figure 5.4: *Left:* Photo of the sample used for this test. The two TES on the left (TES-thick3 and thick4) are the two TES with 3 μm phonon collectors and the two TES on the right (TES-thin1 and thin2) are the sensors with 1 μm thick phonon collectors. *Right:* Photo of the fully assembled module for testing. The ^{55}Fe source is shining though a hole in the lid, in between the two types of sensors.

source is placed in between the thick and thin sensors, at the same distance from both and closer to TES-thin1 and TES-thick3 than TES-thin2 and TES-thick4. This allows us to study the impact of the distance from the source on the signal and on the result.

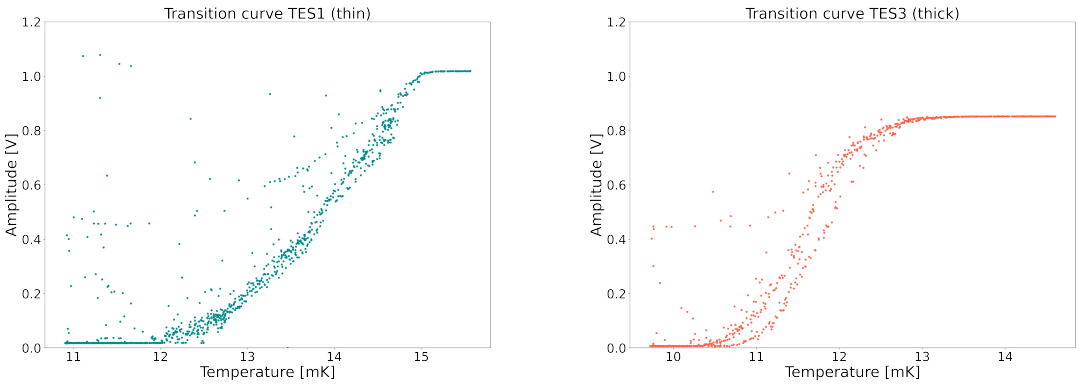

Figure 5.5: *Left:* Transition curve of TES-thin1. *Right:* Transition curve of TES-thick3.

If the two sensors closer to the ^{55}Fe source appear to have an improved performance with respect to the other two TES, this would give a clear indication of a dependence of the performance on the distance from the source.

Results The analysis follows the procedure detailed in section 5.3. The test was conducted in the above ground facility of the Max Planck Institute for Physics in Munich, in a Leiden dilution refrigerator named "Cryo2". The bias chosen for these measurements is 200 nA.
The transition curves of TES-thin1 and TES-thick3 can be found in Figure 5.5, while the template pulses obtained by averaging pulses caused by energy deposits in the abosrber crystal by a 5.89 keV emitted by the ^{55}Fe source can be found in Figure 5.6.

Following our experimental procedure we obtain the following results:

- TES-thin1: $\Delta T = (22.84 \pm 0.14)\,\mu K$
- TES-thin2: $\Delta T = (13.62 \pm 0.04)\,\mu K$
- TES-thick3: $\Delta T = (43.32 \pm 0.10)\,\mu K$
- TES-thick4: $\Delta T = (43.81 \pm 0.04)\,\mu K$

While the effect of the thickness of the film on the result is evident, we cannot clearly see an effect of the distance of the sensor from the source. Indeed, a particle coming from the iron decay causes roughly the same temperature variation in the two thick samples and a similar variation for the two thin ones. Despite being slightly different among each other, the variations in the temperature rises of two thin samples are clearly smaller than those between the two types of samples.

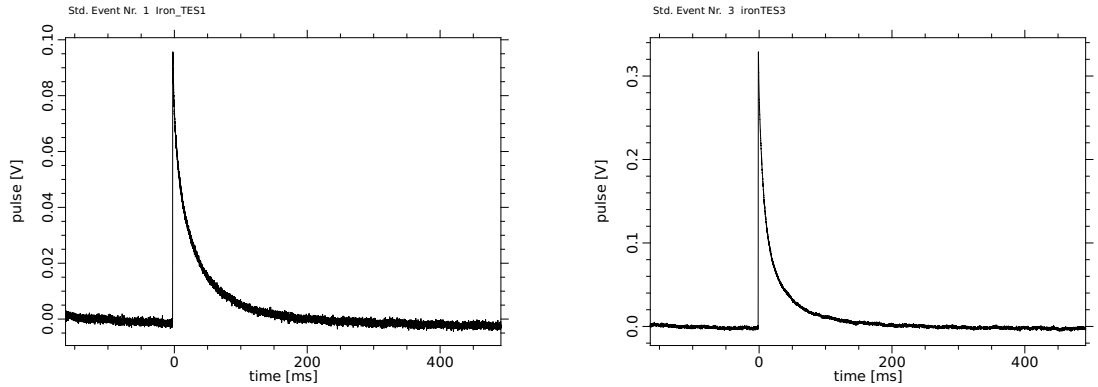

Figure 5.6: Template pulses obtained by averaging the 5.89 keV pulses of the ^{55}Fe source. *Left:* Template pulse of TES-thin1. *Right:* Template pulse of TES-thick3.

Using these measurements we were able to draw some conclusions concerning the ideal thickness of phonon collectors. We realised that increasing the thickness of Al phonon collectors from 1 μm to 3 μm is beneficial, as it results in an increase in sensitivity of roughly a factor 2.39±0.02. This result is in strong agreement with the result obtained in [110], which observed an factor 2.3 higher temperature rise using thicker phonon collectors. This agreement also hints towards an independence of the results from the location of the radioactive source.

5.4.2 Phonon Collectors Architecture

As aforementioned, there are multiple aspects concerning the phonon collector design, which could be optimised for enhancing our detectors' sensitivity. Among those, the material composition and geometry of the phonon collectors surely play an important role and they are discussed in the following.

Single Layer or Bilayer Phonon Collectors

As explained in section 5.2 (see also Figure 5.2), in the standard CRESST III sensors an aluminium layer is deposited on top of the tungsten and acts as a phonon collector. Given the reduced thickness of the tungsten (∼200 nm) compared to that of aluminium (1 μm), the transition temperature of this bilayer is shifted towards the aluminium transition temperature (1.2 K), due to proximity effects [111] (more details in section 5.4.3). As a consequence, the contribution of the phonon collectors to the total sensor's heat capacity becomes vanishingly small at the operating temperatures (W-T_C).

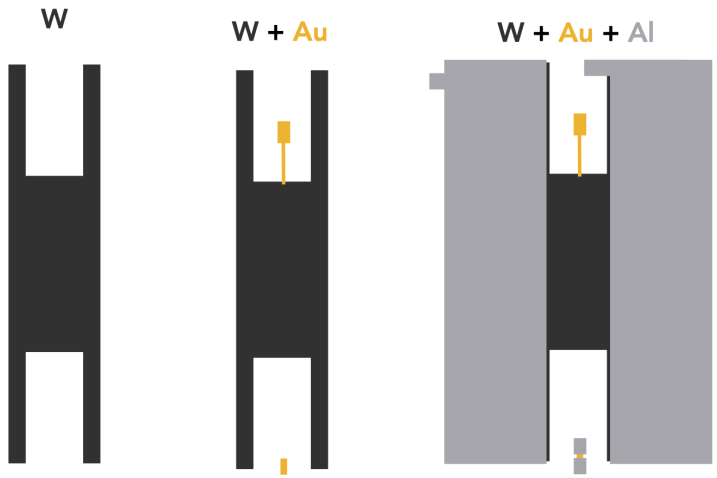

Figure 5.7: Schematic representation of the production steps to structure a TES with single layer phonon collectors.

In this test, we aim at comparing the performance of the standard CRESST TES design, with those of single layer TES. In the latter type of sensors, there is no tungsten below the aluminium of the collectors, which are made of pure aluminium. The production steps for the single layer TES and its design are schematically represented in Figure 5.7.
We have experimentally observed that the pulse shapes of the single layer and bilayer sensors significantly differ. For instance, the pulses rise time is systematically smaller in single layer detectors.
This motivated our study, aimed at understanding the differences in the behaviour of the two different sensors compositions and their impact on the overall performance of our TES.

For this test we deposited four sensors on one single $10\times20\times5\,\mathrm{mm}^3$ Al_2O_3 crystal, two with the standard bilayer design and two with the single layer design. Both types of sensors have $1\,\mu$m thick phonon collectors.
The measurement was performed in Cryo2 and the sensors were individually biased with a current of 500 nA. During the cooldown, the electrical connection to the heater on the crystal was broken. To stabilise the sensors during operation, a high current was sent through one of the TES, such that it worked as a heater.
The TES with single layers phonon collectors are named TES-SL1 and TES-SL2, while the two standards sensors (bilayer) are called TES-BL3 and TES-BL4.

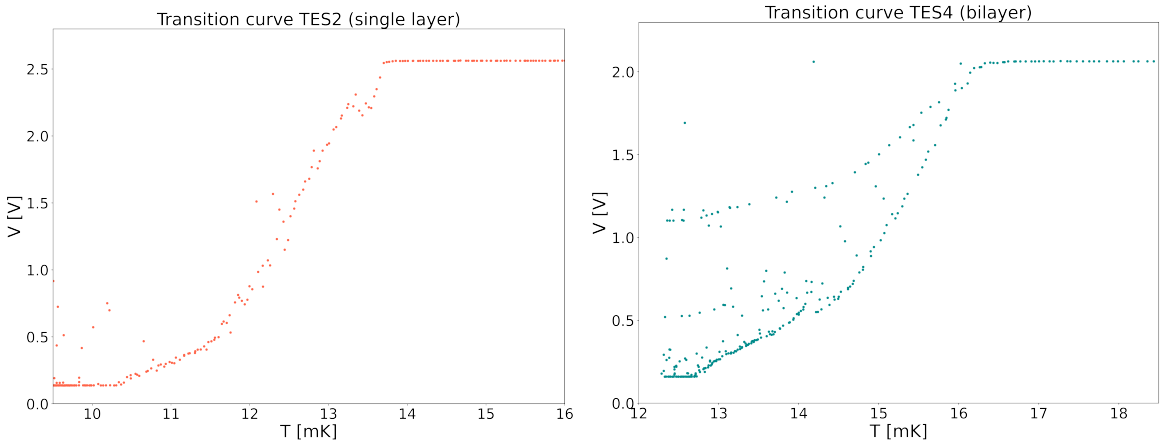

Figure 5.8: *Left:* Transition curve of TES-SL2. *Right:* Transition curve of TES-BL4.

Results The transition curves of TES-SL2 and TES-BL4 are shown in Figure 5.8, while the averaged pulse shapes of TES-SL1 and TES-BL3 are shown in Figure 5.9.

Employing the information obtained for the four sensors we obtain the following:

- TES-SL1: $\Delta T = (199.80 \pm 0.73)\,\mu K$
- TES-SL2: $\Delta T = (157.37 \pm 4.21)\,\mu K$
- TES-BL3: $\Delta T = (54.74 \pm 0.66)\,\mu K$
- TES-BL4: $\Delta T = (101.74 \pm 1.07)\,\mu K$

These results hint towards an improvement in the sensors' performance when produced in the single layer design.
During this measurement, TES2 faced some issue, mostly due to a very high noise level. The relative error on its ΔT ($\sim$2.6%) is slightly higher than that of the other sensors ($\sim$1%).

Based on the results of this test, we can recommend the employment of a single layer of aluminium as phonon collectors for future CRESST sensors on Al_2O_3 substrates.

Single Layer Phonon Collectors Thickness

In summary, the previous tests suggest an enhancement in sensitivity for 3 μm thick phonon collector sensors and an enhancement for the sensors featuring single layer aluminium phonon collectors, as compared to the standard CRESST design.
As a natural next step, to rule out a common source behind the enhancement in

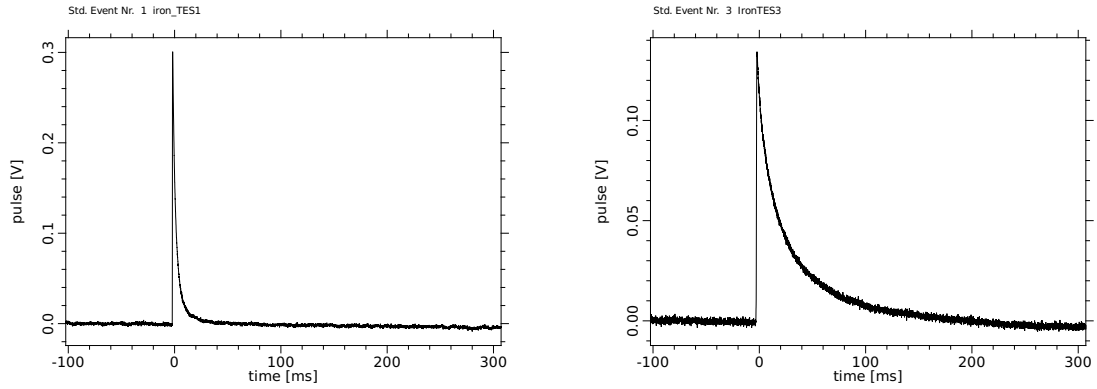

Figure 5.9: Template pulses obtained by averaging the 5.89 keV pulses of the ^{55}Fe source. *Left:* Template pulse of TES-SL1. *Right:* Template pulse of TES-BL3.

sensitivity in the previous test and to assess the total improvement we could obtain optimising the design, we decided to combine the two tests and compare sensors with a single layer of 1 μm thick aluminum phonon collectors with sensors witg a single layer of 3 μm thick aluminum phonon collectors.
With this motivation, four sensors were fabricated on a $20\times10\times0.4\,\mathrm{mm}^3$ silicon-on-sapphire substrate, two per type. The sensors were deposited on the sapphire side, to be consistent with the previous tests. A picture of the final setup mounted on the mixing chamber of the Cryo2 before testing is shown in Figure 5.10.
The two sensors with the thin phonon collectors are named TES-SLthin1 and TES-SLthin2, while the ones with the thick collectors are called TES-SLthick3 and TES-SLthick4. An iron source is placed on the bottom plate, at an equal distance from the two types of sensors, but closer to TES-SLthin1 ans TES-SLthick3. A bias current of 800 nA was chosen for this measurement.

Unfortunately, in this test the channels with TES-SLthick3 and TES-SLthick4, i.e. both the sensors with thicker phonon collectors, had unforeseen issues. The channel with TES-SLthick4 had a much smaller voltage output than normal and the channel with TES-SLthick3 was very noisy (see Figure 5.12 *left*). Irrespective of this, identifying the iron peak on the energy spectra of TES-SLthin1 and TES-SLthick3 was possible, thus we could extract the corresponding ΔT. Nonetheless, some degree of uncertainty is present in this measurement.

Results The analysis follows the standard procedure described in section 5.3. The transition curves of TES-SLthin1 and TES-SLthick3 are shown in Figure 5.11, while their template pulses are shown in Figure 5.12.
From these data, we obtain that with the sample with thin phonon collectors we have

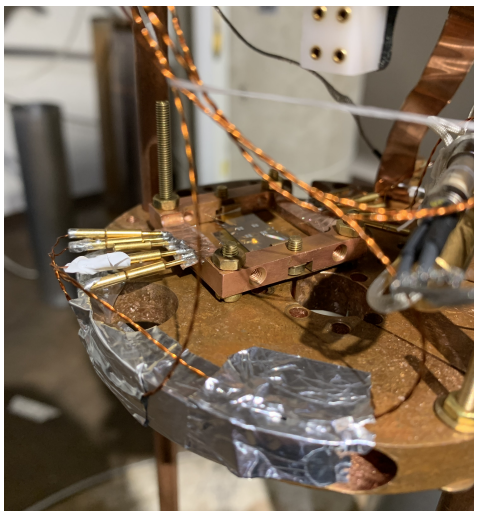

Figure 5.10: Picture of the sample for the test on the thickness of the single layer phonon collectors mounted on the cryostat plate.

an temperature rise of roughly 900 μK, while with the thick one we compute an increase of roughly 750 μK.
Although a very similar performance was observed on TES-SLthin1 and TES-SLthick3, it is not sufficient to draw a final conclusion, given the very different noise conditions of the only two sensors we could compare. So far, we have indications that single layers phonon collectors could be a game changer for our TES on Al_2O_3, improving significantly their performance. Employing this single layer design, we might not need to have 3 μm thick phonon collectors, as this test hints towards a similarity in performance. Further testing is recommended to explore this potential similarity in performance.

Phonon Collectors Size

While the standard CRESST TES design is the outcome of intensive studies, many aspect of the sensors design have changed through the years, therefore, there is a need to address all of the aspects of the phonon collectors design for a better understanding of how to improve the detectors' sensitivity.
One very crucial aspect of the sensor design is the geometry of the phonon collectors. Suboptimal sizing of phonon collectors invariably leads to signal losses. Smaller collectors may fail to capture all phonons, leaving some signal uncollected. Conversely, larger collectors risk losing quasi-particles generated within them due to their finite diffusion lengths. Hence, an optimisation of the phonon collector geometry is of paramount importance.

A litography mask with the possibility of depositing TES with four different phonon collectors dimensions has been produced and it is shown in Figure 5.13 (*left*). The TES

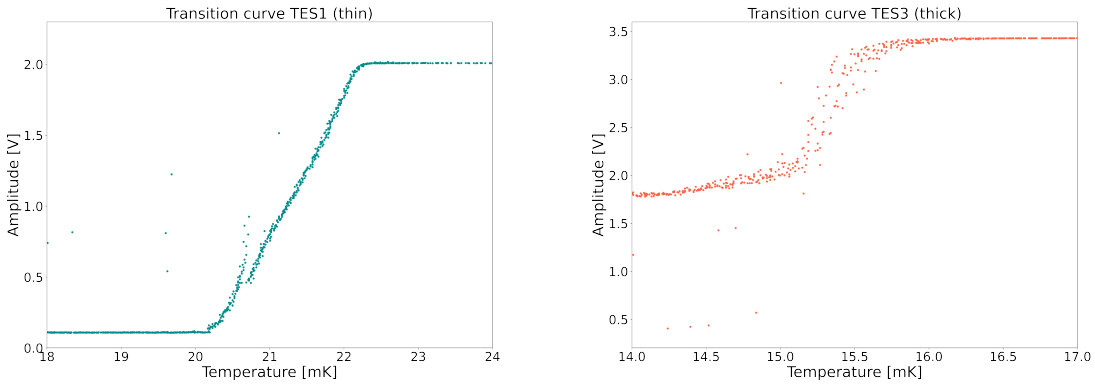

Figure 5.11: *Left:* Transition curve of TES-SLthin1. *Right:* Transition curve of TES-SLthick3.

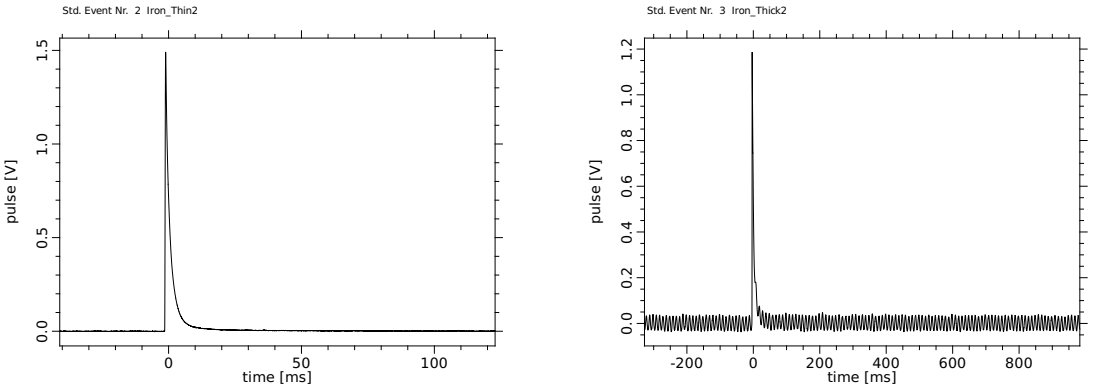

Figure 5.12: Template pulses obtained by averaging the 5.89 keV pulses of the ^{55}Fe source. *Left:* Template pulse of TES-SLthin1. *Right:* Template pulse of TES-SLthick3.

with the smallest phonon collectors is named TESA, the one with standard phonon collectors is named TESB, the one with the largest phonon collectors TESD and the last one TESC (refer to Figure 5.13 (*left*)).
Four sensors using this mask have been fabricated onto a $10\times20\times5\,\mathrm{mm}^3$ Al_2O_3 crystal and they were tested in Cryo2. A final setup with the wire bonded electrical connections made on a copper holder is shown in Figure 5.13 (*right*).

During the cooldown, the connection to TESC was lost, therefore it was not possible to measure this sensor. Furthermore the mixing chamber heater was open. Thus, it was not possible to sweep up and down the mixing chamber temperature and to measure

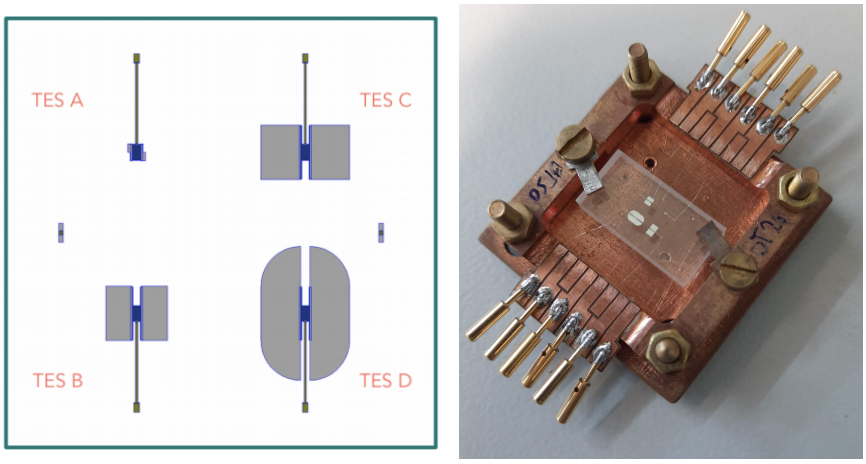

Figure 5.13: *Left:* Schematic drawing of the design of the four TES design compared in this test. *Right:* Picture of the tested sample.

the trasitions reliably.
Therefore, this analysis does not follow the standard procedure, but utilises different aspects of the TES performance to compare the sensors, which had previously proven to be good figures of merit of the overall sensors' performance. In particular, we compare two aspect of the TES performance: the energy resolution and the ratio of athermal to thermal component in the signal.

Results To evaluate the ratio between the athermal and the thermal component of the pulse, we perform parametric fits of the template pulses, using the model developed in [93] and described by the central equation in Figure 5.1. The results of the fits are shown in Figure 5.14. From the fit we obtain that the ratio of amplitude of the athermal and the thermal signal a_N/a_T is (96.7± 0.6)% in TESA, (96.8±0.5)% in TESC, and (97.5±0.4)% in TESD. Looking at the energy spectra in Figure 5.15, we can observe that the energy resolutions of TESB and TESD are clearly better than the resolution of TESA. For quantifying this observation, we perform Gaussian fits of the peaks.
The energy resolutions at 5.89 keV obtained are:

- TESA: $\sigma_{TESA} = \sim 213\,\text{eV}$
- TESB: $\sigma_{TESB} = \sim 99\,\text{eV}$
- TESD: $\sigma_{TESD} = \sim 95\,\text{eV}$

These results hint towards an improvement in the energy resolution going from a geometry with very small phonon collectors to the standard geometry. Further increasing the dimensions of the phonon collectors does not appear to have a significant impact

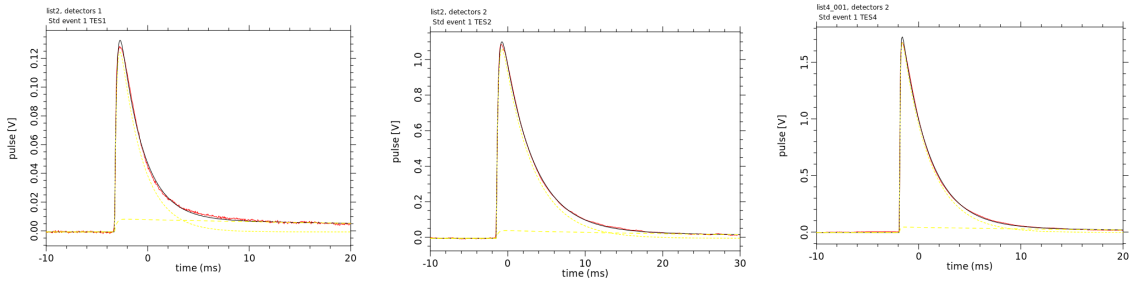

Figure 5.14: Fits of the template pulses obtained by averaging the pulses caused by energy deposits in the abosrber crystal by a 5.89 keV emitted by the ^{55}Fe source. *Left:* Parametric fit of the template pulse of TESA. *Centre:* Parametric fit of the template pulse of TESB. *Right:* Parametric fit of the template pulse of TESD.

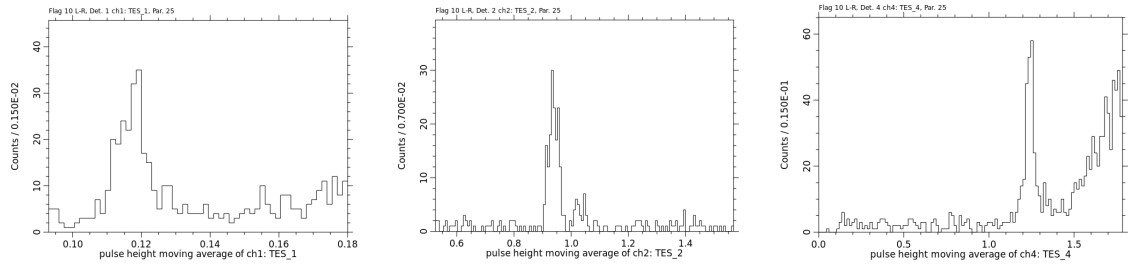

Figure 5.15: Energy spectra around the 5.89 keV peak of the x-ray from the ^{55}Fe source. *Left:* Spectrum of TESA. *Centre:* Spectrum of TESB. *Right:* Spectrum of TESD.

on the resolution. Indeed, the performance of TESB and TESD are compatible.

In light of the results obtained, we conclude that the current dimensions of phonon collectors appear to be ideal.

5.4.3 Magnetic Shield on Phonon Collectors

When superconductivitity was first discovered in 1911 [112], superconductors below their transition temperatures were thought to be simple ideal conductors, i.e. a metallic material with zero resistance. In 1933, Meißner and Ochsenfeld performed an experiment showing that, in addition to having zero resistance, superconductors exhibit another very interesting phenomenon: the magnetic flux density inside the material drops to zero [113]. This phenomenon was later named Meißner effect. Further studies of the magnetic properties of such materials [114] revealed that superconductors expell magnetic fields from their interior, creating surface currents to compensate for exter-

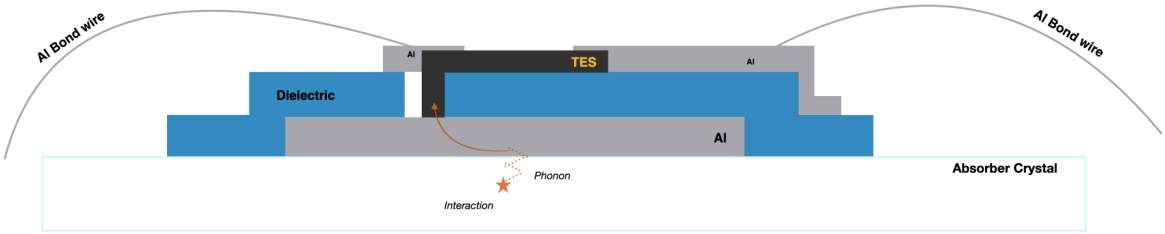

Figure 5.16: Schematic representation of the proposed new sensor design, with an Al layer below the W-TES, acting as a phonon collector and shielding the sensor from magnetic field variations simoultaneously.

nally applied fields.

Since the TES is a tungsten thin film, operated in its transition between its normal and superconducting phase, it is sensitive to external magnetic field variations during operation. The extent of this influence in the CRESST setup was studied in [108], and an active compensation system for the magnetic field variation on-site has been developed for the CRESST experiment. The active compensation is made using a system of coils in coordination with magnetic flux gates placed around the experimental setup that measures magnetic field in all three directions. The current flowing in the coils in tuned to compensate for external variations of magnetic field.
This approach is currently in use in the CRESST facility, nevertheless it is not the optimal solution, as different sensors react differently to variations of the magnetic field. In light of this, a shielding directly at the TES location was proposed.

A new sensor design

The basic idea is to add a superconducting Al layer to the present sensor design, to act as a shield, compensating for magnetic field variations directly at the location of the TES. Aluminium is the ideal choice for this purpose, as it becomes superconductive below 1.2 K, and therefore at our operating temperature it is well below its transition. In addition, this material has been subject to extensive studies in the CRESST collaboration, thus its properties and deposition techniques are very well known.

The proximity effect is a well-known phenomenon observed in superconductors when they come into contact with normal metals or other superconductors [111]. It involves the infiltration of superconducting properties into the neighboring material, typically over a short distance comparable to the coherence length of the superconductor. This effects creates a bilayer material, having intermediate superconducting properties com-

pared to the two materials involved. Depending on the thickness of the two layers involved, the properties can differ. As a consequence, in this novel design it is necessary to insulate the aluminum layer from the tungsten layer. If the two materials come into contact, proximity effects could arise, potentially increasing the tungsten transition temperature. In CRESST sensors, the tungsten layer is thinner than the aluminum layer, suggesting that the bilayer aluminum-tungsten structure might exhibit a transition temperature closer to that of aluminum (1.2 K) than tungsten (∼15 mK). However, the most critical concern regarding insufficient insulation between the layers is the risk of short-circuiting the TES. Any current would preferentially flow through the superconductor due to its lack of resistance. Short-circuiting the TES would render it inoperable, since the bias current would preferentially pass through the aluminum layer rather than the tungsten layer. Hence, stringent insulation measures are essential to avoid such issues.

In light of this, a dielectric layer is deposited in between the Al and the W in this design (see Figure 5.16). To allow the Al layer to act as a phonon collector, transmitting the collected signal to the thermometer, this design includes a mechanical connection between the Al and the W-TES.
To the best of our knowledge, such an approach has never been tried. Therefore, it is essential to confirm its feasibility and evaluate the influence of this innovative design on the signal-to-noise ratio of our TES.

Tests and Results

The first challenge to face for the production of such a new sensor design constists of the choice of the dielectric layer. In this work, we decided to use a sputtered layer of silicon dioxide (SiO_2) for insulation.

In the first experimental test, we produced two different samples with the design schematised in Figure 5.16: one with a 50 nm thick SiO_2 layer and one with a 100 nm thick SiO_2 layer. The Al for this samples was produced in the same evaporation process, while the W was deposited in distinct runs.
Both of these samples showed a transition around 1 K, hinting towards a proximisation of the W due to the Al layer, which resulted in a transition temperature compatible with the Al one. Considering the significant coherence length of aluminum, which extends to 1600 nm, it is reasonable to anticipate the occurrence of the proximity effect on tungsten.

In the second test, we increased the SiO_2 thickness, producing four samples with 800 nm thick SiO_2. Two of these four samples presented a 1 μm thick Al layer, while the other two had a 1.5 μm layer (see Figure 5.17). Even with the thicker SiO_2 layer, these samples exhibited a superconducting transition at approximately 1 K. Considering the

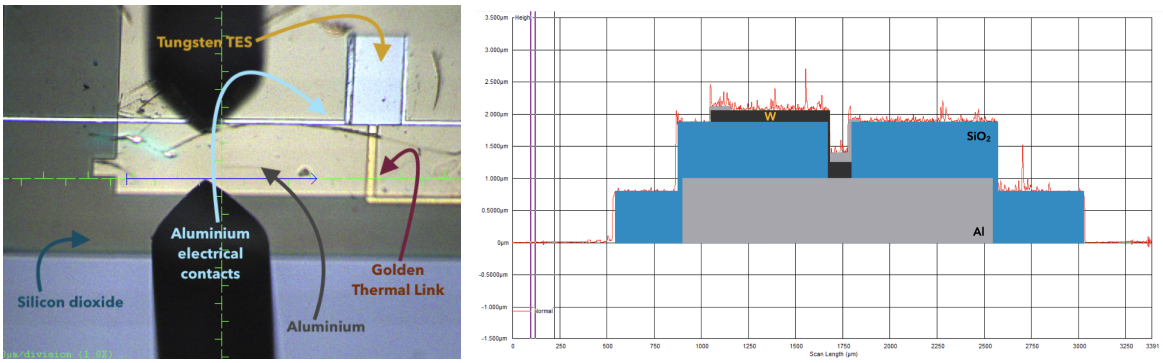

Figure 5.17: *Left:* Picture of the sample produced in this second production, taken with a microscope. The different materials are shown. *Right:* Profile of this sample measured with an alpha stepper. The different materials are shown with their respective thicknesses.

substantial thickness of the dielectric layer, the proximity effect alone does not appear to be a plausible explanation for such a high transition temperature and motivated us to carry out some studies of the chosen dielectric material.

To test the effectiveness of the SiO_2 insulation layer, we produced two new samples, with no mechanical connection between the W-TES and the Al underneath. Therefore they were samples with an Al layer, covered by a 800 nm thick SiO_2 layer, on top of which a W-TES was structured. A picture of these samples is shown in Figure 5.18 (*left*).
These samples showed a transition to their superconducting phase around 350 mK, as reported in Figure 5.18 (*right*).
This measurement indicates that the priximity effect persists, even if with a diminished magnitude, therefore pointing towards an ineffectiveness of the chosen dielectric material as an insulation layer for this type of design. Thus, we decided to investigate the possibility of using a different dielectric material, in particular we chose the KMSF® 1000 low-stress dielectric photoresist.

A detailed description of this study can be found in [115], where the possibility of shielding the W-TES from magnetic field variations is investigated. In [115] it is shown that an Al layer can be employed as an effective shield against variations in the magnetic field at the location of the TES. The next step for producing sensors with the novel design illustrated in Figure 5.16 will consist of trying to have the Al layer underneath the W-TES, working as a phonon collector. The first step in this study will be trying to understand if it is possible to produce good quality W thin films on top of the KMSF® dielectric photoresist.

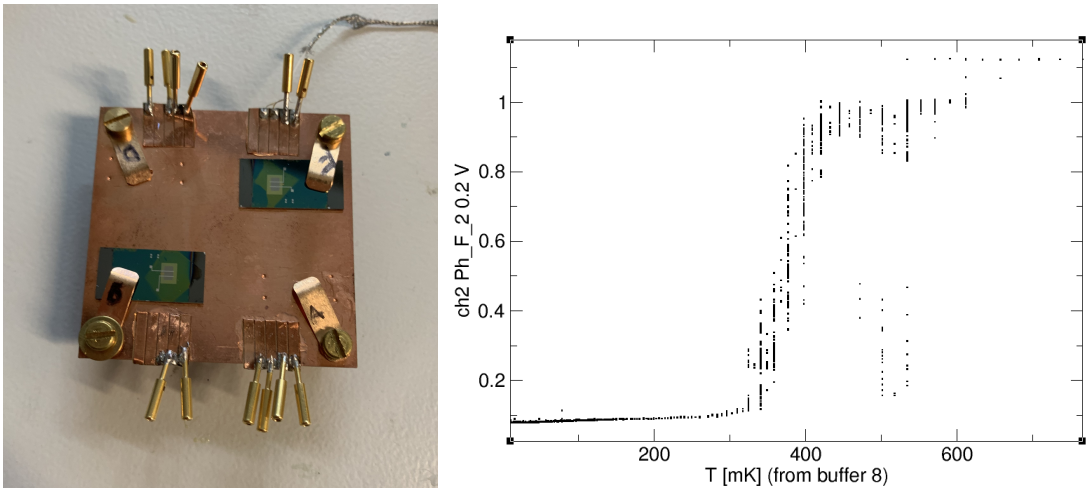

Figure 5.18: *Left:* Picture of the two samples produced to test the effectiveness of the SiO_2 insulation layer. *Right:* Transition curve of one of the two samples tested to verify the effectiveness of the insulation layer.

5.5 Conclusions

In this chapter, numerous studies performed with the objective of improving the sensitivity of the CRESST transition edge sensors are presented, targeting specific aspects of the TES design.
The thickness, composition and dimensions of the phonon collectors were addressed in different tests. Thanks to the results obtained, it was possible to improve the sensitivity of our TES on Al_2O_3 substrates.
A new sensor design was proposed to replace the use of an external magnetic shielding with coils and flux gates which is suboptimal at present. In [115], a prototype sensor was made that demonstrated the magnetic shielding aspects of it. Several tests were attempted using sputtered SiO_2 as insulation layer, which were found to be very non-trivial. A new material, the KMSF® 1000 low-stress dielectric photoresist, could be promising in this regard and needs to be tested as the next steps.

Overall, it is shown that it is possible to achieve an improvement on the sensitivity on the present sensor design. Furthermore, an in-situ passive magnetic shielding would further improve the data quality of the present sensor.

Chapter 6

Sputtering the W-TES

Within the CRESST experiment, the W-TES are currently produced via an electron-beam evaporation system. This technique is extremely reliable, but every production run requires a considerable amount of time.
With the upcoming upgrade of the CRESST experiment, which will entail a significant increase in the number of readout channels up to 288, there is a pressing need for a novel and rapid production method.
Magnetron sputtering has been identified as a viable option for W-TES production [116]. This chapter delves into the challenges and advantages associated with this approach, utilising previously obtained results as a starting point for further investigation.
A new sputter machine dedicated to the tungsten deposition has been established at the Max Planck Institute for Physics. This chapter outlines the commissioning process of this machine and presents the results obtained from various tests. The concluding section discusses the future plans for this project.

6.1 Motivation

The need for a rapid and reliable production of W-TES comes from the need for the CRESST experiment to expand its physics reach, collecting a significant amount of exposure, while lowering the detectors' threshold.
A comprehensive understanding of two key elements is essential: firstly, the importance and planned execution of the CRESST upgrade, and secondly, the current process of detector production. Both of these aspects will be detailed in the following.

6.1.1 The CRESST Upgrade

The physics program of the CRESST experiment entails an upgrade enabling the experiment to explore the low-mass dark matter region down to the neutrino floor (see

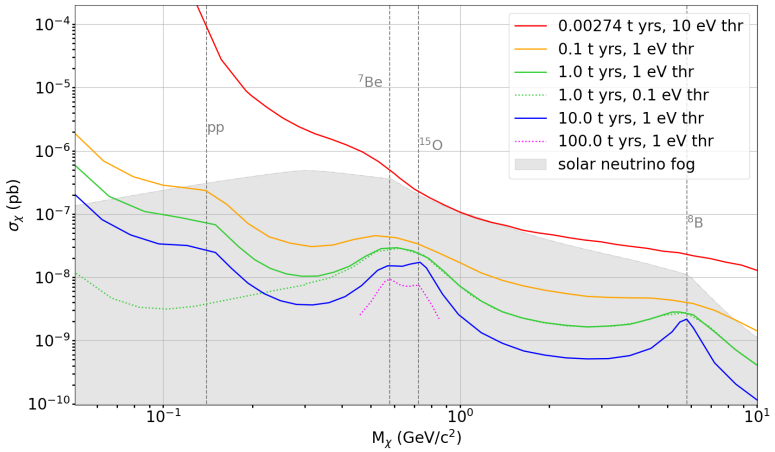

Figure 6.1: 3σ discovery potential for dark matter in different experimental settings in $CaWO_4$ detectors. The red line correponds to the targeted exposure of 1 tonne day in the CRESST upgrade with a threshold of 10 eV, in the very optimistic assumption of zero background. Image taken from [118]

Figure 6.1).
For this objective to be achievable, several conditions must be met, including an increase of the exposure and the reduction of the threshold to $\mathcal{O}(10\,\text{eV})$ for each detector module [117]. Detectors production represents the main challenge to face for realising the upgrade. Consistently achieving such low thresholds is a challenging task, and the increased exposure necessitates the production of an unprecedented number of detector modules with reproducible response. Specifically, as mentioned earlier, the number of readout channels is set to increase to 288. From the detectors perspective, this expansion translates to a rise from $\mathcal{O}(10)$ detector modules to $\mathcal{O}(100)$ detector modules, to be produced.
With this increase, CRESST aims to collect an exposure of around 1000 kg/days within two years of data taking. The sensitivity projections for this upgrade are depicted in Figure 6.1, in the very optimistic assumption of zero background. These projections do not take into account the low-energy excess background (see section 7.1). If this background is not comprehended and mitigated, it could profoundly alter the outcome.

6.1.2 TES Evaporation

Depositing tungsten thin films presents a significant challenge, and achieving transition temperatures within the range of interest for the CRESST experiment ($\sim$15 mK)

is non-trivial.
The deposition of such a film was firstly reported by the Max Planck Institute CRESST group [119] in the early 1990s. The group reported the deposition of W thin film with a critical temperature (T_C) of ∼15 mK, closely matching that of bulk tungsten [120] (more details about W superconductivity can be found in section 6.2).
At that time, the W deposition process was extremely long and complex. High purity epitaxial tungsten films were produced in an electron-beam evaporation system, in an ultra high vacuum chamber, at a base pressure of 6×10^{-12} mbar. Achieving such low pressure levels demanded considerable effort. The reduction of background impurities involved pumping the system for approximately two days, while the hydrogen partial pressure was suppressed using a titanium sublimation pump. Additionally, the system underwent a bake-out process at 220° C to accelerate the outgassing of molecules absorbed in the chamber walls. Finally, the chamber was enveloped by nitrogen-cooled shields to prevent overheating via radiation, particularly through the electron-beam heating of the tungsten source. Furthermore, the deposition process necessitated heating the substrate to approximately ∼600° C to regulate the microstructure of the film. In summary, during the 1990s, each tungsten deposition process demanded approximately a week of work.
Over time, this process has been streamlined and adjusted to the experimental needs. For instance, the required pumping time has been condensed to overnight, and baking out the system is no longer practiced. These procedures aimed at reaching the lowest chamber contamination possible, with the objective of depositing a mono-crystalline W film. Over time, we observed that we do not need to produce mono-crystalline thin films to have the desired superconducting properties. These adjustments have enabled the tungsten deposition process to be completed within a time span of two days. However, the machine itself has remained unchanged (and it is shown in Figure 6.2), and imposes constraints on the number of detectors that can be produced in a single process. Only a disk area of approximately ∼30 mm in diameter can be effectively deposited.
Moreover, the evaporation process exhibits a success rate of approximately 75%, implying that only about three tungsten films out of four display a measurable superconducting transition. Consequently, all produced sensors need to be classified at millikelvin temperatures to measure their T_C and transition shape. This additional step further contributes to the time consumption of the production process.

In light of the complexity and duration of the tungsten electron-beam evaporation process, coupled with the requirement to manufacture a substantial number of reliable and sensitive detectors for the forthcoming CRESST upgrade, the necessity for a novel and expedited fabrication method for tungsten films becomes imperative.

Figure 6.2: A picture of the tungsten evaporation system at the Max Planck Institute for Physics in Munich. The ultra high vacuum chamber is shown, covered with the heating blankets, which were used for the system bake out in the past.

6.2 Tungsten Superconductivitity

Tungsten, identified as an element in 1781 for the first time, is a rare metal primarily found on Earth in compounds with other elements.
Tungsten exists in two crystalline forms: the α and the β phases. Although the β phase is metastable, it can coexist with the α phase under ambient conditions, thanks to stabilisation by impurities or non-equilibrium synthesis. In contrast, the α phase is the stable form.
Superconductivity in tungsten was firstly observed by Gibson and Hein [121] in 1964. They measured a superconducting transition at around 11 mK. Several measurements followed, determining a transition temperature between 11 and 16 mK and a critical field at 0K in the range 115.0-123.7 μT [121–124]. Nowadays, bulk tungsten in its α phase is recognised to exhibit a superconducting transition at approximately 15.4 mK [120], whereas the transition temperature of tungsten in its β phase is observed to vary within the range of 1.0-4.0 K [125, 126].

For the production of W-TES, our objective is to produce thin films of tungsten in its α phase, as this ensures transition temperatures within our range of interest. Nevertheless, thin film superconductivity differs from bulk superconductivity, as thin films

demonstrate distinct superconducting properties, influenced by production parameters and films characteristics.

The crystalline phase of the deposited film plays a pivotal role in determining the film's transition temperature. Moreover, within the crystal lattice, the arrangement of atoms profoundly impacts the electronic band structure, which subsequently influences the superconducting behavior.

The thickness of a thin film also significantly influences its superconducting behavior. Variations in film thickness have the potential to impact the films' microstructure, stress state, and resistivity. Typically, a superconductor is classified as a bulk material when its thickness approaches or surpasses several times its coherence length. The coherence length (ϵ_0) of a pure superconductor with critical temperature T_C serves as a measure of its Cooper pair size and it can be calculated at T=0 K using the formula [127]:

$$\epsilon_0 = 0.18 \cdot \frac{\hbar v_f}{k_B T_C} \tag{6.1}$$

Here, v_f represents the Fermi velocity, $\hbar$ is the reduced Planck constant and k_B is the Boltzmann constant. By applying this formula, we compute a coherence length of 32 μm for tungsten, given its superconducting transition occurring at 15.4 mK [123]. Given this information, it is evident that the CRESST W-TES, with a thickness of 180-200 nm, fall within the category of thin films.

Scatterings on grain boundaries or on surfaces (especially rough surfaces) can drastically reduce the electrons mean free path, strongly affecting the films' superconducting properties [121]. Reactions with residual materials during the deposition process can create superconducting compounds with critical temperatures up to a few K [128,129], while the presence of ferromagnetic impurities may lower the T_C of these films or entirely suppress their superconductivity [130]. Consequently, surface polishing and cleanliness should be carefully controlled.

As detailed in section 5.4.3, external magnetic fields can significantly affect the superconductivity of thin films, particularly of W-TES. This is primarily due to tungsten's notably low critical magnetic field [123].

A crucial aspect of thin film superconductivity involves film stress, which has been extensively studied for various materials [131–133]. Stress is measured as force per unit area $\sigma = F/A$, analogous to pressure.
Typically, when a film undergoes linear deformation, it experiences strain, defined as $\epsilon = \Delta L/L_0$, where L_0 denotes the initial length of the film and ΔL represents its

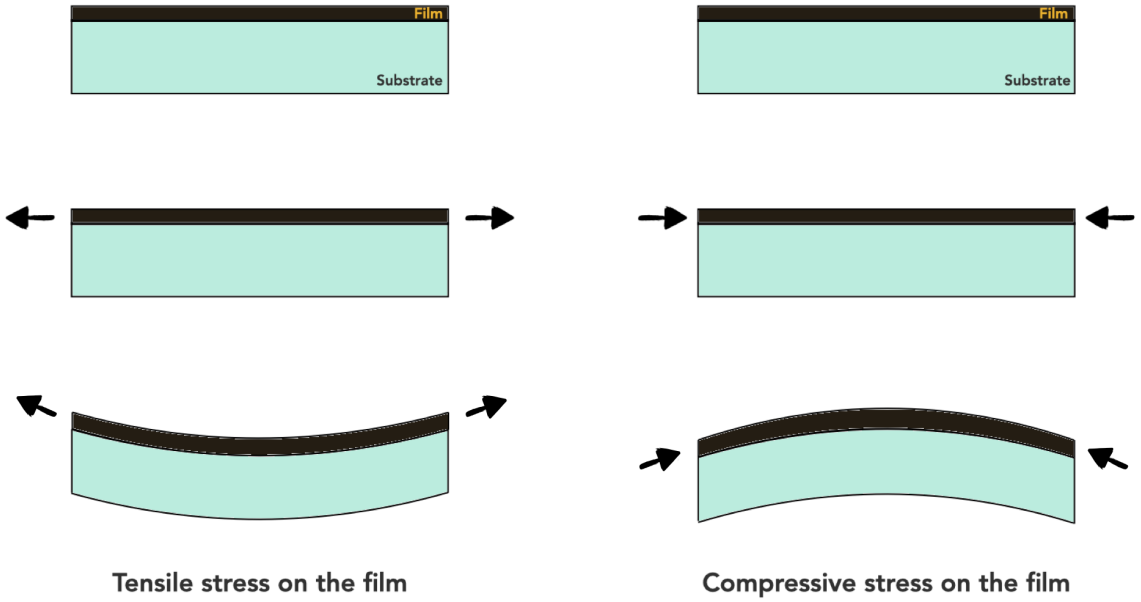

Figure 6.3: Schematic representation of tensile and compressive stress exerted on a thin film. The arrows provide a schematic representation of the direction of the force experienced by the films.

variation. Strain (ϵ) is related to stress (σ) via the modulus of elasticity (E):

$$\sigma = E \times \epsilon \tag{6.2}$$

Tungsten has one of the highest modulus of elasticity, $E_W = 411\,\text{GPa}$, thus large stress values can lead to only slight deformations. For instance, 1 GPa of stress will lead to an elongation of $\sim$0.002% only, which may seem minimal and barely measurable. However, even such slight deformations can entirely suppress tungsten superconductivity.

Two main types of stress can be present in thin films: tensile stress and compressive stress. The former tends to increase the films' transition temperature, while the latter typically shifts it to lower values. Residual stress of these types can easily be stored in sputtered thin films due to energetic gas ions and atoms impinging on the surface during the deposition process. The type of residual stress in the films depends on the kinetic energy of the atoms impinging on the surface. Atoms reaching the surface with excessive energy (e.g. when the sputtering pressure is low, and the sputtered atoms have much higher energies than the plasma gas) have a high surface mobility in the substrate, thus they can create tensile stress [134]. Conversely, atoms reaching the substrate with insufficient energy (e.g. when the sputtering pressure is high, the sputtered

atoms undergo a large number of collisions, and thus are thermalised by the plasma gas) have limited surface mobility and can result in films exhibiting compressive stress [134].

It is also crucial to consider the thermal expansion coefficients of both the substrate and the films, particularly when exposing them to temperatures significantly different from the deposition temperature.
In the context of CRESST, where W-TES are operated at millikelvin temperatures, stress is expected to develop during measurements. Specifically, if the substrate material has a thermal expansion coefficient smaller than that of tungsten, the film's thermal expansion will be restrained by the substrate, and tensile stress will arise. Conversely, compressive stress will occur when the thermal expansion coefficient of the substrate is larger than that of tungsten. Indeed, the film will be forced to expand by the substrate material and it will be subject to its own inertial force.

6.3 W-TES Production via Magnetron Sputtering

Magnetron sputtering is a commonly utilised deposition technique, which typically provides a high production rate, together with a good film quality. A magnetron sputtering facility consists of a vacuum chamber, equipped with a number of magnetron sputtering cathodes. During operation, the chamber is filled with a noble gas, typically argon (Ar) or xenon (Xe).
The possibility of utilising such a technique for W-TES production in CRESST is not a novelty [116, 135, 136]. The production of sputtered thin films with the desired quality proved to be a non-trivial task, as many parameters need to be carefully optimised, to tune the thin films characteristic. At first, RF-sputtering was investigated in former works, such as [135, 136]. Despite the efforts, only a few non-reproducible superconducting thin films were obtained, and obtaining reliable superconducting characteristics proved to be a non-trivial task.
Later studies focused on DC-sputtering [116]. Employing this technique, stable results could be obtained and tuning the thin films superconducting properties started to seem feasable. This lead to the acquisition, by the Max Planck Institute for Physics in Munich, of a new sputtering machine, dedicated to tungsten sputtering and designed according to the knowledge aquired in [116].
In the following, the details of the magnetron sputtering deposition process are presented. Afterwards, results obtained in [116] are briefly summarised, to provide a starting point for new investigations. Finally, the new sputtering facility is introduced. The commissioning of the machine is presented, followed by studies concerning the possibility of tuning the W-TES characteristics via sputtering parameters.

6.3.1 The DC Magnetron Sputtering Process

Sputtering utilises a glow discharge plasma that is confined by a magnetic field and directed towards a target material through an electric field. Typically, the plasma consists of a noble gas such as argon or xenon to prevent unwanted reactions with the target material. The gas is introduced into the vacuum chamber with controlled flow, enabling precise regulation of the chamber pressure during deposition.
In the magnetrons, the magnetic field is generated by permanent magnets located on the backside of the target material. These magnets produce a localised magnetic field, which focuses the plasma into a narrow ring on the target surface, while enhancing the sputtering rate. Additionally, a dedicated chiller is employed to prevent target overheating.
The electric field is established by a power supply, which generates a DC current flow between the anode (typically the substrate, grounded) and the target material (cathode). This electric field sustains the plasma glow discharge.
As a result, energetic ions from the noble gas are accelerated towards the target, causing material atoms to be ejected from the target surface. These atoms then drift towards the substrate, where they condense and accumulate, forming the thin film.
A schematic representation of the sputtering process is presented in Figure 6.4.

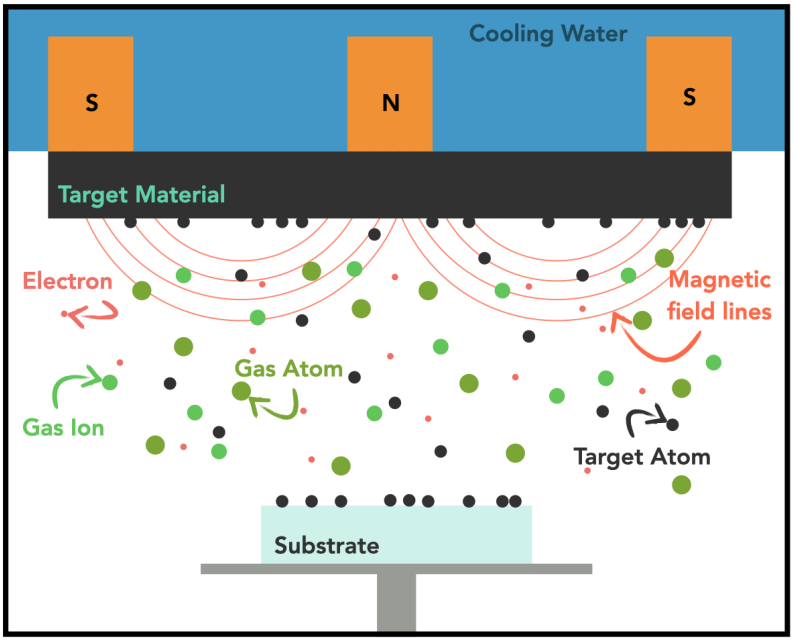

Figure 6.4: Schematic representation of the DC magnetron sputtering process.

6.3.2 Previous Results

The work done in [116] provides a first successful realisation of novel W-TES production process. W-TES were successfully produced in two different sputtering systems. The results from the first system provided the proof-of-principle concerning the possibility to deposit superconducting W thin films. The sputtering gas was changed from Ar to Xe, as the introduction of this second gas allowed for fine-tuning the T_C, allowing to control the residual stress in the film. The second sputtering system (Sputter Machine 533) was commissioned during the time of that work at the Max Planck Institute for Physics in Munich and it was optimised to produce superconducting W films. The introduction of a thin $\mathcal{O}(1\,\text{nm})$ copper (Cu) layer below the tungsten allowed for the production of superconducting films on multiple substrates, namely SiO_2/Si, pure Si, $CaWO_4$, Al_2O_3.
Furthermore, in [116], the effect of various sputtering parameters on the superconducting characteristics of thin films has been studied in detail, resulting in the tunability of the transition temperature of thin films through many of those. In addition, an innovative method for predicting the T_C of thin films, without cooling them down to millikelvin temperatures has been established. This method consists in measuring the residual resistance ratio (RRR) of the films. The RRR is measured as the ratio between the resistance of the film at room temperature and its resistance at 4 K. The cooldowns to 4 K were performed quickly, using a dip stick inserted in a liquid helium can.
Figure 6.5 shows the main dependencies found in [116]. A linear relation between RRR and T_C was found, together with a strong dependency of the RRR value on the sputtering pressure.

6.4 Sputter Machine 581

A new sputtering machine, named Sputter Machine 581, manufactured by Prevac and specifically designed for tungsten deposition, has been delivered to the Max Planck Institute for Physics in March 2022. A picture of this machine can be found in Figure 6.6.
The primary component of a sputter machine is the main vacuum chamber, where the sputtering processes happens in vacuum. The main vacuum chamber of Sputter Machine 581 contains four different stations, each dedicated to a specific process. Three of these stations are equipped with 3-inches magnetrons, while the fourth station is dedicated to sample cleaning. Both, an RF and an ion source cleaning are available. For the purpose of this project, RF cleaning is used, due to its less aggressive nature compared to ion source cleaning, which may affect less the substrates' surfaces and has a low probability of damaging them. RF cleaning removes impurities and contaminants from surfaces via a plasma of low energetic Ar ions.
The system features a 3-axis manipulator, enabling the substrate to be positioned

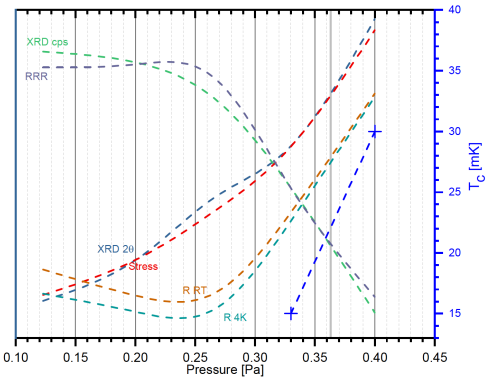

(a) Parameters' dependence on Xe pressure. That data set covers the transition from compressive(left side) to tensile stress(rightside indicated on the figure with the vertical gray line. A correlation of T_C with stress, resistance and RRR can be seen,which confirms the results from IPP.

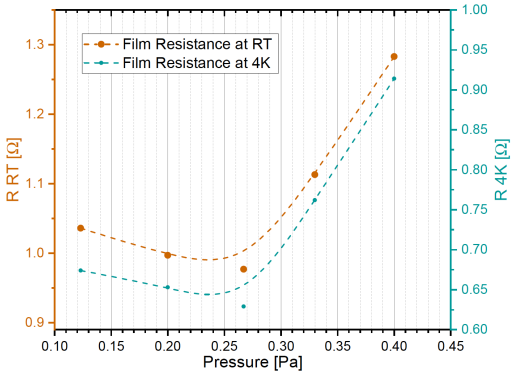

(b) The effect of Xe pressure on film resistance.

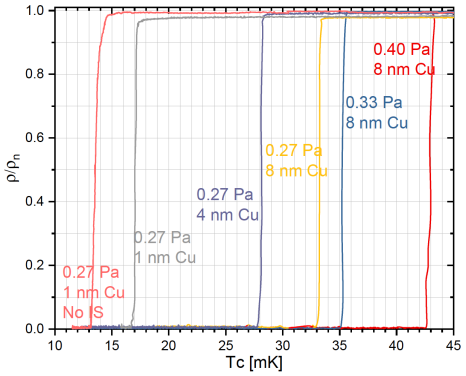

(c) An illustration of the possibility to produce tungsten films with tunable T_C on sapphire. The transition curves are normalized for clarity. Tuning the T_C on sapphire substrates can be done by changing the Xe pressure, the copper thickness, and the use of ion source cleaning (IS).

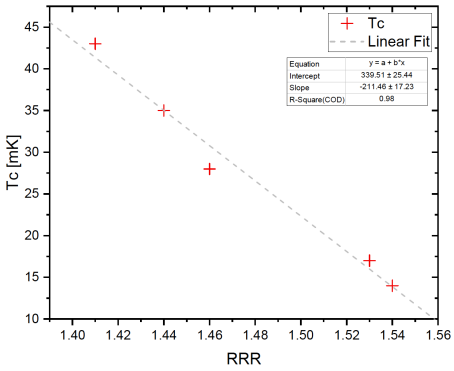

(d) T_C vs RRR for tungsten films sputtered onto sapphire substrates(same of the previous figure).The dashed gray line is a linearfit. The T_C here corresponds to the temperature at which the resistance of the film drops to the half value of the normal resistance.

Figure 6.5: Summary of the reuslts obtained in [116] concerning the tunability of the transition temperature of W thin films through sputtering parameters. Images and captions taken from [116].

beneath the selected target within the chamber. Additionally, it allows for substrate rotation and wiggling during deposition, facilitating a more uniform deposition process. To further enhance uniformity without decreasing the deposition rate, each magnetron is equipped with a rotator, enabling magnetron tilting and thus allowing for confocal deposition (i.e. deposition with the cathode positioned at an angle relative to the vertical axis). Additionally, the machine is equipped with a load-lock, facilitating rapid sample transfers into the process chamber without the need for venting the entire system. The load-lock features a sample holder capable of accommodating up to four substrates simultaneously. The ability to vent only the load-lock for substrate insertion,

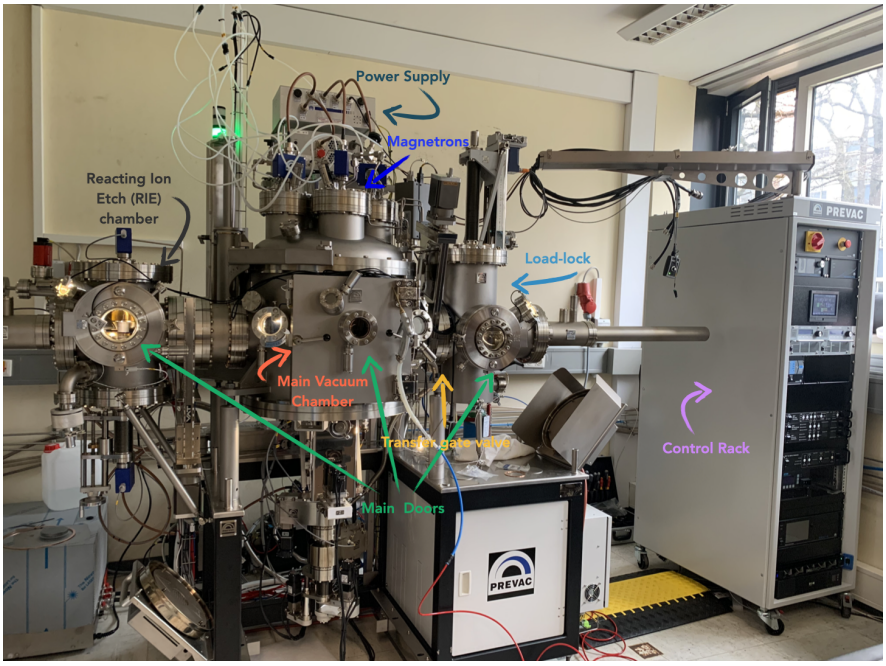

Figure 6.6: Picture of the new sputtering machine dedicated to W production at the Max Planck Institute for Physics.

without requiring venting of the main chamber, significantly expedites the process. A gate valve separates the load-lock from the main chamber, allowing for sample transfer when opened.
A gate valve positioned in front of the turbo pump of the main hamber allows for a reduction of the pumping speed during deposition. Indeed, the ability to precisely control the chamber pressure during deposition has proven to be essential [116].

6.4.1 Commissioning

After the initial setup and testing of the machine, our first objective was to ensure the stability of the sputtering process and its outcomes. Tungsten sputtering is notably affected by the conditions within the main chamber during deposition, as well as by the geometry and conditions of the target. Furthermore, the measured pressure within the chamber during the process is greatly influenced by the positioning of the pressure reader, the pumps, and the gas inlet. Since the position parameters may be significantly different from those of the machine previously in use, new studies for all parameters are necessary.
The first focus of this work was to identify sputtering parameters that would enable the production of samples with reproducible superconducting properties.
To enable such studies, it is important to define a precise experimental procedure, comprising sample preparation, RF cleaning, Cu deposition and the final testing, to ensure comparability among different samples.

6.4.2 Experimental Procedure

In the initial phase of this project, we exclusively utilise silicon samples to establish an initial working production flow. This approach allows us to lay the fundations for establishing well defined procedures for producing superconducting W thin films on other crystals as well.
The sample production comprises various steps, detailed in the following.

Substrate Preparation The Si substrates employed in this work were prepared by the HLL semiconductor laboratory (Halbleiterlabor der Max Planck Gesellschaft), in Garching, from high resistivity p-type silicon wafers $\sim 0.35\,\mathrm{mm}$ thick. The wafers were then cut into $20\times10\,\mathrm{mm}^2$ substrate with a laser cutting machine.
Before being inserted into the sputter machine, the substrates underwent cleaning procedures in the MPP cleanroom.

RF cleaning The samples were then mounted onto the sample holder of the load-lock of the sputter machine. The chamber was then pumped down to a pressure $< 10^{-6}\,\mathrm{mbar}$, to allow for a safe opening of the gate valve and avoid the insertion of impurities into the main chamber. The required base pressure of the main chamber before initiating the sputtering process is set to $\mathcal{O}(10^{-8}\,\mathrm{mbar})$.
Once the sample is transferred into the main chamber, it undergoes RF cleaning. During this procedure, the gas flow in the chamber has to be adjusted such that the pressure in the chamber is $\mathcal{O}(10^{-2}\,\mathrm{mbar})$. We clean the samples for 10 minutes, with 50 W of RF power.

Cu Sputtering Afterwards, following the results in [116], we produce a very thin ($\mathcal{O}$(nm)) copper under-layer, to facilitate the growth of W thin films independently of the employed substrate. During this deposition, the pressure is kept at $3.15{\cdot}10^{-2}$ mbar, through a flow of Ar of 15 sccm. Before initiating the process, the Cu target is sputtered clean for 5 minutes at 100 W DC, avoiding any contamination of the substrate. Then, Cu is sputtered for 60 s at 100 W DC. During Cu deposition, the substrate rotates around the vertical axis, to enhance uniformity. The Cu target used has a purity of 99.999%.

W Sputtering Finally, the tungsten layer has to be produced. Many diverse sputtering parameters have been tested, with the purpose of obtaining a reliable production method resulting in W thin films with reproducible superconducting properties. Nevertheless, the general procedure was standardised, to ensure the maximal reproducibility. Firstly, we pump the main chamber down. Ensuring a good enough base pressure at this stage is very important, as it ensures that no residuals of Ar or Cu atoms will contaminate the W deposition process. Indeed, the gas utilised for this process is xenon. Xe is chosen because its atoms are much less probable to be trapped inside the thin films than Ar atoms [137]. To make the pressure of Xe in the main chamber stable, following previous experience [116], a one litre gas bottle is placed between the Xe bottle and the mass flow controller.
Before proceeding with the DC W sputtering, the target has always been sputtered clean for 10 minutes, avoiding substrate contaminations. After cleaning the target, the deposition process was performed.

Testing Afterwards, the RRR values of the prepared samples were measured. Firstly, we tried to reproduce previous results, targeting RRR values in the range 1.4-1.45 (which proved to show T_C in the range of 15-25 mK [116]).
Measuring the T_C of the samples to control the validity of the relation between T_C and RRR was the natural following step. To do so, we mounted the substrates on a copper holder (see Figure 6.7), and strongly coupled them to the heat bath. The tests were performed in one of the dilution refrigerators at the above-ground facility of the MPP. The transition temperature and shapes were measured seewping up and down the mixing chamber temperature with a dedicated heater, using the same procedure described in section 5.3.

6.4.3 Characterisation and Results

During this project, we sputtered more than 70 substrate and we cooled down more than 25 of them to mK temperatures.
In the initial phase of the project, we adjusted the parameters to achieve RRR values within the previously accepted range. Utilising a DC power of 450 W and maintaining

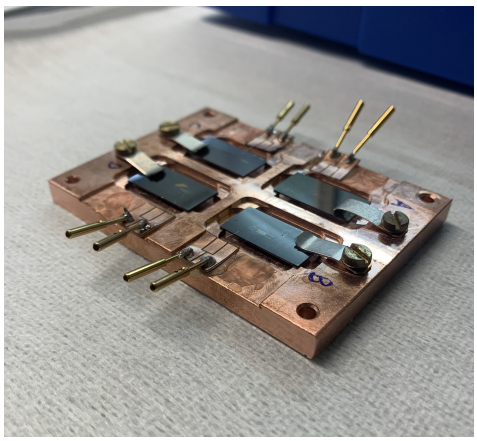

Figure 6.7: Picture of the samples holder used for the T_C tests of sputtered W films. The holder is designed to contain four $10 \times 20\,mm^2$ substrates, each resting on four Cu corners and held in position by a bronze clamp.

a pressure of approximately 10^{-2} mbar, we consistently obtained RRR values falling between 1.25 and 1.35. The majority of these samples exhibited superconducting transitions, with temperatures ranging from 15 mK to 35 mK. With the aim of replicating previous findings, we analysed the dependencies of the transition temperatures obtained as a function of various parameters. This study's objective is to investigate the potential to adjust the T_C of the tungsten thin films through sputtering parameters using the new machine.

In the first part of this work, we focus on silicon as a substrate material. The plots in Figure 6.8 illustrate the trends of the T_C of the samples as a function of the pressure during the deposition and of the voltage applied. However, these plots do not exhibit a clear trend, prompting further investigation into the relationship between T_C and RRR values for these samples. Figure 6.9 indicates that the trend observed in [116] is not validated by our tests. The plots in Figure 6.8 do not show an obvious dependency of the T_C from these parameters, the RRR and the T_C of our samples appear to be uncorrelated. However, we could utilise the RRR as an indicator of whether a sputtered thin film might have an acceptable transition temperature or not, since we tested several samples with RRR values far from the 1.2-1.4 range, and none of them exhibited a superconducting transition. Despite this correlation between the RRR value and the superconducting transition of tungsten thin films, using it to tune the transition temperature of W-TES does not appear to be feasible.

The following step in this project concerned the study of these dependencies in sapphire samples.

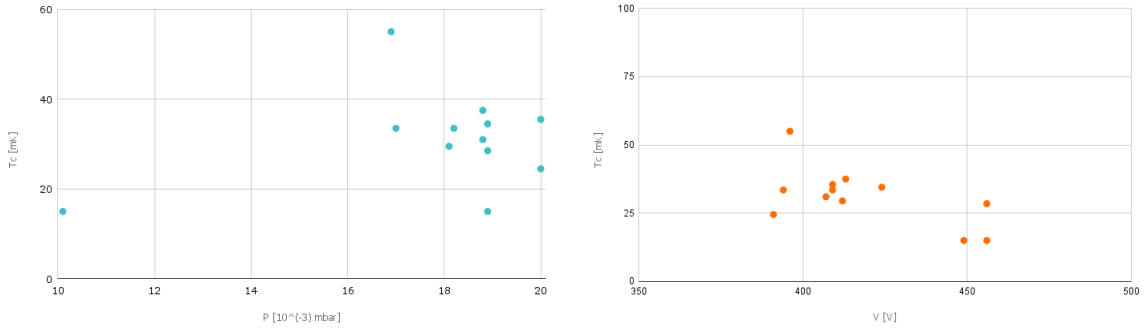

Figure 6.8: *Left:* Plot of the T_C of W thin films sputtered on Si samples as a function of the pressure in the chamber. *Right:* Plot of the T_C for the same samples as a function of the voltage used for the deposition.

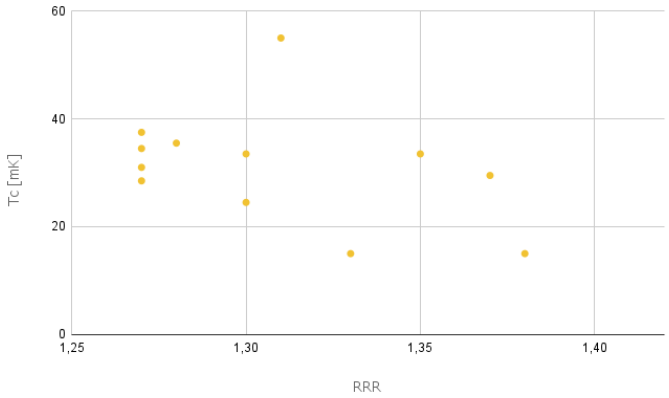

Figure 6.9: Plot of the T_C of W thin films sputtered on Si samples as a function of their RRR value.

Figures 6.10 and 6.11 present the outcomes of these investigations. These findings align with those obtained for the silicon samples.

The inability to replicate previous results could derive from multiple factors. Firstly, the samples in [116] are sputtered without opening the main chamber, nor the load-lock, utilising a specially designed holder that allowed sputtering of multiple samples in a single deposition run. Introducing samples into the main chamber at different times could potentially introduce variations in the sputtering conditions. The different pumping times of the load-locks before the insertion of the samples in the main chamber (varying approximately between 1 hour and 1 day) might also affect the sput-

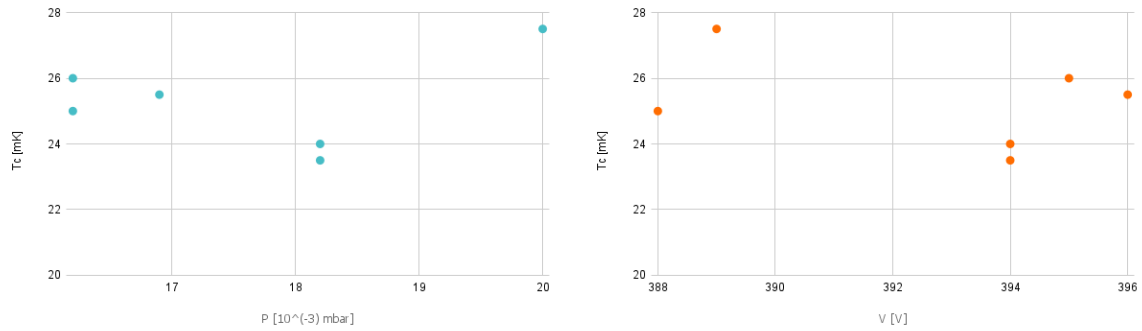

Figure 6.10: *Left:* Plot of the T_C of W thin films sputtered on Al_2O_3 samples as a function of the pressure in the chamber. *Right:* Plot of the T_C for the same samples as a function of the voltage used for the deposition.

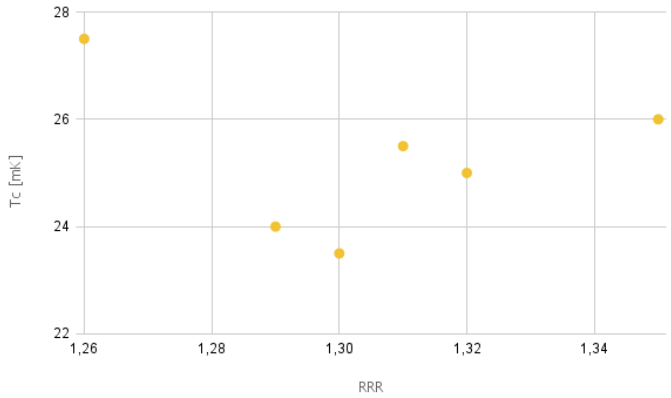

Figure 6.11: Plot of the T_C of W thin films sputtered on Al_2O_3 samples as a function of their RRR value.

tering conditions. However, considering the objective of establishing a procedure for sputtering a large number of detectors for the upcoming CRESST experiment upgrade, conducting a single production run seems impractical.
Additionally, a notable difference between the two studies is the size of the magnetron used. In [116], a 4-inch magnetron was utilised. A new 4-inch magnetron has been acquired by MPP for installation in the new machine, and further investigations will be carried out using this, which should enhance homogenity of the sputtered films.

Although we could not reproduce the previously observed trends in T_C as a function of sputtering parameters, our project successfully achieved stable production of super-

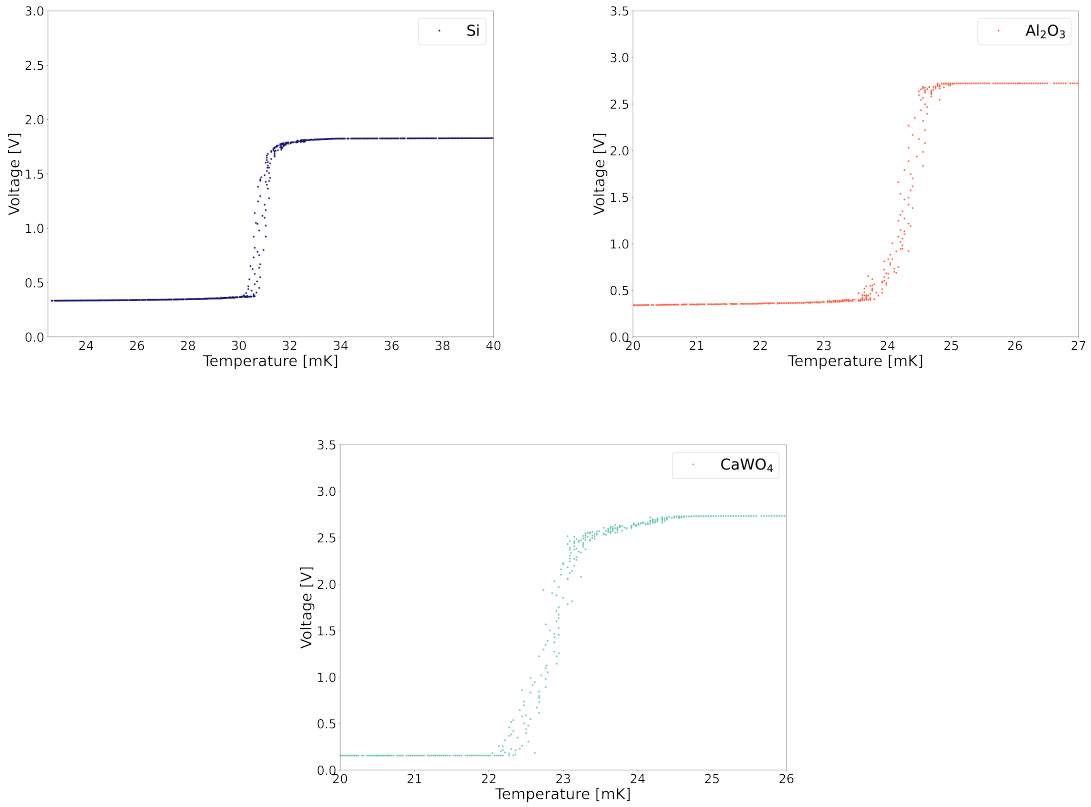

Figure 6.12: Transition curves of W thin films sputtered on different materials. On the top left, Si; on the top right Al_2O_3; on the bottom, $CaWO_4$.

conducting W thin films on various materials. In addition to Si and Al_2O_3, W thin films were successfully deposited on three $CaWO_4$ crystals, all exhibiting a superconducting transition around 25 mK. Selected transition curves are depicted in Figure 6.12.

6.4.4 Stress on W thin films

Within the project of producing the new sensor design described in section 5.4.3, W thin films have been sputtered on the KSFM dielectric photoresist, without the interposition of a Cu layer. Thanks to the softness of the dielectric photoresist compared to the Si substrates, these depositions allowed us to optically observe residual stress in the thin film and investigate its variation with sputtering pressure in the chamber during deposition. Figure 6.13 shows three samples produced at different pressure. As the pressure changes, the stress conditions of the films also change.

With these tests, we realised that sputtering W thin films onto substrates coated with KMFS dielectric photoresist provides a means to address the stress conditions of the films. Observing the different stress conditions is fairly easy, as it can be done with the sole use of a microscope. By adjusting the pressure in the chamber using different values of Xe flow, we can produce and test samples with varying stress levels and study how stress is affected by different sputtering parameters. In the hypothesis that stress influences the superconducting properties of W films, controlling it may enable us to regulate the T_C of our sputtered W films and the characteristics of the produced W-TES.
Furthermore, studying the correlations between sputter parameters, film stress and W-TES properties might allow us to have a means of characterising sputtered TES without needing to test them at mK temperatures, thus drastically reducing the production time demand.

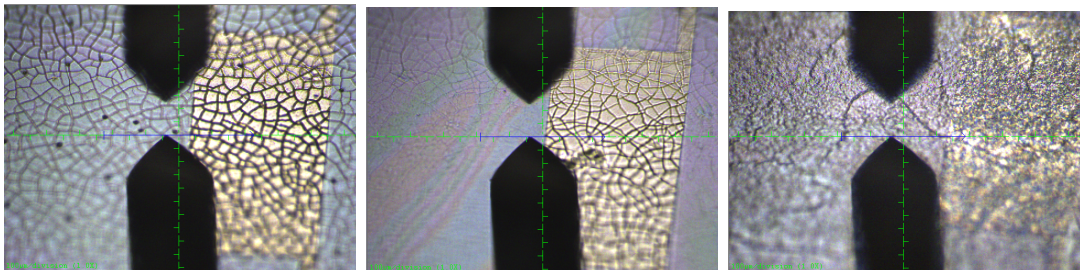

Figure 6.13: Pictures of W thin films produced on substrate coated with KMFS dielectric photoresist at different sputtering pressures seen at the microscope. *Left:* P=$2.76{\cdot}10^{-2}$ mbar. *Centre:* P=$1.66{\cdot}10^{-2}$ mbar. *Left:* P=$3.5{\cdot}10^{-3}$ mbar.

6.5 Conclusions and Outlook

With this work, we have established a reliable procedure for obtaining sputtered superconducting thin films on various materials.
Stress might be the parameter driving the superconducting behaviour of thin films, and by managing it, we may gain control over the transition temperatures of sputtered W thin films. Further research should be directed towards understanding the type and magnitude of residual stress stored in the films. Our findings suggest that sputtering onto substrates coated with KMFS dielectric photoresist offers a convenient and efficient means of studying the stress conditions of the films.
Moreover, the capability to fabricate W-TES directly on top of this dielectric layer would be an asset in producing the new sensor design with an underlying Al phonon collector described in section 5.4.3.

Additional investigations could help fine tuning the procedure to precisely control the T_C of the sputtered W thin films using sputtering parameters.

Chapter 7

The doubleTES

In recent times, a significant challenge hindering the sensitivity of low-mass dark matter direct detection experiments has been the unexpected increase in events occurring close to the energy threshold of the detectors. This background, widely known in the field as the Low Energy Excess (LEE), has prompted considerable efforts within the community to comprehend its origin.
The CRESST collaboration has performed extensive investigations of this background, leading to the development of new detector modules specifically designed to address the remaining possible sources of the LEE. The doubleTES is among these modules, and it has been the focal point of the extensive studies presented in the following.
This chapter begins by detailing the motivation for this novel detector design, outlining the experimental investigations of the LEE conducted by the CRESST collaboration and the subsequent findings. Afterwards, the concept behind the doubleTES design is introduced, along with the details regarding the fabrication of the prototypes. Following this, the chapter delves into the data analysis procedure employed in this work, followed by the outcomes of various tests of the prototypes conducted in the above-ground facility of the Max Planck Institute for Physics. Some of these results are also detailed in [138]. Finally, the chapter presents the ongoing underground measurement of various doubleTES detector modules named Run37.

7.1 Motivation

The LEE has garnered the attention of numerous scientists worldwide. Despite the considerable efforts of various experiments to understand this signal, its origin remains elusive. Within the framework of CRESST, extensive investigations have been undertaken to comprehend this signal. In particular, we addressed numerous hypotheses by implementing minimal changes to our detector design. These studies have yielded insights into several characteristics of the LEE, as outlined below. A new generation of CRESST detectors has been developed to probe the remaining open hypotheses.

In the following, we present the experimental studies of the LEE conducted by the CRESST collaboration.

7.1.1 The Hunt for Low Energy Excess

During the first measurement campaign of the CRESST-III Phase, named Run34, the detector modules achieved unprecedentedly low thresholds below 100 eV, allowing the exploration of a new portion of the parameter space.
In 2019, CRESST was the first experiment to report the observation of a rise of events above a flat background at energies below 200 eV (see Figure 7.1) [86]. This rise of events could be observed across all detectors reaching a threshold below 100 eV. While this signal exhibited a featureless spectrum, which could easily be mistaken for dark matter, differences in the spectral shapes among different detectors precluded a single common origin for these events. Consequently, the interpretation of this signal as solely attributable to dark matter was immediately dismissed, leaving behind the need to understand its origin.

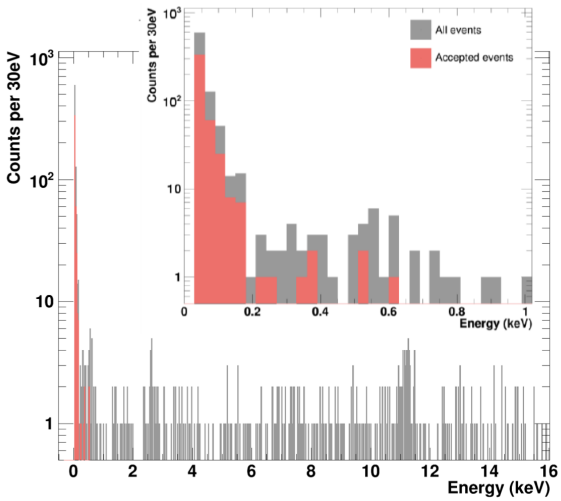

Figure 7.1: First observation of the low energy excess in CRESST in the first measurement campaign of CRESST-III. Picture taken from [86]

Subsequently, during the following measurement campaigns, Run35 and Run36, we explored several hypotheses regarding the origin of this signal, implementing minimal modifications to the standard CRESST-III detector design. In the following, we review the tested hypotheses, detailing the modifications made to the detector design to address them. Notably, during Run35 two detectors remained unchanged and served as control detectors.

Mounting Direction

Since all detectors were mounted in the same direction in Run34, we hypothesised that altering the mounting direction could influence the observed LEE. In light of this, one detector was measured with a different mounting orientation (i.e. horizontally instead of vertically) than the previous measurement campaign.

Surface Polishing

$CaWO_4$ is very brittle, rendering it susceptible to surface damage during the TES production process. We investigated the straightforward hypothesis that such damages might contribute to the excess events. For Run35, two $CaWO_4$ crystals previously utilised in Run34 underwent repolishing on all sides post TES production, while an additional newly polished $CaWO_4$ crystal was also included in the measurement. The remaining $CaWO_4$ crystals were not subject to the same procedure.

Material Dependence

During Run34, all detector modules featured a $CaWO_4$ crystal as the main absorber, prompting speculations that the LEE's origin could be related to the material. Consequently, in Run35, two modules employed Al_2O_3 crystals as the main absorber. In Run36, the main absorber crystal was Al_2O_3 in three modules and $LiAlO_2$ in two modules, while one module presented both the main absorber and wafer detectors made of Si.

Scintillation light

In the first run of the CRESST-III Phase, all detectors were mounted in a fully scintillating housing. The possibility of photons originating in the scintillators and directly hitting the TES sensors was considered a potential source of the LEE. Consequently, all non-active scintillating components of the detector modules were removed.
Furthermore, in Run36, a fully non-scintillating module was measured. This module featured a main absorber made of silicon, a non-scintillating material coupled to a silicon wafer detector of the same geometry as the standard light detector. This setup enabled the investigation of coincidences between the two detectors instead of the scintillation light as in the standard configuration.

Internal relaxation of the lattice stress

To study the impact of the lattice stress of the crystals on the LEE rate, in Run36, we employed commercial $CaWO_4$ crystals in two detector modules. Furthermore, we compared the internal stress of the crystals grown in two different manufactures.

Stress induced by holding structure

To investigate the influence of the holding structure on the LEE rate, we implemented changes to the holding scheme of several detector modules in Run36. The following outlines the various holding schemes utilised:

- Instrumented $CaWO_4$ sticks: these sticks were specifically designed and employed to examine how events occurring within the holder and transmitted to the main absorber crystal manifest in the main target.
- Copper sticks: these metal sticks (i.e. with a very low heat capacity) were introduced to suppress possible events occuring in the holder.
- Bronze clamps: the holding by sticks was replaced by a different holding system with bronze clamps. By adopting this alternative holding scheme, we aimed to verify whether the pointy sticks might induce cracks at the interface with the crystal, potentially resulting in low-energy events.

Detector geometry

We analysed light detector crystals as main absorbers to assess the impact of volume and surface area, on the LEE rate. These crystals possess a significantly thinner geometry compared to the absorber crystals, measuring $20\times20\times0.4\,\mathrm{mm}^3$ instead of the standard $20\times20\times10\,\mathrm{mm}^3$ absorber crystals. Therefore, any effects stemming from the volume or surfaces of the crystals should be discernible when comparing results from a light detector with those from a standard main absorber.

A summary of the different detector modules tested during Run35 and 36 is depicted in Figure 7.2. This schematic representation illustrates the various modifications implemented to investigate hypotheses regarding the origin of the LEE.

Comparing results across the various modules, we could not observe significant differences in the LEE rates attributable to any modifications. These comprehensive studies allowed us to exclude several hypotheses, enhancing our understanding of the LEE.

LEE Decay

The rate of the LEE was observed to decay over time, characterised by two time constants: a fast one (of the order of a few days) and a long one (of the order of 200 days). This decay pattern was consistently observed across all detector modules. Notably, the diversity in the observed time constants contradicts the interpretation of this signal as arising from a radioactive background.

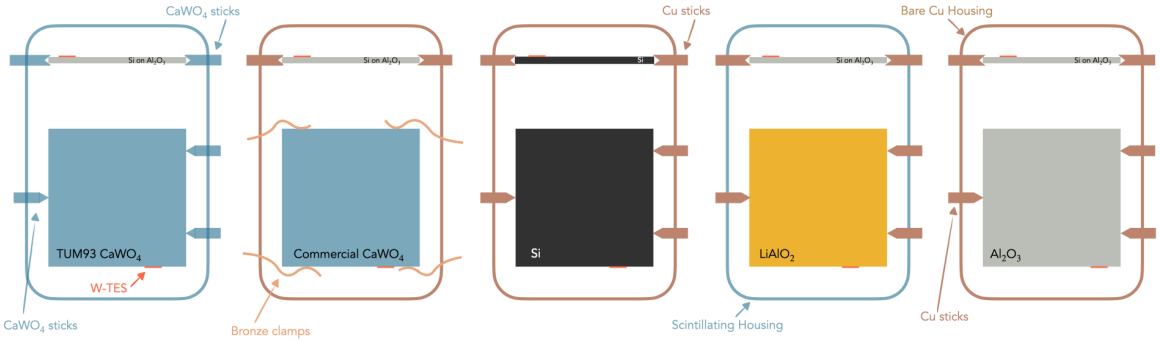

Figure 7.2: Schematic representation of the different modules tested during Run35 and 36, comprehending all the modifications to the standard detector design.

Thermal cycles

Following up on an observation by the EDELWEISS collaboration, which reported an increase in the rate of heat-only events after a warm-up of the cryostat to 30 K during measurement, the CRESST collaboration started systematic thermal cycles to investigate this phenomenon. Figure 7.3 presents the results of the warm-up tests of the light detector of one of the Si modules as an example. These results demonstrate that the fast-decaying component can be reactivated following thermal cycles from the working temperature of a few mK to a few tens of K. Additionally, the plot indicates that the neutron calibration does not influence the LEE counting rate [87].

Figure 7.3: Plot of the decay of the LEE rate in time, comprehending the performed warm-up tests, showing a recharge of the LEE fast component.

The extensive studies conducted to understand the LEE have yielded valuable insights. Nonetheless, the origin of the LEE has yet to be understood. Consequently, the CRESST collaboration has developed three new detector modules to comprehend or veto LEE events while enhancing sensitivity at low energy. These modules are presented in [89].
The following section will provide a detailed presentation of the doubleTES detector module, together with the results of the above-ground tests of the prototypes.

7.2 DoubleTES Detector Module

The basic idea behind the doubleTES detector module is to equip the main target with two identical W-TES, each with independent readout. This design allows to investigate whether the origin of the LEE events is sensor-related. By combining the data from the two sensors, we can identify events originating in close vicinity to the sensors. This is achieved by analysing the 2D energy spectrum of the detector. If an event originates within the bulk of the crystal, the two sensors are expected to respond similarly and measure nearly identical energies. Conversely, if an event originates in close proximity to one of the two sensors, we expect the responses of the two sensors to differ significantly, resulting in diverse energy measurements. Figure 7.4 provides a schematic representation of the working principle of the doubleTES.

7.2.1 Description

In its standard realisation, the doubleTES utilises the same crystals as the standard CRESST-III module: a $20\times20\times10\,\mathrm{mm}^3$ $CaWO_4$ crystal as the main absorber, coupled to a $20\times20\times0.4\,\mathrm{mm}^3$ SOS crystal as light detector, for particle identification.
This detector features a gravity-assisted holding scheme, developed by the CRESST collaboration within the framework of the new generation of CRESST detectors and detailed in [89]. The crystal is resting on a minimal amount of copper, held solely by its own weight rather than clamps or sticks. This holding scheme minimises the forces exerted on the crystal and allows to investigate their impact on the LEE. A technical drawing of this module is provided in Figure 7.5.

7.2.2 Production details

The two W-TES are simultaneously deposited onto the crystal surface in an evaporation process (see chapter 6 for details about the process). The key to the functionality of this detector module is the similarity between the two W-TES, which enables simultaneous stabilisation, as detailed in section 7.4.3. Achieving very similar transition temperatures for both sensors is crucial, to minimise the thermal interference between the two sensors and enable independent stabilisation of each sensor in its operating

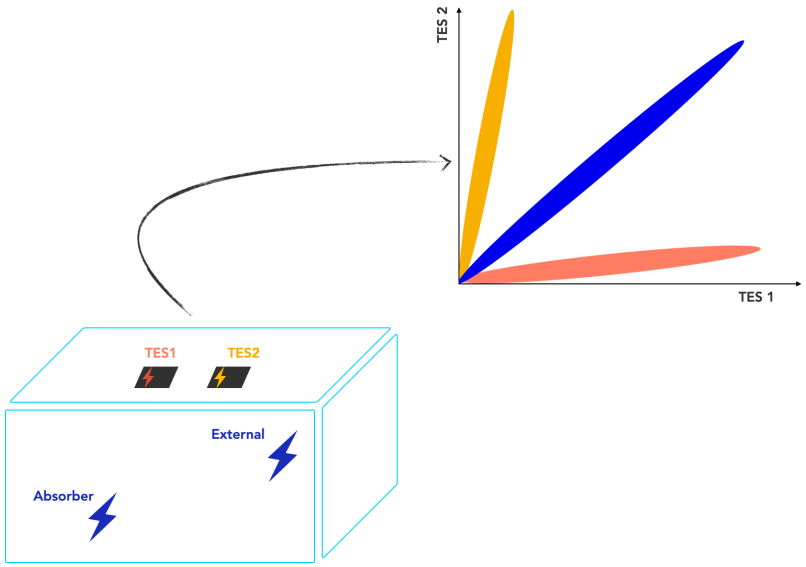

Figure 7.4: Schematic representation of the signal originating from different sources in the doubleTES detector module. In a plot with the energies of the two TES as axes, we expect a clear separation of the events originating in the bulk of the crystal from those originating in the two sensors.

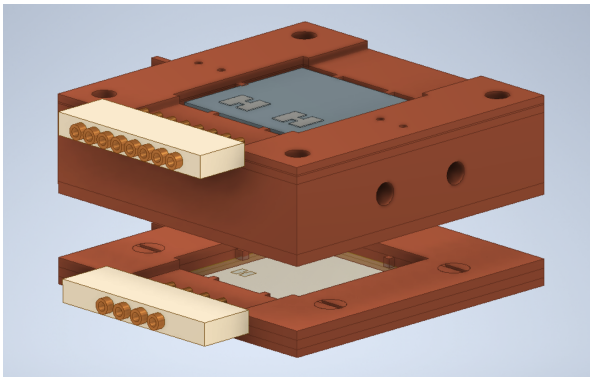

Figure 7.5: Technical drawing of the doubleTES in its standard realisation. The main absorber is equipped with two identical TES and coupled to a standard light detector. Both crystals rest on a minimal amount of copper, exploiting the gravity-assisted holding scheme. The holes on the side of the copper structure are used to place calibration sources when needed.

point.
Our sensors are stabilised in their operating point by a current sent through the heater

element, typically placed on the crystal's surface near the TES. Each sensor of the doubleTES detector module requires independent stabilisation. Placing the heater near the sensor risks substantial thermal cross-talk between the TES, as the heater element would heat the entire crystal. To mitigate thermal interference, we deposited the heater directly on top of the tungsten film and electrically isolated the two films using a sputtered 350 nm thick layer of SiO_2.

The TES used in the absorber crystal are two "phonon-S" TES (see [108]), which consist of a 0.6 mm long and 1.7 mm wide tungsten film as thermometer, a 1 mm long and 0.04 mm wide gold thermal link and two 0.95 mm long and 4.0 mm wide aluminium phonon collectors. Based on the studies of the TES design (see section 5.4), the phonon collectors are made of aluminium only (single-layer phonon collectors) to enhance the detector's sensitivity. A drawing of one of the complete sensors of the doubleTES can be found in Figure 7.6.
The TES deposited on the light detector is a standard CRESST light detector TES in its single-layer version.
The heaters are small gold films with two aluminium bond pads. All the bond pads are designed to have all the bond wires of the same length and parallel.

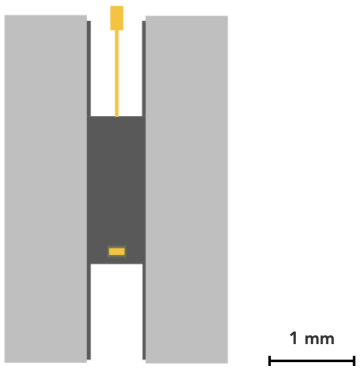

Figure 7.6: Drawing of one of the two sensors of the standard doubleTES module. The parts are represented in scale.

7.3 Data Analysis

All measurements presented in this chapter follow the same analysis procedure, which consists of several steps. Initially, the raw data are processed. Next, the analysis of the processed data generates the energy spectrum. Finally, the results are interpreted in terms of physics results.

For a better understanding of the following, some basic concepts are introduced below, followed by an outline of the analysis flow.

Run: A measurement campaign starting with the cool-down and ending with the warm-up of the cryostat.

Record window: The number of samples considered when a trigger is fired. It must be long enough to contain the entire pulse but not be too long as to cause pile-up, especially in above-ground measurements. The chosen length is 8192 samples, corresponding to 327.68 ms, with the triggering sample placed at one-quarter of the record window, defining "pre-trigger" and "post-trigger" ranges.

Event: When one readout channel triggers, all channels are simultaneously recorded. An event is defined as the combination of information from all of the channels.

Heater Pulse: Artificial pulses sent to the sensors via the heater element. The largest heater pulse saturates the sensor, providing precise operating point information, and thus monitoring the detectors' stability. The other heater pulses span the sensors' linearity range to extend the energy calibration.

Particle Event: An event caused by a particle interaction in the absorber crystal.

Empty Baseline: Randomly extracted record windows where no channels triggered. These are used to create the Noise Power Spectrum (NPS) and determine the energy threshold.

Simulated Event: Simulated events created by superimposing desired pulse shapes onto the data stream.

Template Pulse: An event pulse shape created by averaging particle pulses from the 5.9 keV ^{55}Fe peak. It is also called a standard event.

Noise Power Spectrum: Created from cleaned empty baselines (without residual pulses or artefacts) to inform about noise frequencies. Constructed by Fourier transforming empty baselines $\hat{n}(w)$, multiplying by their complex conjugate $\hat{n}^*(w)$ and averaging:

$$N(w) =< \hat{n}(w)\hat{n}^*(w) > \tag{7.1}$$

Optimum Filter: A filter to maximise the signal-to-noise ratio by re-weighing frequencies via the optimum filter (OF) transfer function H(w) [139]:

$$H(w) = K\frac{\hat{s}^*(w)}{N(w)}e^{-iw\tau_m} \tag{7.2}$$

where $\hat{s}^*(w)$ denotes the complex conjugate of the signal pulse shape's Fourier transform (obtained from the template pulse), K is a renormalisation constant, and τ_m represents a phase.

7.3.1 Trigger

The data acquisition for these measurements employs a software-triggered methodology, where the entire data stream is recorded and triggered offline. This approach is chosen because it allows to trigger the same data in different ways, thus to obtain as much information as possible from the data.
The triggering process starts by constructing an optimum filter for each detector, utilising their specific NPS and template pulse. Once the filters are constructed, the filtered stream is subject to a trigger algorithm to detect pulses above a defined threshold value.

7.3.2 Pulse Parameter Calculation

Once the pulses have been identified through the trigger, they are processed by an Event Builder algorithm. In this step, the trigger timestamps from the different channels are grouped to form the events of the detector module. These events and basic parameters, such as the timestamp and readout channel, are saved. This algorithm also categorises the events. Since the acquisition software provides information about the timing of the test pulses, these can be tagged and identified by comparing these saved timestamps with the trigger timestamps.
During this step, the number of empty baselines (random triggers) to be extracted from the continuous stream must be specified. When processing the data for threshold estimation, we opt for extracting a large number of empty baseline, as having clean empty baselines, with no residual pulses can be challenging in above-ground measurements, depending on the size of the crystal. For the final physics analysis, we opt for no empty baselines. Afterwards, the pulses undergo a Calculation of Main Parameters (CMP) algorithm. Baseline parameters are extracted from the pre-trigger range, with key parameters being the baseline RMS, slope and offset. The baseline offset is crucial for this analysis, serving as the basis for the working point cut (described in the following).
The CMP algorithm also provides other important pulse parameters, such as baseline difference, pulse height, peak position, decay time, rise time, and maximum and minimum derivatives. The pre-processing of the data stream concludes with the calculation of pulse parameters.

7.3.3 Threshold Estimation

After processing the data with the correct OF, the trigger threshold needs to be determined. Following this step, the continuous stream will undergo the trigger, event builder and CMP algorithms for the last time.
For above-ground measurements, the trigger threshold in CRESST is typically set to five times the baseline resolution (σ_{BL}), as described in [140]. The first step in this process consists of creating a clean list of EBLs, which are baselines free of residual pulses and artefacts. An algorithm then superimposes a pulse of a well-defined amplitude (0.01 V in this work) onto each baseline and evaluates its amplitude with the filter. Since the pulses superimposed on the empty baselines are free from noise and have a well-defined amplitude, the width of their amplitude distribution serves as an indicator of the noise present in the empty baselines. This distribution is fitted with a Gaussian distribution function, and the resulting σ defines the baseline resolution of the detector. Figure 7.7 shows an example of such a fit.

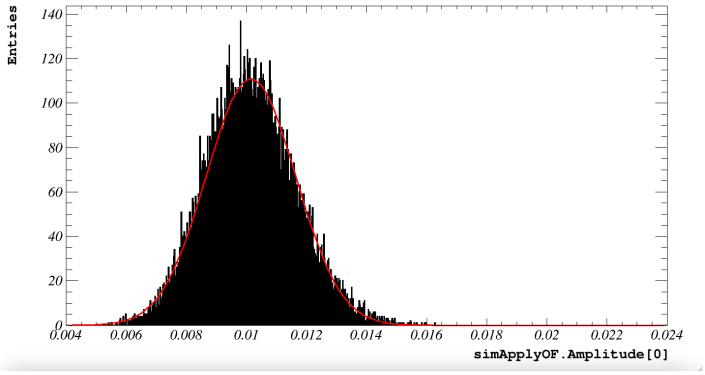

Figure 7.7: Plot of the fit to the Gaussian distribution used to compute the baseline resolution. This distribution is obtained by superimposing pulses of 0.01 V to a clean list of EBLs and then filtering them. Plot taken from the analysis of the silicon-on-sapphire doubleTES module.

This is one of many possible threshold definitions. Another common way to define the threshold is by setting it to allow a certain number of noise triggers to be accepted as pulses. This method is described in [141, 142]. For above-ground measurements, accepting that 1% of the total triggers are noise triggers has proven to be a good estimate [57].
In this work, the threshold is given as five σ_{BL} and always cross-checked with the second method to ensure the validity of this choice, such that the accepted number of noise triggers is compatible with 1% of all triggers.

7.3.4 Working Point Cut

Once the final processing of the data stream with the chosen OF and threshold is complete, the first step in the analysis chain consists of performing a working point cut to ensure the detectors are stable in their operating point.
During normal operation, we select the working point of our sensors in the middle of their superconducting transitions and stabilise them at a specific temperature. This temperature corresponds to a particular resistance value of the film, defining the operating point.
We only consider pulses originating from specific resistance values around the chosen working point to ensure the detector's stability during operation. This selection involves both sensors in a doubleTES: we only consider pulses where both sensors are at their correct working point.
Performing this cut is non-trivial. The resistance value at the working point is read out by the SQUIDs as a voltage, represented by the baseline offset. As described in section 4.3, the SQUID response is periodic with a period of one flux quanta, leading to a sequence of possible quantised baseline offset values, as shown in Figure 7.8 (left). To select values around the chosen working point, we need to eliminate the periodicity effect and obtain a continuous distribution of the baseline offset centred around one single value, describing the operating point. Therefore, we shift every distribution by an entire number of flux quanta. The accepted stability region is then selected on this distribution (see Figure 7.8, right).

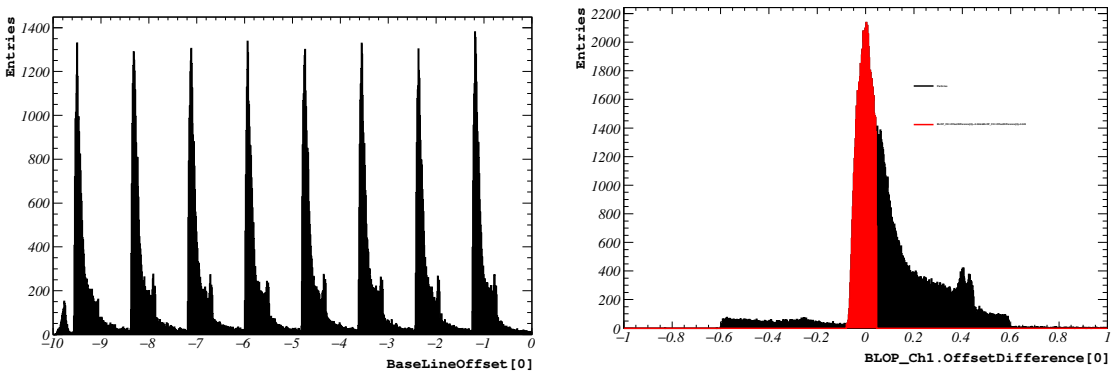

Figure 7.8: *Left:*Plot of the baseline offset of the TES1 of the down $CaWO_4$ doubleTES detector. This parameter in this measurement takes eight different values, shifted by a quantised amount. *Right:* Distribution of the baseline offset obtained by shifting all baseline offset distributions by an entire number of periods. The part highlighted in red represents the accepted region of this distribution. Plots taken from the analysis of the up $CaWO_4$ module described in section 7.4.4.

7.3.5 Quality Cuts

Having defined a set of stable pulses for both detectors, quality cuts are applied to the pulse parameters to discard those with issues such as tilted baselines, electronics artefacts, resetting pulses or pile-up. These cuts follow a consistent scheme across all detectors and measurements, and they are described in the following.

Baseline Difference

The baseline difference is the difference between the average of the first 50 samples and the average of the last 50 samples of the record window. This parameter helps identify and tag events, such as flux quantum losses and decaying baselines.

- **Decaying Baselines:** These events usually occur after a large energy deposition in the crystal. If the detector has not returned to its original baseline value due to the large energy deposition, it may trigger again in the following record window.
- **Flux Quantum Losses:** These typically have a very fast time, surpassing the electronics slew rate, causing the SQUID feedback loop to fail to follow the rapid rise, leading to a flux quantum loss in the SQUID (see section 4.3). As a result, the SQUID locks into a different baseline offset value after the pulse.

Baseline RMS

The baseline RMS describes the RMS of the linear fit performed by the CMP algorithm to the pre-trigger range of the pulses. This parameter provides information about irregularities in the pre-trigger range, such as the presence of small pulses before the triggered pulse. When two pulses appear in the same record window, the event builder centres the largest pulse at the correct position (1/4 of the record window). Thus, if a small pulse precedes the triggered one, it will appear in the pre-trigger range. A cut on this parameter helps to eliminate such pile-up events.

Baseline Slope

The baseline slope parameter describes the slope of the baseline of a pulse. This allows the identification and exclusion of pulses superimposed on slightly decaying baselines.

Delta Voltage

The delta voltage is the ratio of the minimum derivative and the baseline RMS. This parameter helps to tag electronic artefacts, such as electronic spikes, by identifying pulses where there is a sudden change between two consecutive samples beyond the normal noise level.

After applying cuts on these basic pulse parameters, the remaining pulses are filtered for a more precise amplitude estimation. The filter estimates the amplitude of the pulses as the difference between the highest point of the record window and the baseline value. The highest point can either be searched for by the filter itself, or it can be computed as the value in a specific position. Typically, for the amplitude estimation of particle events, the maximal value is computed at the trigger timestamp. For the analysis of the doubleTES module, we decided to have the maximal value searched for by the filter, within a small range around the trigger timestamp. This timestamp is defined by the first channel triggering, thus it can be shifted by a few samples for the second channel. Knowing the exact position of the pulses is crucial for an optimal energy estimation.

OF RMS

The OF RMS parameter measures the difference between the filtered puses and template pulses used to construct the filter. It represents a valuable pulse shape parameter, enabling the distinction between valid particle pulses and pulses with a different pulse shape.

Peak RMS

Peak RMS is the difference between the filtered pulses and template pulses, calculated in a small region around the peak. This parameter is typically not used in this analysis due to its strong energy dependence. Indeed, performing pulse shape discrimination on the peak at very low energies is extremely challenging, given the proximity to the threshold.

7.3.6 Energy Calibration

The calibration source used in these above-ground measurements is a ^{55}Fe source. ^{55}Fe decays via electron capture to ^{55}Mn, leaving a vacancy in the K shell of ^{55}Mn. This vacancy is filled by an electron from a higher shell, resulting in the emission of K_α and K_β lines of ^{55}Mn are at 5.89 keV and 6.49 keV respectively [143].
These known energy peaks are used to calibrate the test pulses from the heater. The calibrated test pulses are then used to extend the calibration across the entire dynamic range of the detector.

To ensure the validity of this calibration, the detector response has to be linear up to the energy of the ^{55}Fe peaks. Moreover, it is essential to have well-distributed test pulses across the detector's dynamic range and to ensure that at least one pulse is approximately as energetic as the iron X-rays. The linearity of the detector is evaluated by plotting the detector output signal in response to the test pulses as a function of the injected amplitude in volts. If a detector is linear from its threshold to the iron

energy, the calibration can be easily interpolated across the entire dynamic range. More attention is required when performing the calibration if the calibration energy exceeds the linear range of the detector. A description of the possible calibration methods for these situations is beyond the scope of this work, as linearity is confirmed for all measurements hereby presented.
Once the linearity has been confirmed, the calibration proceeds by comparing one of the test pulses to the ^{55}Fe 5.89 keV peak using a simple proportion:

$$V_{Fe} : 5.89\,keV = V_{TP} : E_{TP} \tag{7.3}$$

where $V_{Fe/TP}$ denote the output signals in volt corresponding to the ^{55}Fe peak at 5.89 keV and the chosen test pulse, respectively, while E_{TP} represents the unknown injected energy corresponding to the chosen test pulse.
In the second step of this two-step calibration, our goal is to calibrate each pulse based on the detector's response at the time of the event. Thus, we perform an event-by-event calibration, taking into account the specific working point of the detector for each event. This approach maximises the exposure by rejecting only those events that originate from a different operating point than the selected one.
For this scope, the test pulse amplitude is plotted against the baseline offset distribution obtained for the working point cut, as shown in Figure 7.9. This plot is fitted linearly, and the fit results are used to extend the calibration across the entire dynamic range. This extension accounts for the specific working point of the detector for each event.

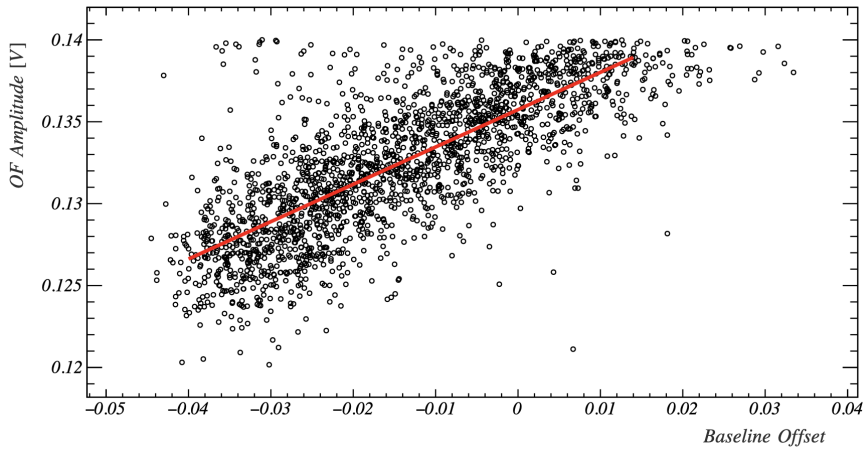

Figure 7.9: Plot of one of the test pulses amplitude as a function of the baseline offset value. The red line represents the linear fit to this distribution, which is used for the event-by-event-based calibration.

The calibration equation is:

$$E = \frac{Amp_{OF}}{(a \cdot BL_{offset} + b)} \cdot E_{TP} \tag{7.4}$$

where a and b are the parameters of the linear fit, Amp_{OF} denotes the amplitude computed by the OF, BL_{offset} represents the baseline offset value for the specific event and E_{TP} is the known energy of the test pulse used for the fit.

In this work, the energy resolution of the sensors is computed as the σ of the double Gaussian fit of the K_α and K_β lines from the ^{55}Fe calibration source.

7.3.7 Absorber Events Cut

This cut has been specifically designed for this module to locate the origin of the events. As described in section 7.2, the doubleTES was designed to distinguish the origins of different events by analysing the difference in the signal responses of the two sensors. This difference varies depending on whether an event originates in the bulk of the crystal or in the proximity of one of the two sensors. For events occurring in the bulk of the crystal, the signal detected by both TES is expected to correspond to the same deposited energy. However, for events occurring near one of the sensors, the signal will be significantly different between the two sensors. Thus, by plotting the ratio of the energy detected by the two sensors against the energy detected by one of them, we expect to see distinct bands:

- A band centred around 1, representing bulk events.
- Two additional bands: one above 1, representing events near the sensor whose energy is in the numerator, and one below 1, representing events near the sensor whose energy is in the denominator.

Since dark matter interactions are expected to occur in the bulk of the crystal, this newly designed "absorber events cut" aims to accept only those events. The cut is designed on the plot of the ratio of the energy detected by the two sensors according to the specific condition of each measurement.

7.3.8 Survival Probability

The final step in the doubleTES analysis is the survival probability calculation, which determines the probability that a particle event is included in the final spectrum.
This survival probability is computed through a simulation process. Artificial events of a known pulse shape are superimposed onto the data stream and processed as the real data using the previously defined analysis chain. For the doubleTES, performing

a correlated simulation of the two channels that considers the amplitude ratio between events in the two sensors and their relative positionis is crucial.
Artificial pulses are created by scaling the template pulse used for the OF and superimposing them at random positions in the stream. This process mimics real conditions, providing a realistic representation of the true situation. However, it is challenging in above-ground measurements due to the limited number of empty baselines. Therefore, it is essential to balance the number of simulated pulses to ensure sufficient statistics without excessive pile-up hindering successful analysis.
Before computing the survival probability, it is important to obtain information about the trigger efficiency, i.e. the probability that a simulated event causes a trigger, as the survival probability cannot exceed this value. This information is particularly relevant for above-ground measurements, where pile-up is expected to reduce this efficiency, limiting the signal survival probability.
The list of simulated events that caused a trigger is then subjected to the full analysis chain. The percentage of simulated pulses surviving to all cuts represents the survival probability of events. This is typically used to correct the energy spectra by dividing each bin of an energy spectrum by the corresponding bin of the survival probability histogram. This correction allows for the comparison of energy spectra from different measurements.

For this work, the main objective of the survival probability calculation is to understand the effectiveness and energy independence of the absorber events cut, ensuring that events originating from the bulk of the crystal are accurately identified.

7.4 $CaWO_4$ doubleTES

The prototype of the doubleTES consisted of a $20\times20\times10\,\mathrm{mm}^3$ $CaWO_4$ crystal, produced exactly like the main absorber of the complete module described in section 7.2.1, but not coupled to a light detector. Figure 7.10 shows a picture of this module. During this prototyping phase, we prepared two identical $CaWO_4$ detectors.

7.4.1 Experimental set-up

This prototype was measured at the above-ground facility of the Max Planck Institute for Physics (MPP) in Munich. We employed a dilution refrigerator from Leiden Cryogenics. This cryostat features a round detector plate with a 10 cm diameter and it houses four APS-581 SQUIDs for readout. The temperature of the detectors is read and monitored using a thermometer placed at the detector plate.
To mitigate the issue of event pile-up, which is a common challenge in large crystal measurements at sea level, we installed a shield composed of 10 cm thick lead bricks around the cryostat, as shown in Figure 7.11. The shielding was borrowed from the COSINUS ([144]) group at MPP.

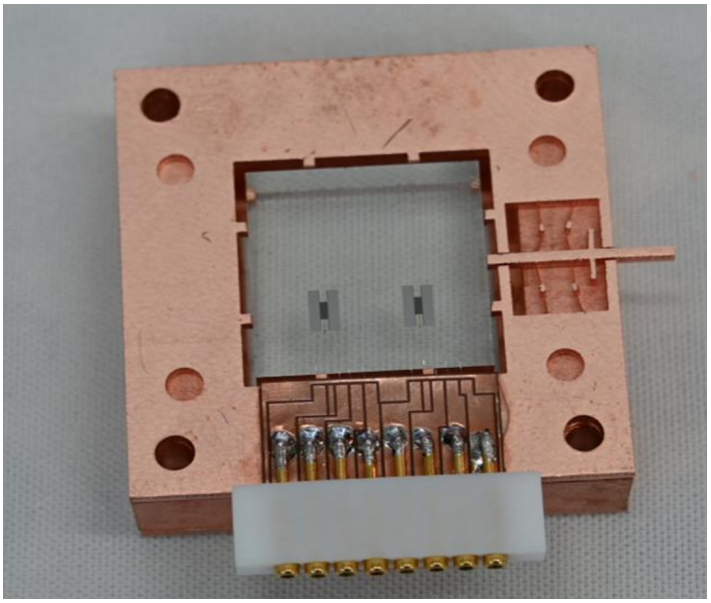

Figure 7.10: Photo of the assembled doubleTES detector in its prototype. The picture shows the two identical TES from the top and the crystal mounted in the gravity-assisted holding scheme.

The data acquisition system records a continuos data stream and the triggering is then performed offline, as described in section 7.3.1. The continuous data stream from the module is recorded on disk using a National Instruments board (NI USB-6218 BNC) at a sampling rate of 200 kHz.

7.4.2 Measurements

Two different measurements were performed with the first prototype of the doubleTES. In both measurements, we mounted the two doubleTES crystals on top of each other and inside a mechanical decoupling system (see Figure 7.12).

First Measurement

During the first measurement, the crystals were equipped with two iron (^{55}Fe) sources for calibration (see section 7.3.6). The sources were placed in the holes on the side of the Cu holder (as shown in Figures 7.5 and 7.12), ensuring that each source was positioned close to one of the two sensors. This arrangement was designed to ensure independent calibration of the two TES and investigate the sensors' energy share. The two crystals were named "up doubleTES" and "down doubleTES" according to their

position within the holder.

Figure 7.11: Photo of Cryo 2 closed and surrounded by a 10 cm thick lead shield in the above-ground facility of the Max Planck Institute for Physics in Munich. The lead shield was borrowed from the COSINUS group at the Max Planck Institute for Physics. The picture was taken during the data taking of the first measurement of the first doubleTES prototype.

Second Measurement

In the subsequent measurement, one ^{55}Fe source per crystal was removed. This modification aimed to verify the first measurement's findings regarding the energy shared between the two sensors.

7.4.3 Thermal Analysis

In the initial phase of our experiment, we focused on understanding the thermal interactions between the two sensors to assess their impact on performance. In the following, we aim to empirically understand the thermal interactions between the two sensors in such a detector.

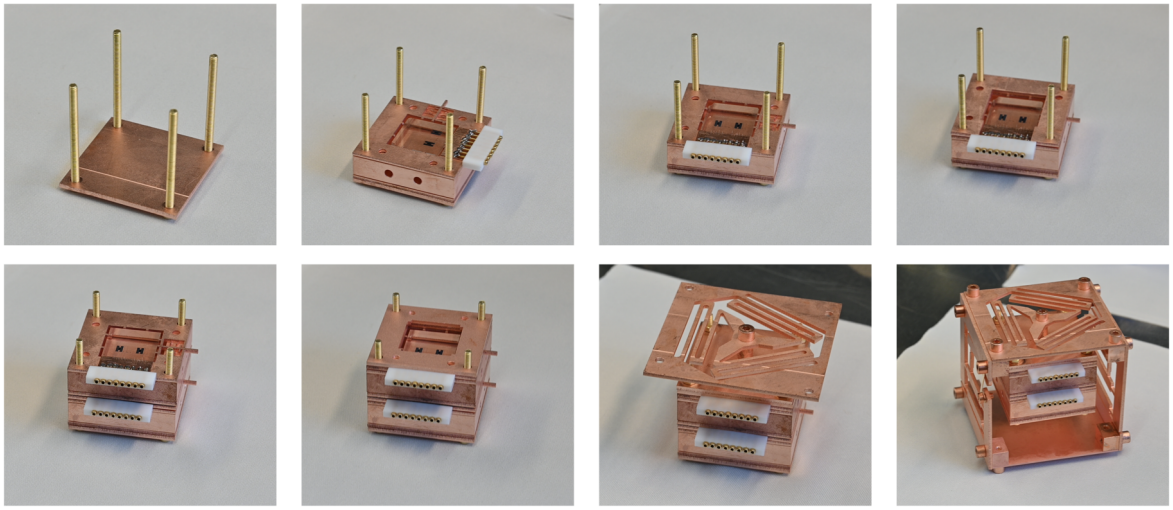

Figure 7.12: Photos of the mounting of the doubleTES crystals for the first above-ground test. The two identical crystals are mounted on top of each other and inside a mechanical decoupling system for vibration damping.

Simplified Thermal Interaction Model

We can describe the behaviour of the two sensors with the following simplified model equations:

$$T_{C,1} - T_{bath} = g_{11}P_1 + g_{21}P_2 \tag{7.5}$$

$$T_{C,2} - T_{bath} = g_{22}P_2 + g_{12}P_1 \tag{7.6}$$

where $T_{C,1/2}$ denote the transition temperatures of the two TES on the crystal, which will be named TES1 and TES2, T_{bath} represents the temperature of the bath during operation, $P_{1/2}$ are the heating power through the heater elements 1 and 2 respectively, and $g_{1,1}$, $g_{1,2}$, $g_{2,2}$, $g_{2,1}$ define the thermal coupling of the two TES to their own and each other's heaters. The heating power through the heater elements is directly proportional to the voltage value (DAC) given as an input to the heater source used to drive the current through the heater. Taking this into account, we can rewrite 7.5 and 7.6 as:

$$T_{C,1} - T_{bath} = g_{11} \cdot aDAC1 + g_{21} \cdot bDAC2 \tag{7.7}$$

and

$$T_{C,2} - T_{bath} = g_{22} \cdot bDAC2 + g_{12} \cdot aDAC1 \tag{7.8}$$

where a and b are proportionality constants.

Empirical Measurements

To empirically solve these equations, we study two limit cases: DAC1 = 0 and DAC2 = 0.

- **DAC1 = 0:** Setting DAC1 = 0, the equations simplify to:

$$b \cdot g_{21} = \frac{T_{C,1} - T_{bath}}{DAC2} \tag{7.9}$$

and

$$b \cdot g_{22} = \frac{T_{C,2} - T_{bath}}{DAC2} \tag{7.10}$$

We measure the value of DAC2, which brings TES2 into its operating point, and then the value of DAC2, which brings TES1 into its operating point.

- **DAC2 = 0:** Setting DAC2 = 0, the equations simplify to:

$$a \cdot g_{11} = \frac{T_{C,1} - T_{bath}}{DAC1} \tag{7.11}$$

and

$$a \cdot g_{12} = \frac{T_{C,2} - T_{bath}}{DAC1} \tag{7.12}$$

We measure the value of DAC1 that brings TES1 into its operating point and the value of DAC1 that brings TES2 into its operating point.

To check the operability of the module, we perform the same type of measurements for other values of DAC1 and DAC2 for both TES to ensure that the two sensors can be simultaneously optimised using both heaters. The results of these tests are shown in Figure 7.13 for both of the doubleTES modules.

To empirically address the limit cases, obtaining the transition temperatures of the two TES is essential. For precise estimates, we gradually heat the mixing chamber, recording both sensors' transitions and then cool it down slowly while recording the temperatures once again. Figure 7.14 presents the transition curves of both TES for both doubleTES modules, indicating that the sensors in each module exhibit closely aligned transition temperatures. This observation suggests the potential for smooth and straightforward simultaneous stabilisation.

We can solve the equations for the up doubleTES module. The temperature of the bath during operation was 10.5 mK and we estimate $T_{C,1}$ = 20.7 mK and $T_{C,2}$ = 20.9 mK. Substituting the values into the equations for DAC1 = 0

$$b \cdot g_{21} = \frac{T_{C,1} - T_{bath}}{DAC2} = \frac{20.7 - 10.5}{6.8} = 1.5 \tag{7.13}$$

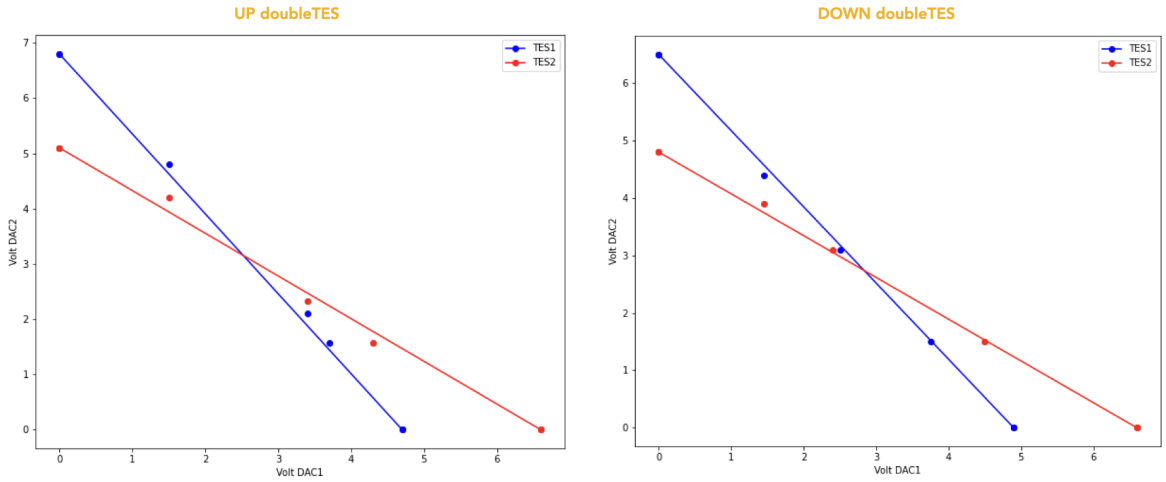

Figure 7.13: Plots of the DAC values needed to optimise TES1 (blue) or TES2 (red) for both of the $CaWO_4$ doubleTES modules. This test ensures the operability of the modules as the lines of the two TES cross each other.

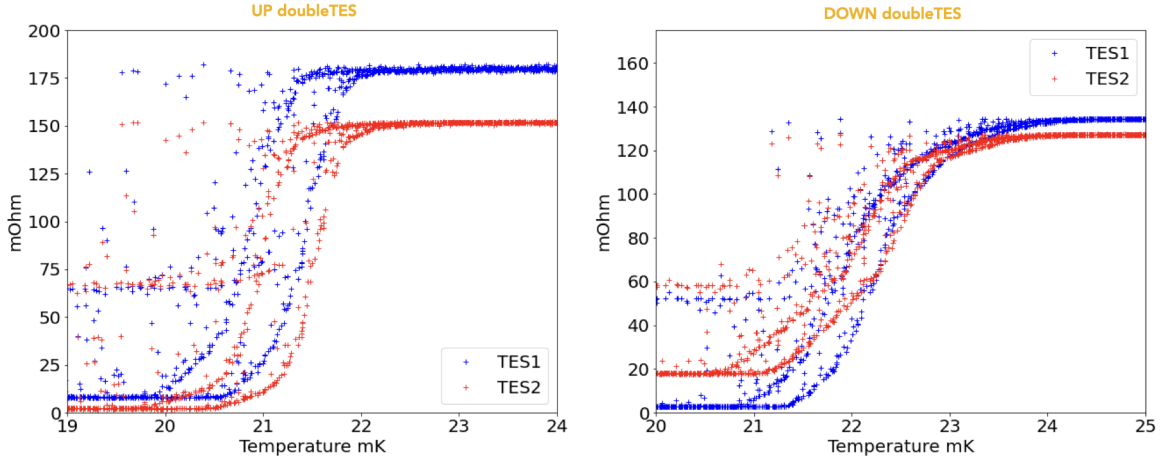

Figure 7.14: Transition curves of TES1 (blue) or TES2 (red) for both of the $CaWO_4$ doubleTES modules. The transitions are recorded during a slow sweep up and down of the mixing chamber temperature. For both modules, the curves of the two TES overlap, showing a very similar transition temperature.

and

$$b \cdot g_{22} = \frac{T_{C,2} - T_{bath}}{DAC2} = \frac{20.9 - 10.5}{5.2} = 2 \tag{7.14}$$

Taking the ratio of these two equations, we obtain one of the two limiting cases:

$$T_{C,1} - T_{bath} = \frac{b \cdot g_{21}}{b \cdot g_{22}} \cdot (T_{C,2} - T_{bath}) = 0.75 \cdot (T_{C,2} - T_{bath}) \tag{7.15}$$

Setting DAC2 = 0, the second limiting case can be found. Following the same steps:

$$b \cdot g_{11} = 2.23 \tag{7.16}$$

and

$$b \cdot g_{12} = 1.59 \tag{7.17}$$

such that

$$T_{C,1} - T_{bath} = 1.40 \cdot (T_{C,2} - T_{bath}) \tag{7.18}$$

Combining all of this information, the two sensors can be simultaneously operated if their transition temperatures satisfy the following relation:

$$-0.25 \cdot (T_{C,2} - T_{bath}) < T_{C,1} - T_{C,2} < 0.40 \cdot (T_{C,2} - T_{bath}) \tag{7.19}$$

Repeating the entire procedure for the down doubleTES module, we obtain its operability condition:

$$-0.26 \cdot (T_{C,2} - T_{bath}) < T_{C,1} - T_{C,2} < 0.35 \cdot (T_{C,2} - T_{bath}) \tag{7.20}$$

The two $CaWO_4$ modules fulfil these criteria for operability.

To further assess the thermal interference between the two sensors of a doubleTES, we performed a second test: stabilising both TES at their operating points and then sending test pulses through one heater element only. This test helps us understand which part of the thermal component of a pulse in one TES is transmitted to the other sensor. The results of these tests are shown in Figure 7.15. From this figure, we observe some thermal interference among the two sensors. This results in the TES not receiving heater pulses from its own heater, to detect a purely thermal pulse, with an amplitude of approximately half of the amplitude detected by the TES directly receiving the heater pulse from its own heater. We have to keep in mind that such an effect persists for every type of pulses and can result in slightly distorted pulse shapes.

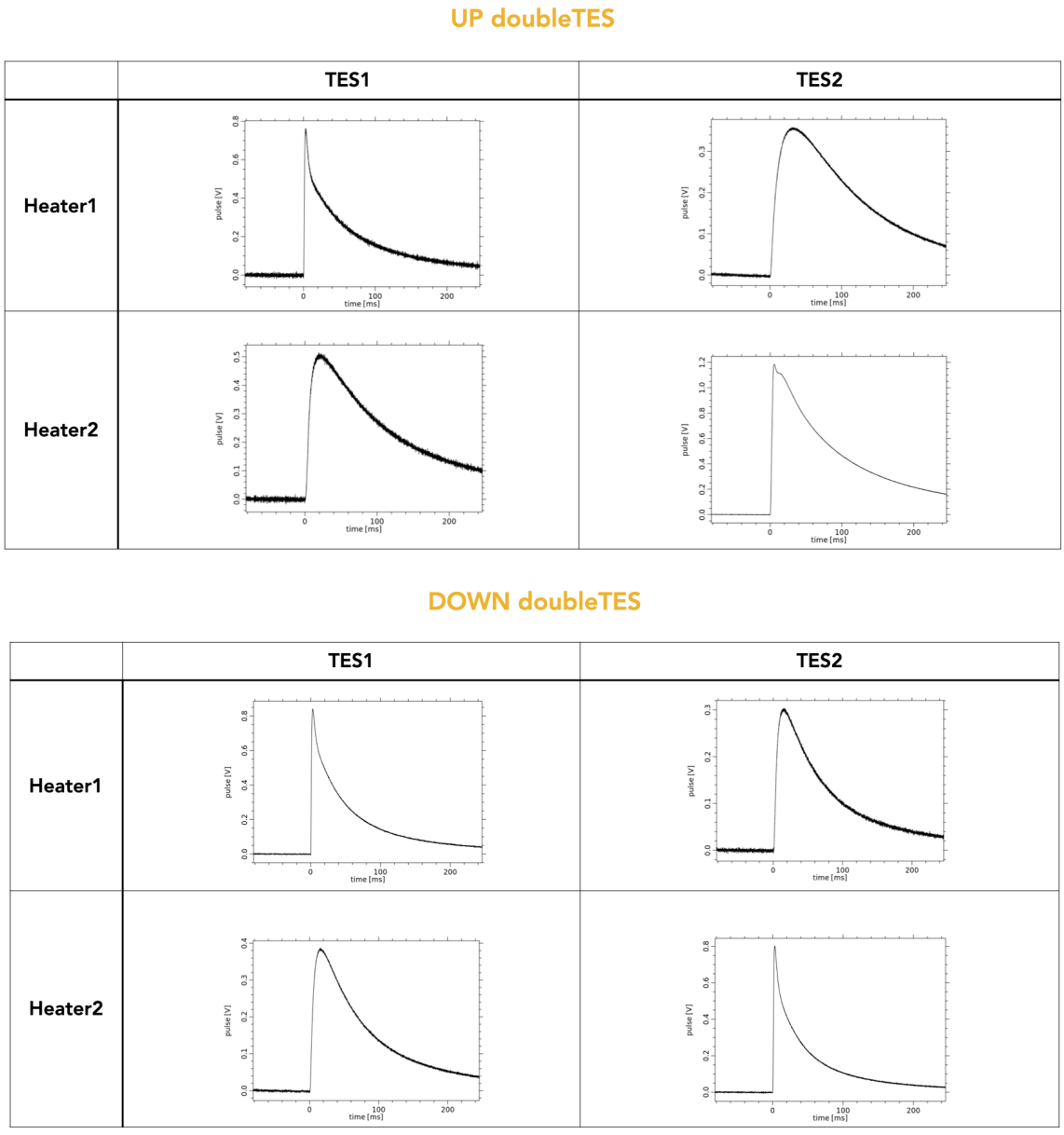

Figure 7.15: *Top:* Picture of the response of the two TES of the up doubleTES to pulses injected through heater 1 and heater 2 only. *Bottom:* Picture of the response of the two TES of the down doubleTES to pulses injected through heater 1 and heater 2 only. In both cases, the part transmitted to the further TES is roughly half of the pulse detected by the TES whose heater is firing the pulses.

7.4.4 Performance Studies and Results

The second part of the experiment focused on studying the performance of the two sensors in the doubleTES setup. This section presents the results from two measurements, providing insights into the behaviour and capabilities of the detectors. Both measurements follow the analysis procedure described in section 7.3.

First Measurement

Both sensors were measured during the first run. The results from both modules were consistent, but the down doubleTES module demonstrated better performance. Therefore, only the results from this module will be detailed in this section.

Down DoubleTES Module A total of 62 hours of measurements were collected. However, due to the challenges of maintaining a stable operating point in the above-ground environment and the large crystal size, only about 20 hours of usable data remained after applying the working point cut.
The two TES of this module will be referred to as "down-TES1" and "down-TES2". The NPS, template pulses and OF of these sensors are shown in Figure 7.16. The absence of an anti-aliasing filter introduced noise issues. The anti-aliasing filter functions essentially as a low-pass filter, attenuating noise components with frequencies above half of the sampling frequency. Without it, high-frequency noises appear at lower frequencies, due to a phenomenon known as aliasing.
Despite this, the sensors achieved baseline resolutions of 27.1 eV and 29.6 eV, respectively, resulting in computed energy thresholds of 137 eV for down-TES1 and 148 eV for down-TES2.
Calibration was performed as described in section 7.3.6, with a check of the sensors' response linearity (see Figure 7.17). The energy thresholds obtained in this measurement are too high to study the full low energy excess spectrum. Nevertheless, this measurement serves as a proof-of-principle of the detector's working principle.
The energy resolutions at 5.89 keV are 117 eV for down-TES1 and 128 eV for down-TES2. Figure 7.18 shows the double Gaussian fit of the K_α and K_β for down-TES1.

Following the performance studies of the individual TES, we conducted a combined analysis of the two sensors to investigate the possibility of locating the origin of the events. Using data from the measurement, we reproduce the plot schematised in Figure 7.4. The resulting plot, shown in Figure 7.19, reveals distinct populations, colour-coded for easier visualisation. Events triggering both channels are represented in blue, those triggering in down-TES1 only are in red, and those triggering in down-TES2 are in green.

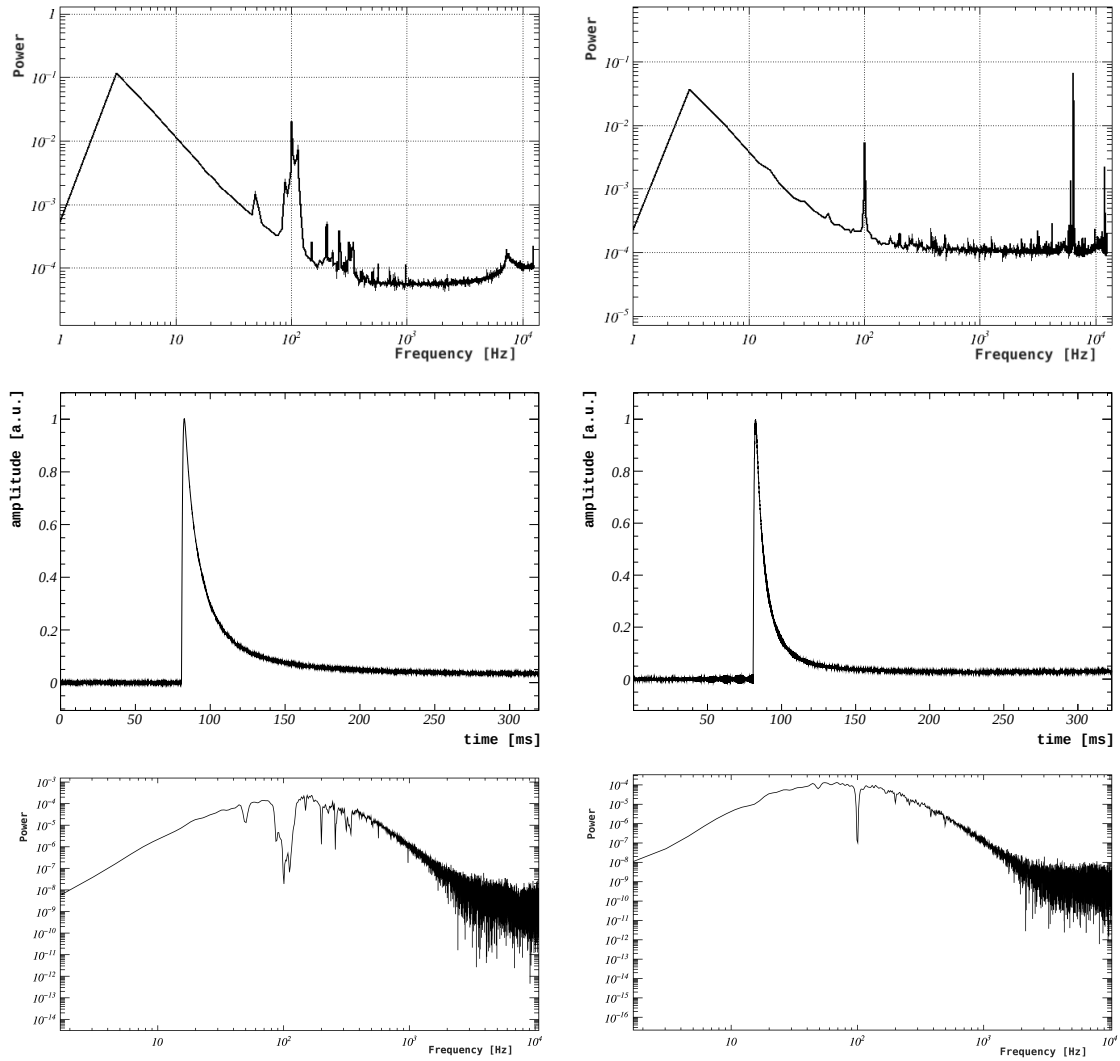

Figure 7.16: Plot of the noise power spectra, template pulses and optimum filter kernels of down-TES1 (*left*) and down-TES2 (*right*)

Interestingly, more events trigger down-TES2 than down-TES1, with energies reaching almost 2 keV, significantly higher than the known LEE energies. This difference led us to investigate the cause of these events.

Upon inspecting the events (see Figure 7.20), we observed differences in pulse shape compared to the template pulse. To explore the possibility of electronic bursts causing these events, we examined their time distribution. Figure 7.21 shows that these events have the same time distribution as valid particle events, thus excluding the hypothesis

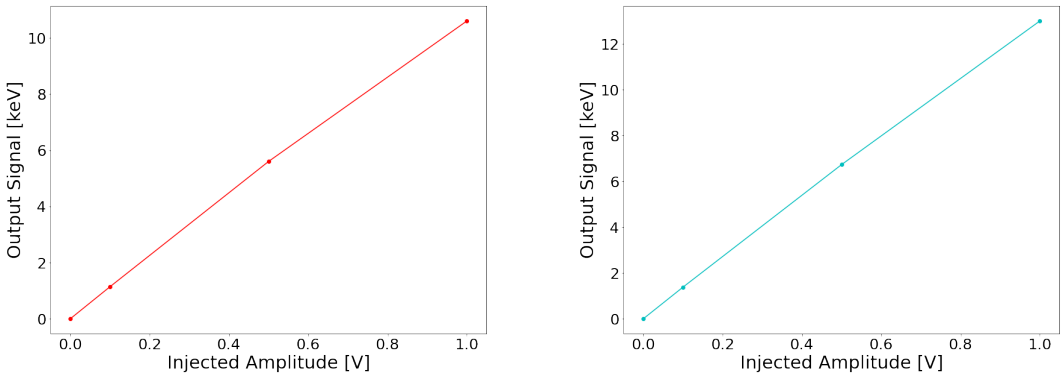

Figure 7.17: Plot of the output signal of down-TES1 (*left*) and down-TES2 (*right*) to test pulses as a function of the injected amplitude. Both of the sensors appear to be linear up to almost 1V. The 5.89 keV peak from the iron sources outputs a signal of roughly 0.45 V in both sensors, thus being in the linear region of the energy dynamic range.

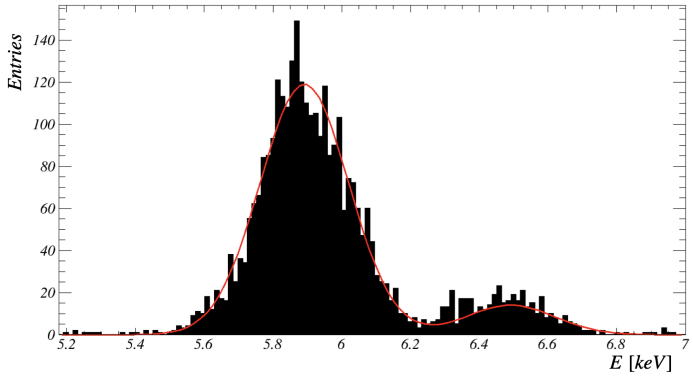

Figure 7.18: Fit of a double Gaussian to the two peaks of the x-rays coming from the iron calibration source for down-TES1. The σ of this fit corresponds to the energy resolution of the sensor at 5.89 keV.

of bursts.

Notably, despite the difference in shape, we cannot distinguish these events from real particle interactions in the absorber crystal using information from the filter RMS. Conversely, analysing the PeakRMS distribution (shown in Figure 7.22) enabled us to isolate these events. Nonetheless, as explained in section 7.3, this cut carries a strong risk of energy dependency.

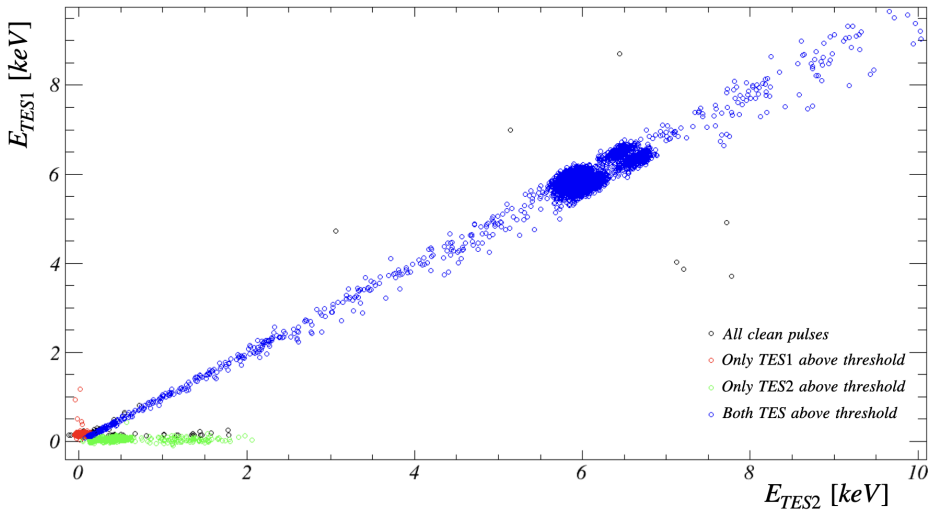

Figure 7.19: 2D energy spectrum of the down doubleTES. On the x-axis is the energy of down-TES2, while on the y-axis is the energy of down-TES1. The different colours represent different populations: in black, all the pulses surviving the quality cuts; in red, the events where only down-TES1 triggered; in green, the events where only down-TES2 triggered; and in blue, the events where both channels triggered. The green population extends to much higher energies than the red one. This issue is discussed in the text.

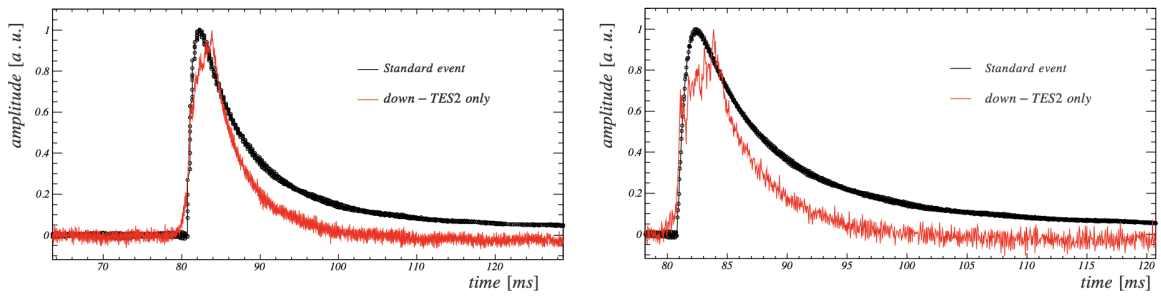

Figure 7.20: Events with energies around 1 keV in down-TES2 only compared to the template pulse of down-TES2. The difference in pulse shape is visible.

Given the proof-of-principle nature of this measurement, aimed at studying the combined analysis of the two TES at energies close to threshold, the presence of artificial pulses could potentially alter the results. Therefore, we applied the PeakRMS cut in this measurement. Figure 7.23 presents the resulting 2D histogram with the energies of the two TES as axes after applying this cut.

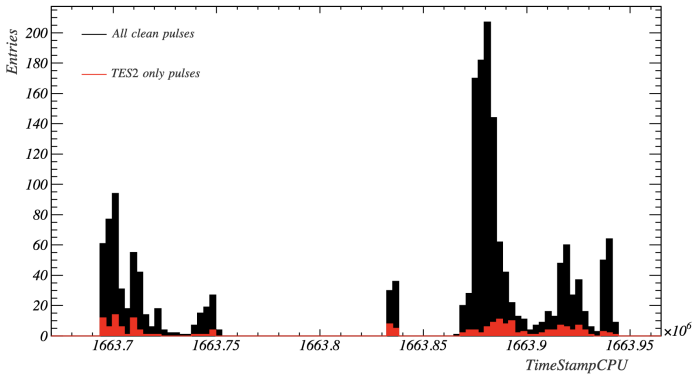

Figure 7.21: Time distribution of the high energetic events in down-TES2 only compared with the time distribution of clean pulses. The two distributions have the same behaviour, highlighting that these events do not come in bursts. The non uniformity of the distribution derives from the different run being recorded at different times, and by the presence of instabilities.

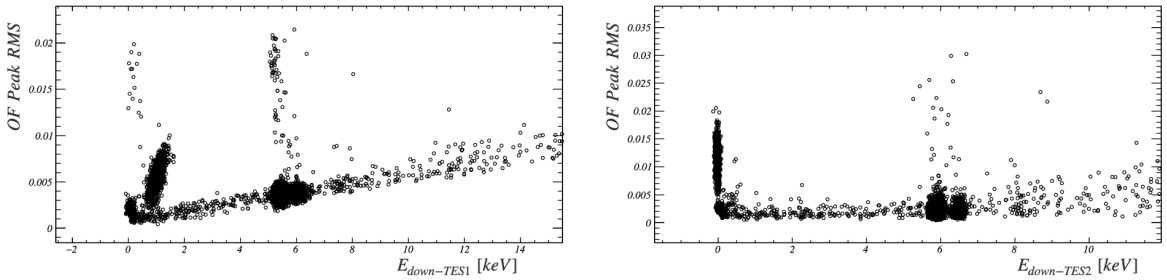

Figure 7.22: *Left:* OF Peak RMS distribution for down-TES1. *Right:* OF Peak RMS distribution for down-TES2. Both plots show a clear separation between the band of coincident events and a separated population of events, formed by pulses with energies around 1 keV in down-TES2 only.

Looking at the diagonal band, we can distinguish two separate iron populations, each exhibiting two peaks. These populations correspond to the two ^{55}Fe sources. The TES closer to the ^{55}Fe source measures at most 5% more energy than the further away TES, suggesting only a slight position dependence in the detector's response.
The presence of this separation (despite its small magnitude) implies that a more precise energy estimate can be achieved by averaging the signal from both sensors. The resulting energy spectrum is shown in Figure 7.24. The energy resolution at 5.89 keV is 81 eV.

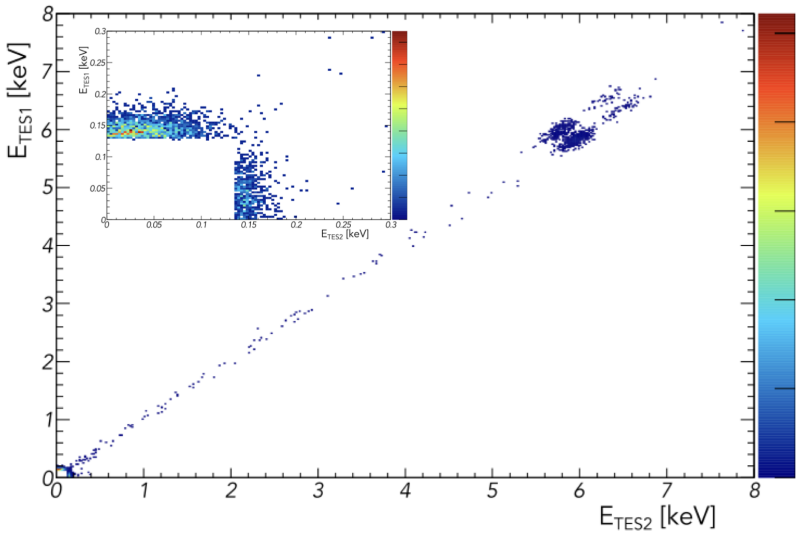

Figure 7.23: 2D histogram with the energies of the two TES as axes after the PeakRMS cut. The inset shows a zoom into lower energies, from threshold up to 300 eV.

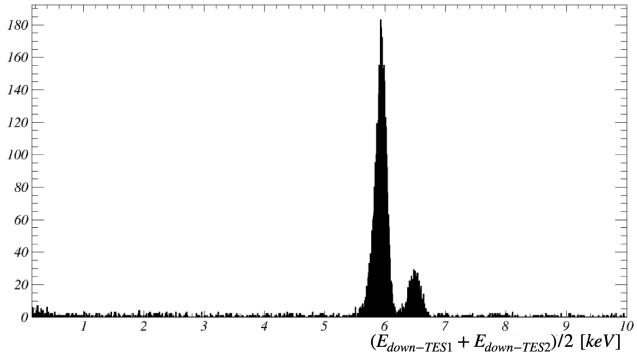

Figure 7.24: Energy spectrum of the average signal from the two TES. The two peaks of the X-rays emitted by the iron calibration source are well separated, and the energy resolution at 5.89 keV is 81 eV.

The last step of this analysis consists of implementing the absorber events cut. To design this cut, we examine Figure 7.25. To accept an event as an absorber event, we conservatively require that the energies measured by the two sensors should not differ by more than 35%. This cut can be visualised in the 2D energy spectrum, as shown in Figure 7.26.

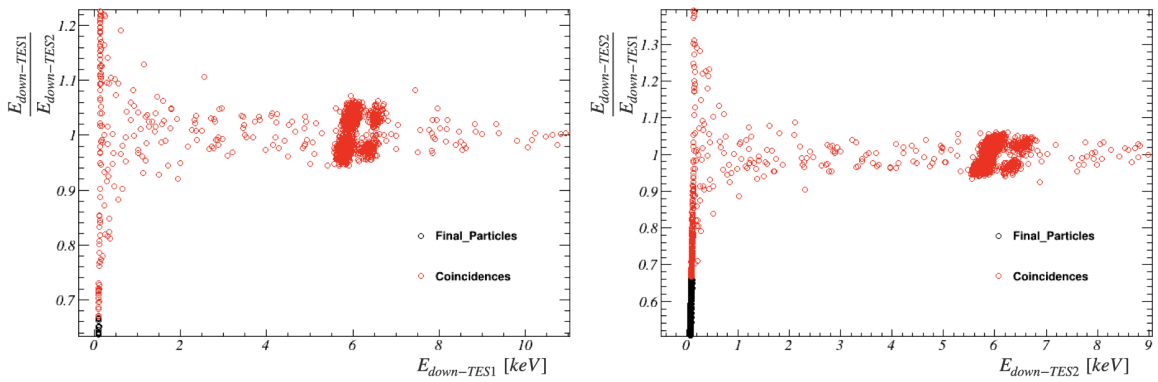

Figure 7.25: Implementation of the absorber events cut for the first measurement of down-TES1 (*right*) and down-TES2 (*left*). The accepted events are shown in red. We accept events in which the energies measured in coincidence by the two sensors do not differ more than 35%.

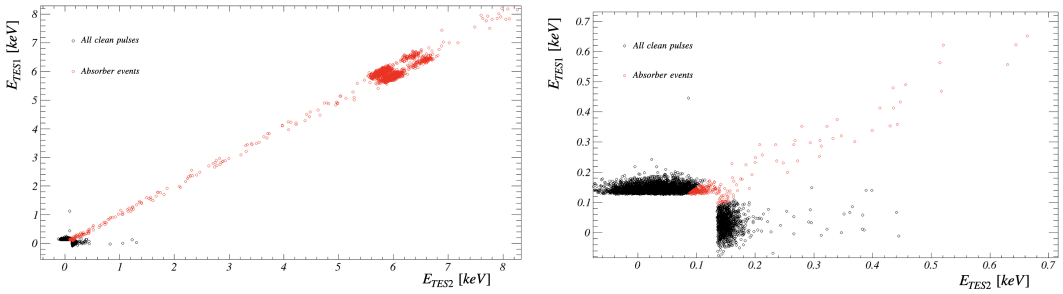

Figure 7.26: Absorber events cut visualised in the 2D energy spectrum. The red events are those accepted by the cut. None of the events in the diagonal band is rejected. *Right:* Zoom into the lower energy region of the spectrum, from threshold up to 700 eV.

To ensure that the single TES events are actual particle-like events and not noise triggers, we generated standard events using the pulses in this region, as shown in Figure 7.27. Despite the tilted baseline caused by unfavourable noise conditions and the small amplitude of the single TES events, the comparison indicates similarities between the pulse shapes.
To further confirm the particle-like nature of the observed singleTES events, we studied the noise distributions of the two TES in the voltage-inverted data stream, following the procedure detailed in [88]. The results of this study for down-TES1 are shown in

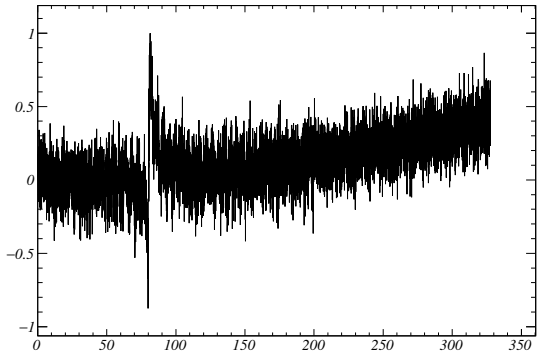

Figure 7.27: Standard event computed from the low energy events in down-TES2 only.

Figure 7.28. The plot on the left shows the noise distribution of down-TES1, obtained by applying the OF to the inverted data stream, while the plot on the right shows the spectrum of down-TES1 close to its trigger threshold. The events appearing below the threshold of the detectors are pulses which triggered in down-TES2 only. Looking at these plots, the events triggering in down-TES2 but not in down-TES1 appear to provide a good estimation of the noise distribution in down-TES1, and we ultimately rule out misidentified noise as a possible origin for the events observed close to the sensors' thresholds.

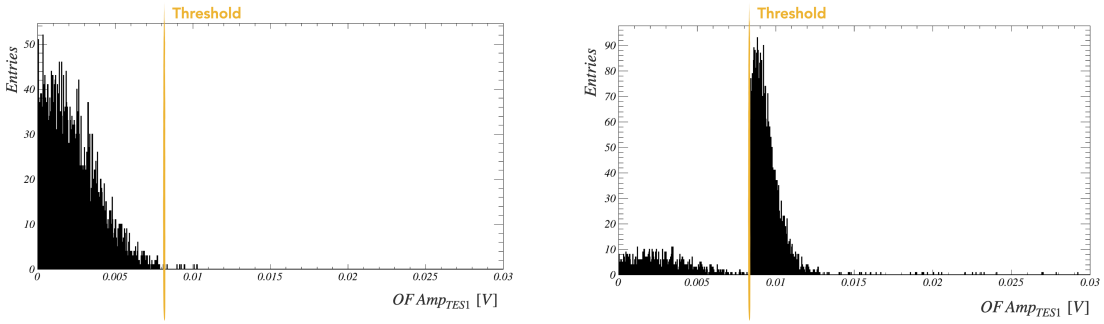

Figure 7.28: *Left:* Non-calibrated noise distribution of down-TES1, calculated by applying the OF to the inverted data stream. *Right:* Non-calibrated spectrum of down-TES1 close to threshold. The population of events below threshold is composed of particle events triggering in down-TES2 only. The rise of events at threshold is not attributable to noise.

To assess the impact of the absorber events cut at energies close to threshold, we

examined the 1D spectra of the two sensors at low energies before and after the absorber events cut (see Figure 7.29). The cut effectively reduces the number of events observed near the threshold during the above-ground test of this module.

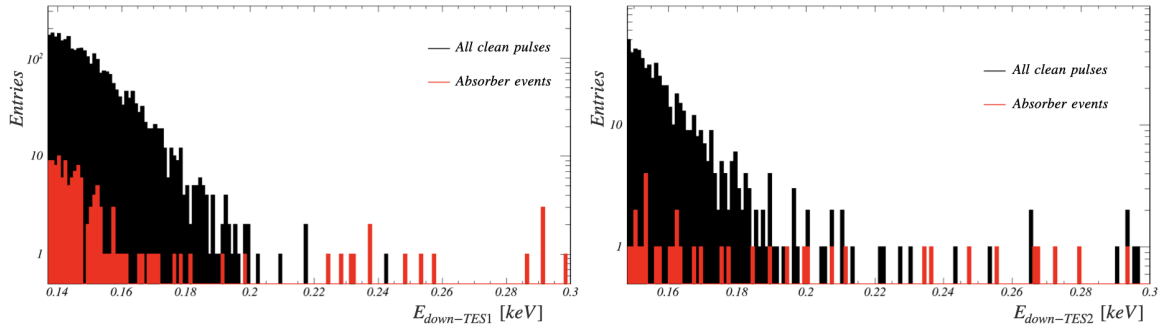

Figure 7.29: Energy spectra of the two TES close to threshold. In black are the spectra of the two TES after quality cuts, and in red are the spectra after the quality cuts + absorber events cut.

As discussed in section 7.3.8, it is crucial to evaluate the efficiency of the cut to ensure that it is conservative and it does not exclude events originating in the bulk of the crystal. Thus, we performed a simulation to study its impact. Figure 7.30 shows the calculated survival trigger efficiency of 45% and survival probability of approximately 12%.
Since we can observe that the absorber events cut slightly reduces the survival probability at low energies in this measurement, we correct the 1D spectra for the computed survival probability. The resulting spectra are shown in Figure 7.31.

To enhance the trigger efficiency for absorber events, particularly at low energies, we explored the possibility of summing the data stream from the two TES and triggering on the combined stream. In this way, the single TES events should be disfavoured with respect to the absorber events during the triggering, and this should improve our sensitivity to dark matter. Indeed, all of the energy deposits causing a signal in both TES would result in double the size in the summed stream. Despite this modification, the results remained qualitatively unchanged.

Although the energy thresholds of these sensors are high, thus precluding the possibility of drawing conclusions about the observed LEE; we can confirm the observation of events where energy is deposited in one of the two sensors only. These events might be intrinsic to the sensors and thus pose calibration challenges due to their response being notably different from the response to energy deposition in the absorber.

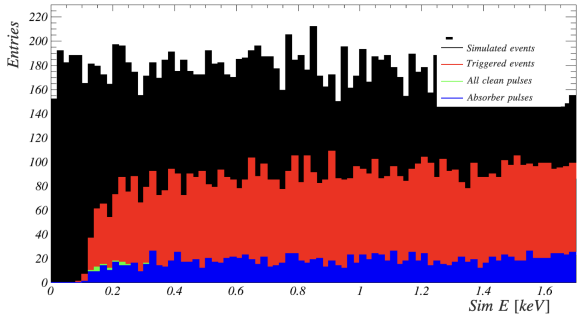

Figure 7.30: Plot of the efficiencies of the first measurement. The trigger efficiency is computed considering events that trigger in at least one channel. The quality cuts are applied to both channels simultaneously: a pulse must be accepted in both channels to be considered a good pulse. We obtain a trigger efficiency of 45% (shown in red) and a signal survival probability of 12% (shown in green for quality cuts and in blue for quality cuts+absorber events cut).

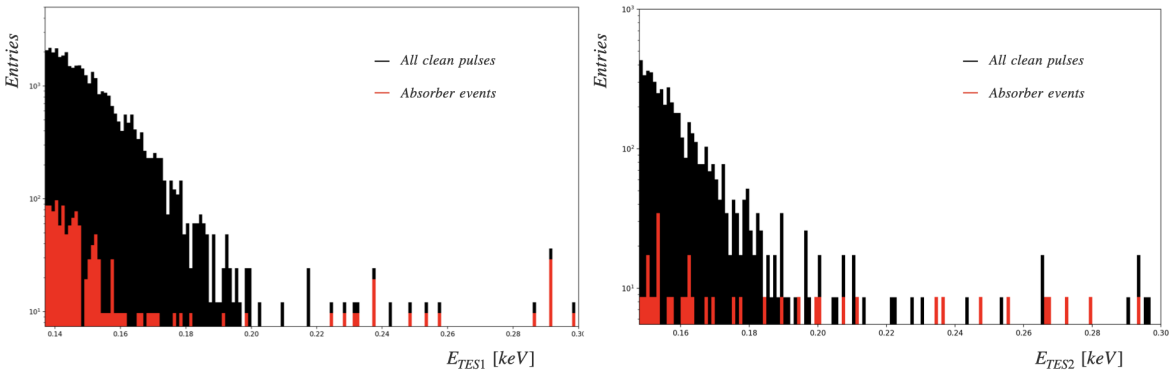

Figure 7.31: Energy spectra of the two TES close to threshold. In black are the spectra of the two TES after quality cuts, and in red are the spectra after the quality cuts + absorber events cut. Each spectrum is corrected for the corresponding signal survival probability shown in Figure 7.30.

Second Measurement Results

This second measurement was conducted to understand the origin of the events observed solely in down-TES2 during the first measurement.
To try to locate their origin, we interchanged the readout channels as follows:

First Meas.		Second Meas.
down-TES1	→	up-TES2
down-TES2	→	up-TES1
up-TES1	→	down-TES2
up-TES2	→	down-TES1

This exchange aimed not only to trace the source of the discrepancy but also to investigate if the difference in performance between the two modules was linked to specific noise conditions in the readout channels.
Additionally, one of the two iron sources from each of the crystals was removed for this run. This adjustment sought to enhance the understanding of the position dependence and to cross-check that the observed iron populations in the first measurements stemmed from the two different sources rather than from other effects (e.g. position dependence-related effects).

Both sensors were again measured in this run, yielding compatible results. For performance evaluation, only the results of the up doubleTES module will be presented in this section.

Up DoubleTES Module A total of 64 hours of measurement were collected for this module. However, due to instabilities, only approximately 30 hours of usable data remained after the working point cut.
The NPS and template pulses of these sensors are shown in Figure 7.32.
Notably, the template of up-TES1 exhibits severe noise conditions, probably worsened by the absence of an antialiasing filter, as for the previous measurement. A parametric fit of this template was performed using the pulse thermal model (see section 4.2), to obtain a noise free template, preserving the signal shape. Anyways, this noise significantly affects the performance and, in particular, the baseline resolution of this TES.
The two TES achieved baseline resolutions of 61.2 eV and 32.2 eV, respectively. The thresholds are computed with the assumption of 1% of the triggers being noise triggers, as described in section 7.3.3 and they are 221 eV for up-TES1 and 131 eV for up-TES2 (see Figure 7.33). These values are lower than those computed as $5\,\sigma_{BL}$ due to the unfavourable noise affecting the baseline resolution.
The linearity in the response of the sensors up to the energy of the iron peaks was verified, and it is shown in Figure 7.34.

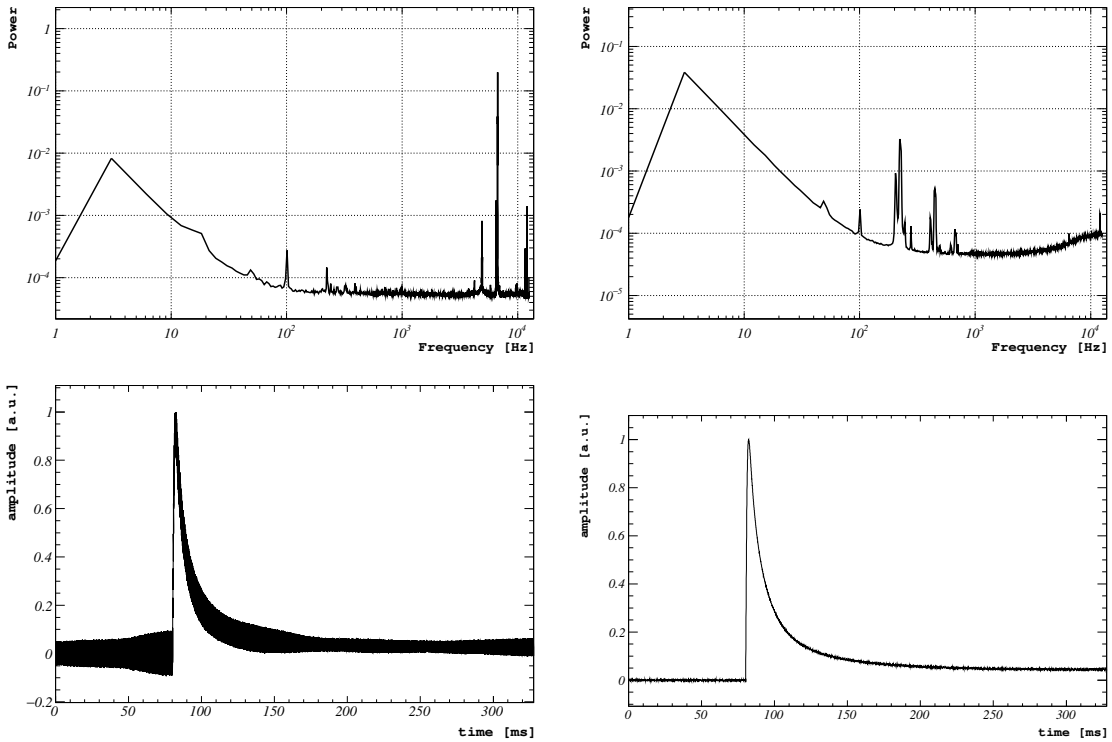

Figure 7.32: Plot of the noise power spectra, template pulses and optimum filter kernels of up-TES1 (*left*) and up-TES2 (*right*)

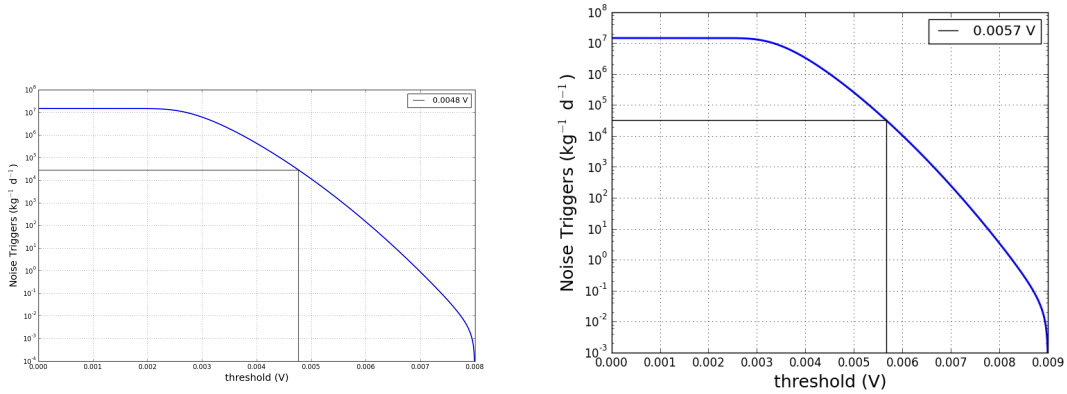

Figure 7.33: Plot of threshold computation for up-TES1 (*left*) and up-TES2 (*right*)

The energy resolutions at 5.89 keV of the two sensors are computed to be 129 eV for up-TES1 and 80.5 eV for up-TES2 (see Figure 7.35). Since this measurement only

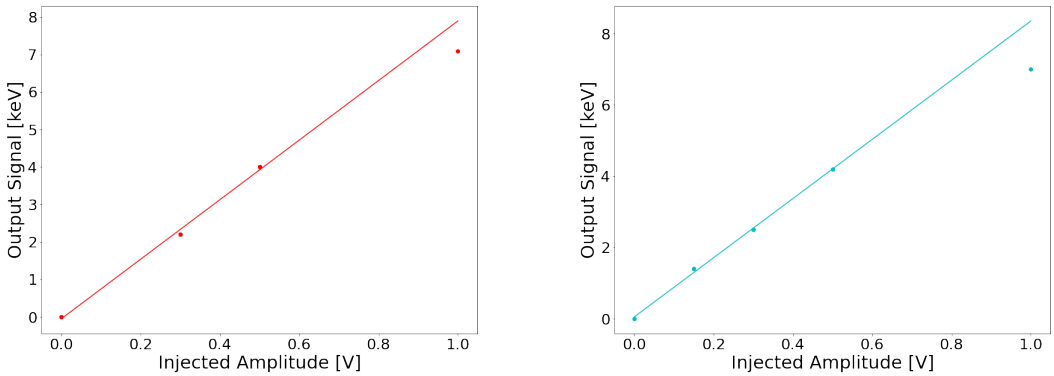

Figure 7.34: Plot of the output signal of up-TES1 (*left*) and up-TES2 (*right*) to test pulses as a function of the injected amplitude. Both of the sensors appear to be linear up to almost 0.6V. The 5.89 keV peak from the iron sources outputs a signal below 0.3 V in both sensors, thus being in the linear region of the energy dynamic range.

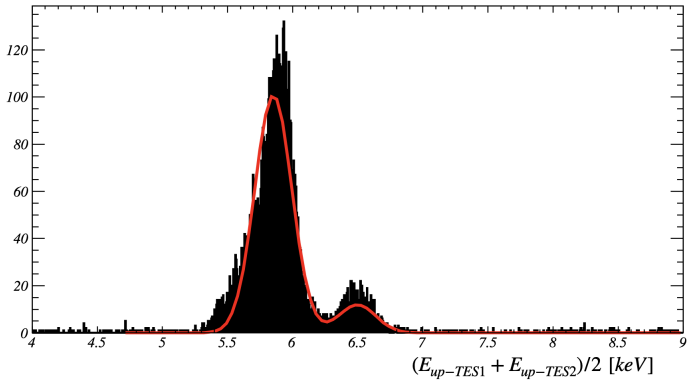

Figure 7.35: Fit of a double Gaussian to the two peaks of the x-rays coming from the iron calibration source for the average of up-TES1 and up-TES2. The σ of this fit is computed to be 105 eV.

features a single iron source, the energy resolution of the TES located further from the source was adversely affected, due to the slight position dependence also observed in the previous measurement. As discussed for the results of the first measurement, averaging the output of the two sensors should provide a more accurate estimate of the energy resolution of the module as a whole. Consequently, the overall energy resolution at 5.89 keV peak for this module is 105 eV (refer to Figure 7.35).

This measurement aimed at understanding the origin of the high energetic events

detected by down-TES2 only during the previous measurement. Initially, data were collected to test the hypothesis that these events originated from electronics.
Analysing Figure 7.36, the hypothesis that these events stem from the electronics appears plausible, as the affected channel uses the same readout channel as the channel affected by this problem in the first measurement. Further disentangling of the various components allowed us to identify the specific cause of these electronic events in the test pulse electronics board. Subsequently, by replacing this board with a properly working one, we successfully removed these events.

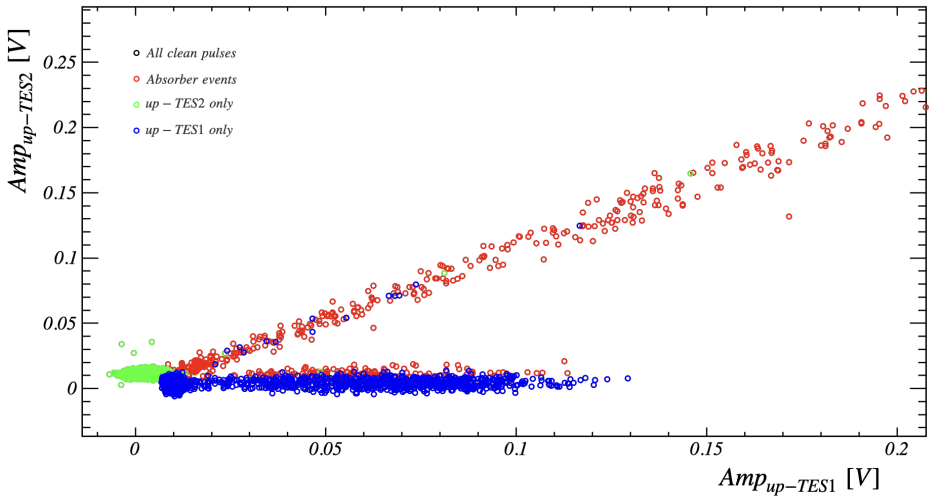

Figure 7.36: 2D spectrum with the amplitudes of the two TES in volts in the x and y-axis. Detector up-TES1 clearly shows the same abundance of events with energies around 1 keV shown by down-TES2 in the previous measurement.

We conducted a combined analysis of the two sensors with the electronics issue resolved. Examining the 2D energy spectrum in Figure 7.37, we observed a result similar to the previous measurement: three different populations of events were discernible. Additionally, we confirmed that the double structure of the iron peak observed in the first measurement was attributable to the presence of two ^{55}Fe sources. In the current plot, only one structure is observed, with the two peaks at 5.89 keV and 6.49 keV well separated.

Given the noise levels during this measurement, it is crucial to verify whether the events observed by the single sensors at the threshold are genuine particle-like events or noise triggers. Studies of the standard events from different regions of the spectrum showed that single TES events are not merely noise triggers, but valid events. Figure 7.38 shows the standard event from up-TES1 only, confirming the presence of a valid

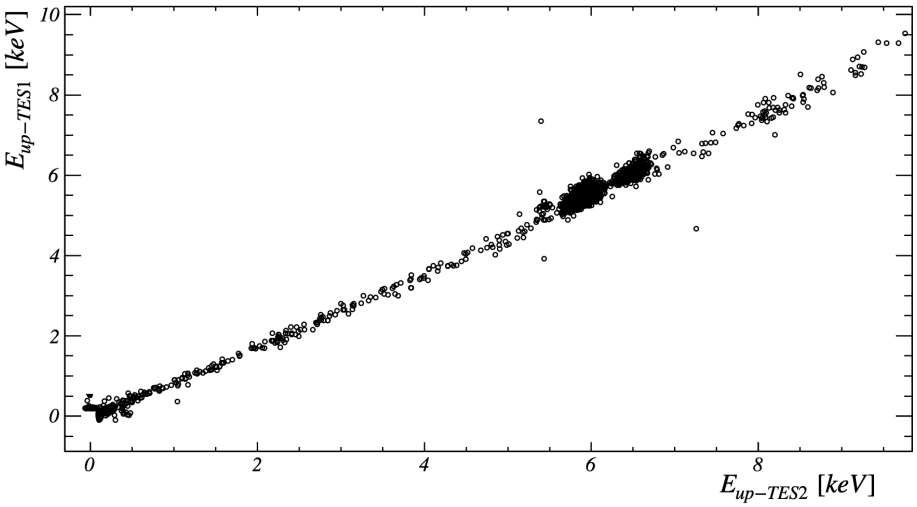

Figure 7.37: 2D energy spectrum of the up doubleTES detector during the second measurement.

pulse, despite the adverse noise conditions.

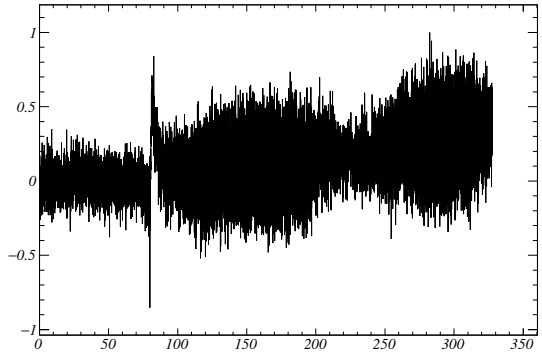

Figure 7.38: Standard event computed from the low energy events in up-TES1 only.

Next, we designed the absorber events cut based on the energy ratio between the two sensors (see Figure 7.39). Events where the energy detected by the two TES differs by more than 35% are rejected.

This cut effectively reduced the number of events at threshold, as evidenced by the 1D energy spectrum of up-TES2 before and after the cut (see Figure 7.40). Furthermore, the overall survival probability remained low (approximately 16%), but it did

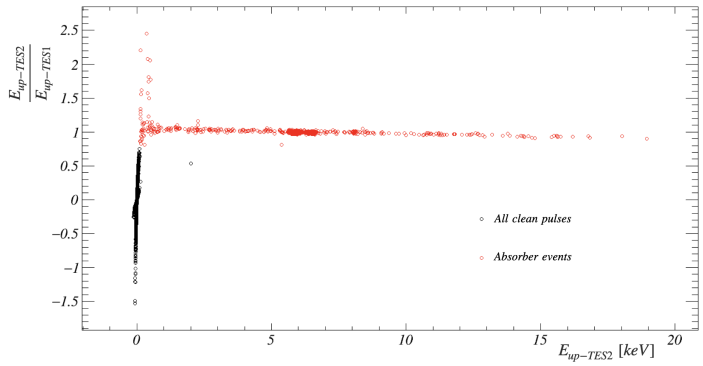

Figure 7.39: Plot of the ratio between the energy detected by up-TES2 and the energy detected by up-TES1 as a function of the energy detected by up-TES2. The absorber event cut is designed on this distribution, accepting only events in which the two TES observe a signal which does not differ by more than 35%.

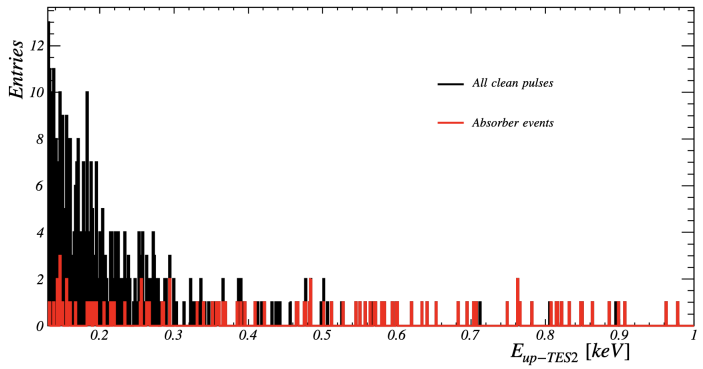

Figure 7.40: Energy spectrum of up-TES2 before and after the absorber events cut. The events in red are the events surviving the absorber events cut.

not appear to be affected by the absorber events cut.
Interestingly, events observed by only one of the sensors are again detected, occurring near the detectors' threshold. This observation reinforces the findings from the previous measurement.

Finally, the analysis of this dataset for the up doubleTES detector was repeated using the different triggering algorithm previously described and yielded consistent results, validating the robustness of the findings.

7.4.5 Conclusions

In summary, the two measurements with two doubleTES $CaWO_4$ crystals demonstrated very promising performance, and we anticipate significant improvements when these crystals are tested in the CRESST underground facility.
Across both measurements, we consistently observed events present in only one of the two TES, appearing at the energy threshold of the sensors. This intriguing observation supports further investigation and highlights the importance of continued research in this area.

7.5 Silicon-on-sapphire doubleTES

The silicon-on-sapphire (SOS) doubleTES detector represents the second prototype for this detector layout.

7.5.1 Design and Motivation

This detector, consisting of a $20\times20\times0.4\,\mathrm{mm}^3$ silicon-on-sapphire crystal, was produced to address the challenge of high rates encountered with the $CaWO_4$ crystals. The reduced dimensions of the SOS crystal offer several advantages, including access to lower energies [84] and pile-up reduction. A picture of this detector mounted for its above-ground test can be found in Figure 7.41.

Two SOS doubleTES crystals were initially produced and stacked on each other. However, operational issues arose due to significant differences in the thermal properties of the two sensors in one of the detector, preventing simultaneous operation. Consequently, only one detector was operated, and its results will be presented in the following.

The W-TES used in this detector has the standard light detector TES dimensions, featuring a single-layer realisation. The heaters are directly deposited on top of the tungsten, as for the $CaWO_4$ detector, and insulated through a 350 nm layer of SiO_2.

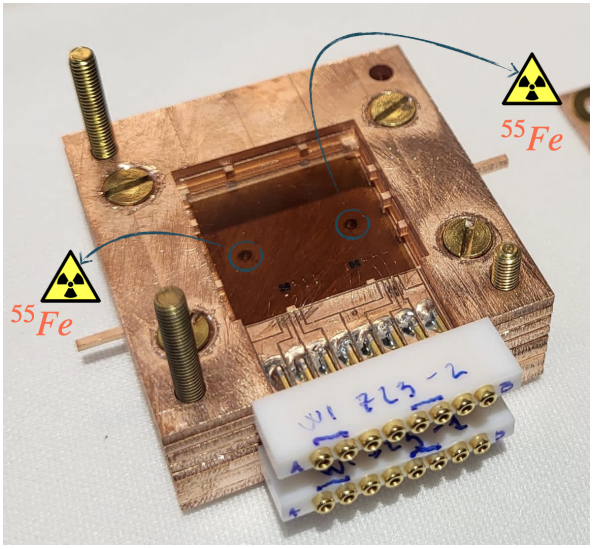

Figure 7.41: Photo of the silicon-on-sapphire doubleTES detector, mounted for its first above-ground test. The two ^{55}Fe sources are highlighted.

7.5.2 Experimental set-up

The above-ground testing of the SOS doubleTES prototype was conducted in the above-ground facility of the MPP, utilising Cryo 1, an Oxford Instruments Kelvinox100 dilution refrigerator. This cryostat is housed within a Faraday cage and is equipped with two StarCryo SQUIDs quads and 2 APS-581 SQUIDs for a total of 10 readout channels. Temperature measurements are performed through a thermometer mounted directly on the detector plate.
The same data acquisition system employed for the previous measurements was used. The detector was measured in its gravity-assisted holder, directly screwed onto the detector plate, without the use of any additional decoupling system.

7.5.3 Test Results

A total of 125 hours of measurements were collected during this run. After the working point cut, roughly 75 hours of usable data remained. This is a much higher fraction of events compared to the larger $CaWO_4$ crystal previously presented, achievable thanks to the lower rate of events facilitating stable operations.
The two sensors of this detector are referred to as TES1-L and TES2-L, and the analysis follows the procedure described in section 7.3.
The NPS, template pulses and OF of these two sensors are shown in Figure 7.42 The two sensors achieved the outstanding baseline resolution of 5.4 eV and 4.1 eV respectively. We set the energy threshold to $5\,\sigma_{BL}$ for this measurement, corresponding to

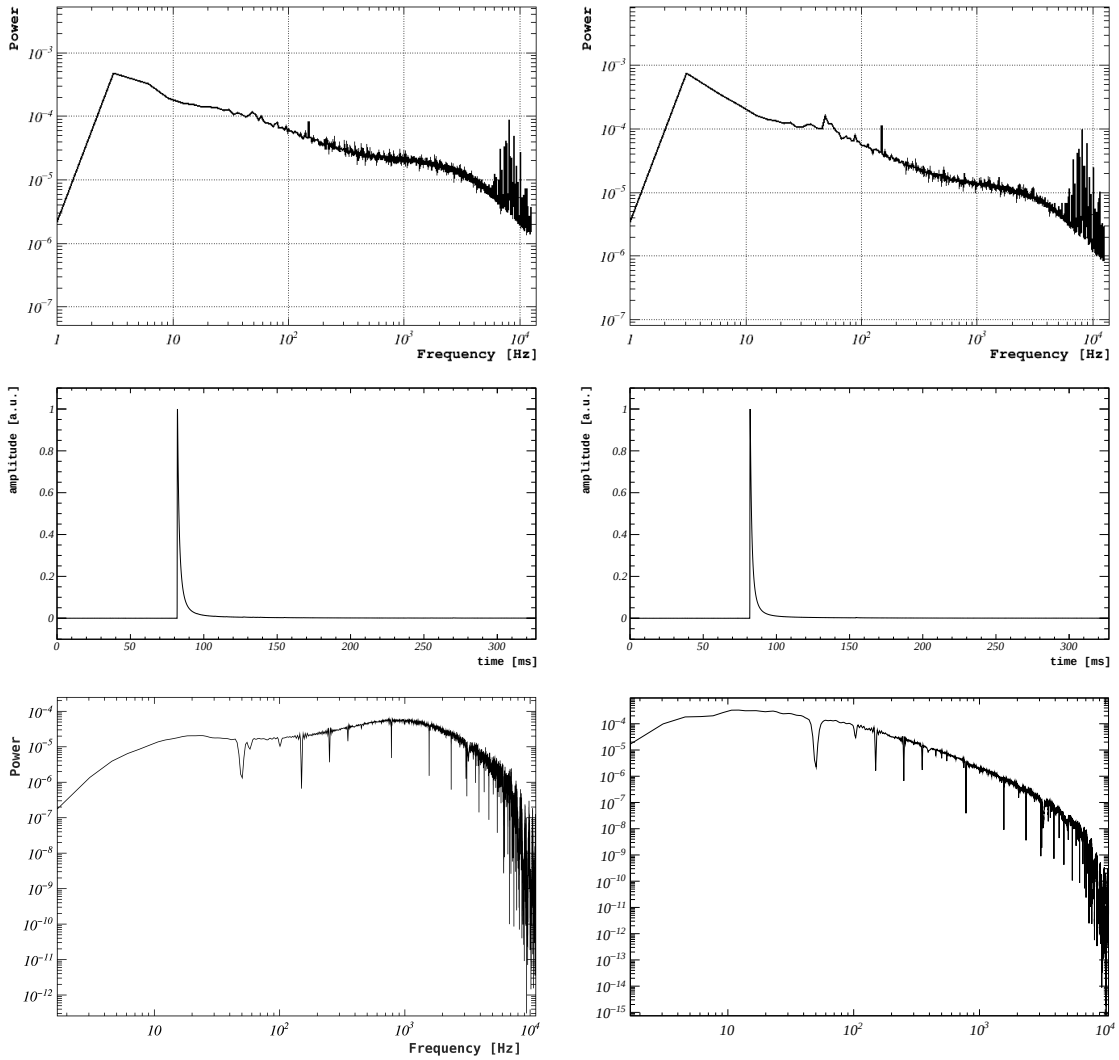

Figure 7.42: Plot of the noise power spectra, template pulses and optimum filter kernels of TES1-L (*left*) and TES2-L (*right*)

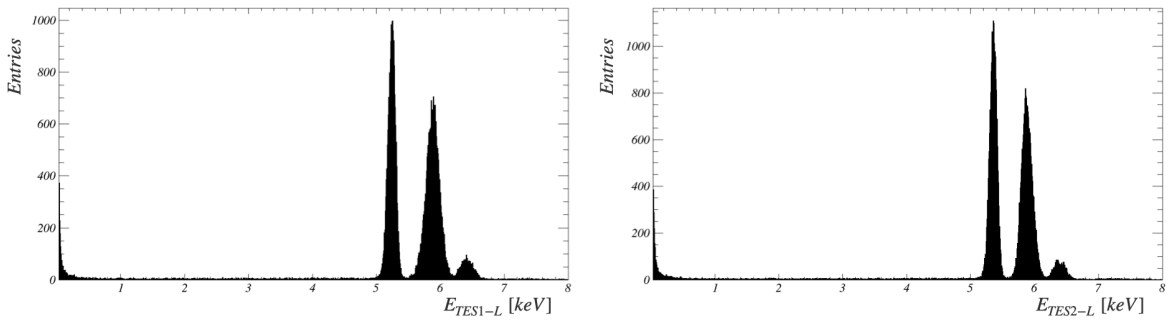

Figure 7.43: Energy spectra of TES1-L (*left*) and TES2-L (*right*). Both spectra show three peaks around the energy of the X-rays emitted by the iron source. From the left, the first peak corresponds to the 5.89 keV peak from the furthest source; the second peak is a superimposition of the 5.89 keV peak from the nearby source with the 6.49 keV peak from the one furthest away, the third peak is the 6.49 keV peak from the source nearby.

a threshold of 27 eV for TES1-L and 20.5 eV for TES2-L. The energy resolutions at 5.89 keV were computed as 149 eV for TES1-L and 121.6 eV for TES2-L. The peaks from the two different sources are well-separated in the energy spectra, as shown in Figure 7.43. However, the 6.49 keV peak of the furthest source is superimposed to the 5.89 keV peak of the closest source worsening the energy resolution.
As discussed in section 7.4, averaging the response of two signals we obtain the spectrum in Figure 7.44 and an energy resolution at 5.89 keV of 90 eV. The linearity of the

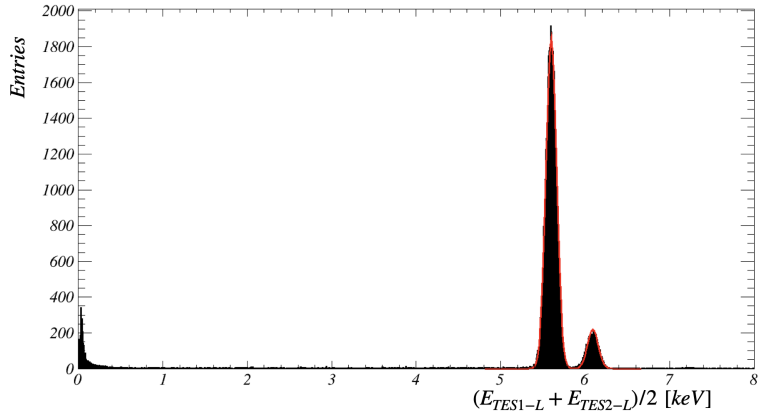

Figure 7.44: Energy spectrum of the average of TES1-L and TES2-L. The two peaks of the iron are well separated. The double Gaussian fit to the iron peaks is shown with a red line and its σ is 90 eV.

sensor response up to the iron peaks was confirmed and further validated the calibration process, ensuring the accuracy of energy measurements.

The combined analysis of the two sensors revealed interesting findings. Figure 7.45 shows the 2D energy spectrum of this module before implementing the absorber events cut, showing different populations corresponding to events where both TES triggered, events where only TES1-L triggered, and events where only TES2-L triggered. The position dependence is visible from this plot, particularly when looking at the iron peaks. For both peaks, the TES closer to the ^{55}Fe source measures up to 15% more energy than the further one. This stronger position dependence is expected for such a thin crystal and should be carefully accounted for, especially when designing the absorber events cut.

Figure 7.46 shows the absorber cut implemented in this measurement, designed to

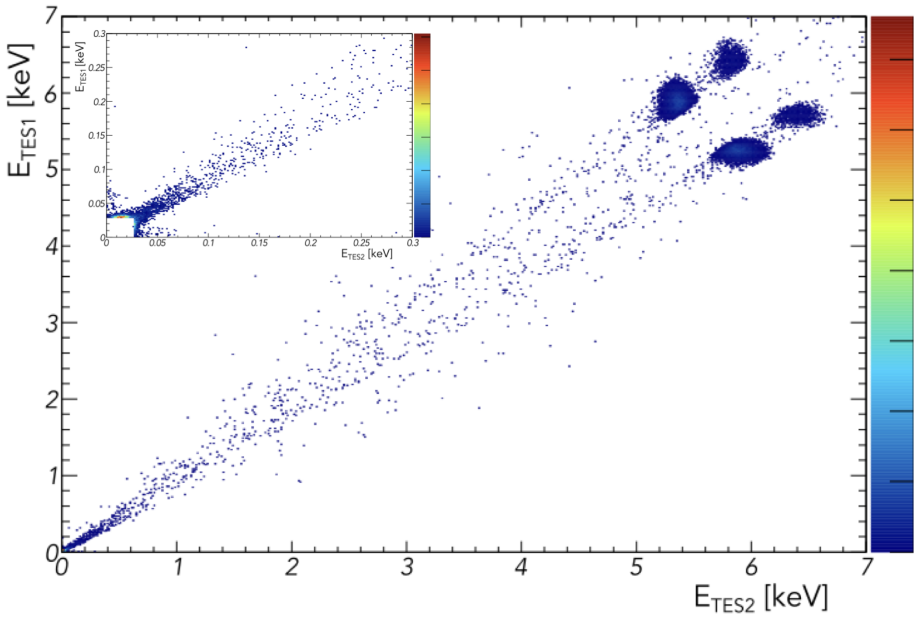

Figure 7.45: 2D histogram with the energies of the two TES of the SOS doubleTES detector as axes. The inset provides a zoom into lower energies of the spectrum, from threshold up to 300 eV.

accept events where the energy detected by the two sensors does not differ more than 50% are accepted.

We can also visualise this cut in the 2D energy spectrum, zooming into the energy region below 500 eV, as shown in Figure 7.47. To help in visualising this cut, Figure 7.48 presents a zoom into energies below 100 eV of the 2D histogram presented in Figure 7.45.

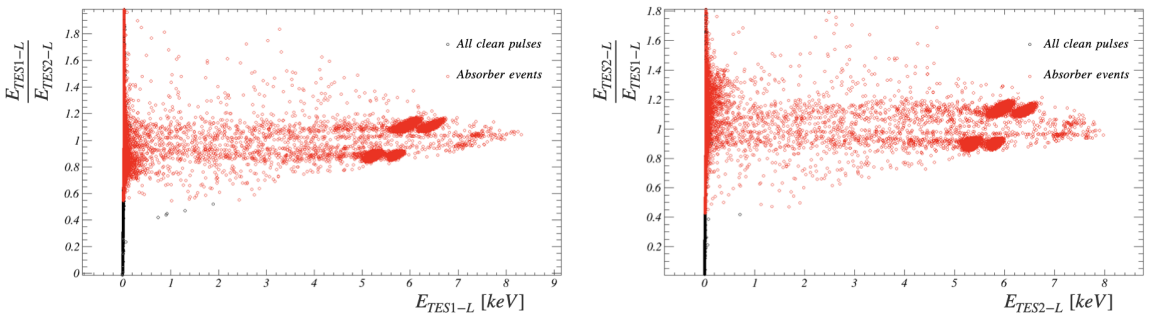

Figure 7.46: Plot of the ratio between the energy detected by the two TES as a function of the energy detected by TES1-L (*left*) and TES2-L (*right*). The absorber event cut is designed on this distribution, accepting only events in which the two TES observe a signal which does not differ by more than 50%.

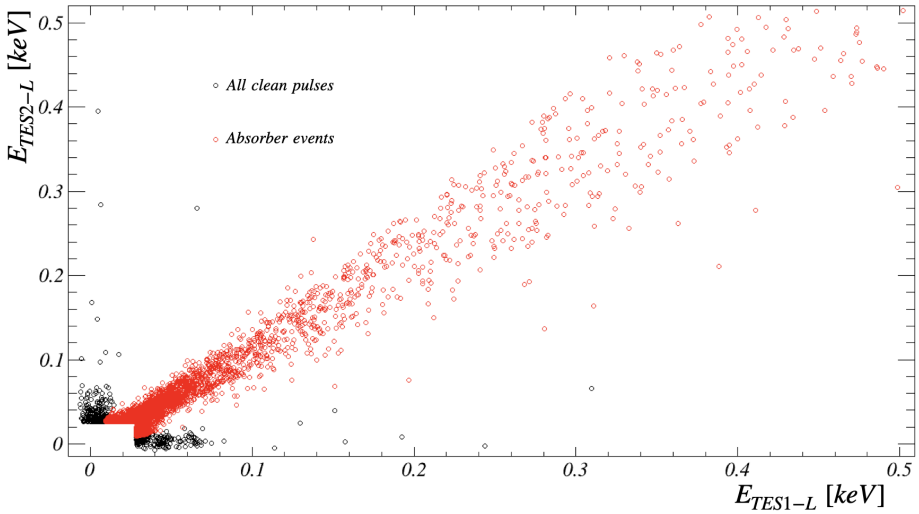

Figure 7.47: Zoom of the 2D energy spectrum of the SOS doubleTES module into energies below 500 eV. The events in red are the events accepted by the absorber events cut.

We observe an excess of events below 150 eV in the absorber events band. This measurement appears to indicate that the LEE comprises different components and that one includes events originating close to the sensors.

We studied the spectra extracted from the inverted data stream, as explained in

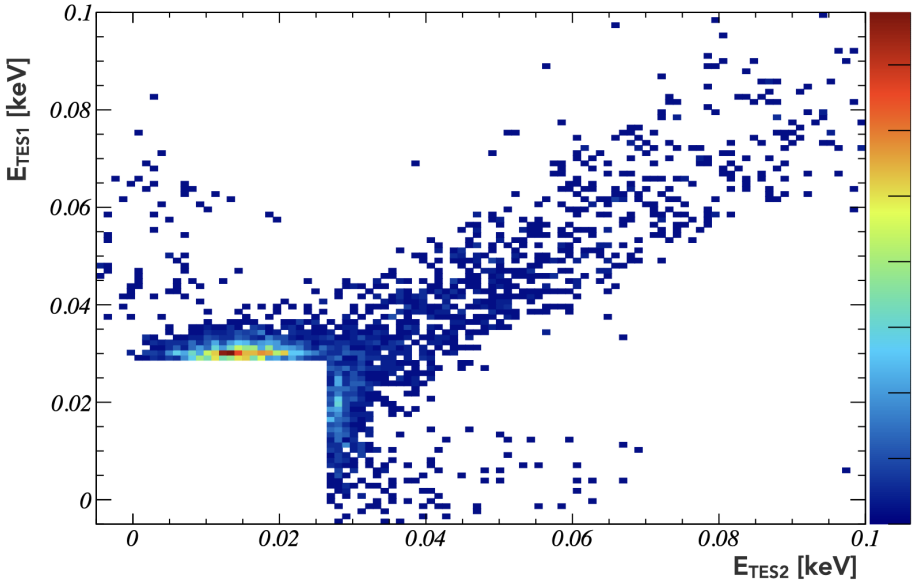

Figure 7.48: Zoom of the 2D histogram with the energies of the two TES of the SOS doubleTES module as axes into energies below 100 eV.

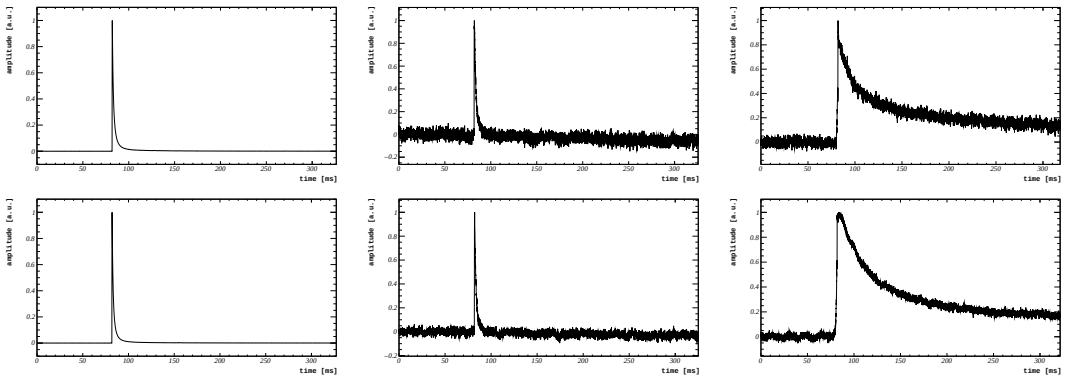

Figure 7.49: Standard events computed from different portions of the energy spectrum. On the left the template pulses from the 5.89 keV peak; in the centre, the standard events are computed from the events at the threshold with an equal share of the energy between the two sensors; on the right, standard events are computed with single TES events.

section 7.4, and we could observe that the events constituting the LEE only occur with a positive trigger, thus confirming that they are not misidentified noise triggers. Template pulses were created from different regions of the energy spectrum to further verify that the single TES events detected during this measurement are not noise

triggers. Figure 7.49 shows that while the single TES events exhibit a slower decay compared to standard absorber events, all populations consist of genuine pulses.
Performing parametric fits of the standard events from the absorber and the single TES components of the LEE allowed us quantify the difference in pulse shape among the different event populations. The function employed for this fit is eq. 4.21. The parametric fit has seven free parameters: the amplitudes of the non-thermal (A_n) and the thermal (A_t) components, the signal rise time (τ_n), the decay times of the non-thermal (τ_{in}) and thermal (τ_t) components, the baseline offset (p_{BL}) and the onset of the pulse ($onset$). Figure 7.50 reports pictures of these fits, while Table 7.1 reports the obtained parameters.

	A_n	A_t	τ_n	τ_{in}	τ_t	p_{BL}	$onset$
Absorber LEE event	-1.10	0.21	0.09	1.39	6.22	-0.02	81.80
Single TES event	-0.58	0.32	0.61	16.29	257.88	-0.002	80.93

Table 7.1: Parametric fit parameters for the standard event of absorber events with energies around 40-50 eV of TES1-L and for the standard event obtained with its single TES events.

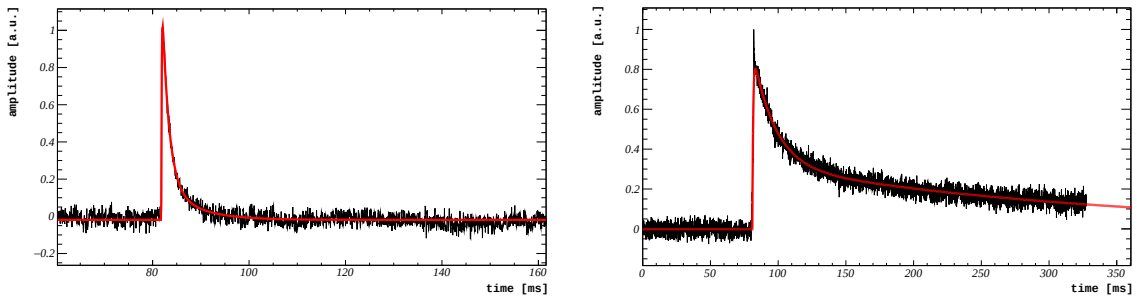

Figure 7.50: *Left:* Parametric fit of the standard event computed from absorber events with energies around 40-50 eV of TES1-L zoomed in time for a better visualisation. *Right:* Parametric fit of the standard single TES1-L event.

Radiation Impact Studies

The investigation into the impact of external radiation on the observed above-ground LEE was motivated by the consistently higher rates of excess events observed in above-ground measurements.
By conducting a second measurement after removing the iron sources from the experimental setup, we were able to study the influence of calibration sources on the results. The setup underwent minimal modifications: we carefully removed the sources while

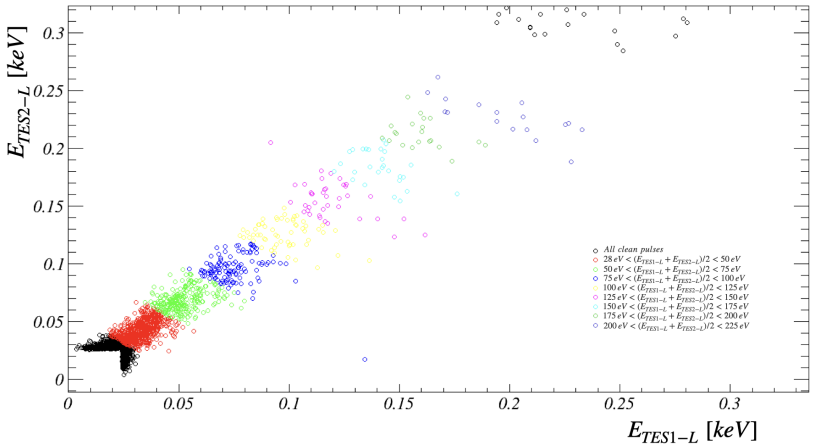

Figure 7.51: 2D energy spectrum of the SOS doubleTES module, during the measurement without the ^{55}Fe source and with the lead shield mounted. This plot highlights the energy ranges defined for the time dependence studies in different colours.

the rest (e.g. cables, sources, positions) remained unaltered.
As the changes to the setup were minimal, we assumed the calibration of the energy injected via the heater to be unchanged, and used it to calibrate the dataset.
As a result of the source removal, we could observe a roughly halved event rate at energies above 250 eV. However, on the LEE portion of the spectrum, we could not observe a significant reduction in the ebent rate, indicating that the calibration source did not significantly impact it.
To further assess the influence of external radiation on the LEE, we constructed a 10 cm thick lead shield around the cryostat (the same shield used during the $CaWO_4$ measurement in section 7.4) roughly 200 hours after the start of the second run. Despite reducing the overall event rate by approximately a factor of three, the lead shield did not affect the LEE. This observation led us to conclude that external radiation is not a significant source of excess events.

Time Dependence Studies

To verify the compatibility of our observations with the LEE measured in the CRESST setup, we studied the time dependence of the rate of the excess events. To do so, we sliced the 2D spectra of both measurements in different energy ranges, as highlighted in Figure 7.51. The ranges are defined using the average energy of the two channels: the first range is $28\,eV < (E_{TES1-L} + E_{TES2-L})/2 < 50\,eV$ the second one $50\,eV < (E_{TES1-L} + E_{TES2-L})/2 < 75\,eV$ and so on, with incrementations of 25 eV up to 225 eV. The most interesting energy intervals for LEE studies are the first two. The time behaviour of the event rate in these energy intervals are shown in Figure 7.52. For

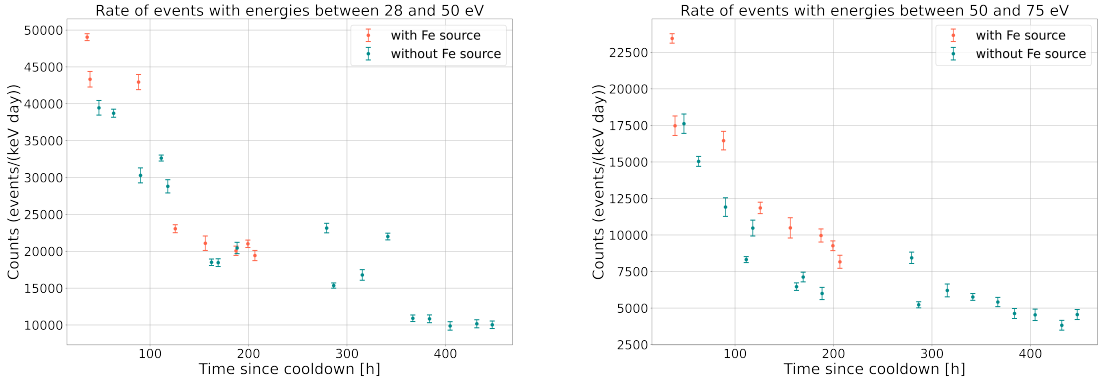

Figure 7.52: Time evolution for the absorber part of the above-ground LEE in the two experimental setups tested combined. In red are the rates from the measurement with the ^{55}Fe sources and in blue are the rates from the measurement without it. Every point of this plot corresponds to a single data file, and the errors are computed for each file singularly. The rates are corrected for the signal survival probability computed file by file. *Left:* Time evolution of the events with average energies between 28 and 50 eV. *Right:* Time evolution of events with average energies between 50 and 75 eV.

the the energy interval between 28 and 50 eV, we compute a decay time of (7.4±1.1) days for the measurement with the calibration sources, while the decay time computed for the measurement without the calibration sources is (12.4±1.5) days. Using the data points from both data sets, we calculate a decay time of (10.2±1.1) days. For the second energy interval (from 50 to 75 eV), we compute a decay time of (7.9±1.1) days in the measurement with the calibration sources, and a decay time of (11.3±1.7) days in absence of the sources. Considering data points from both sets, we calculate a decay time of (9.0±1.1) days.
These results are compatible with a decay time of approximately ten days, compatible with the decay time of the fast component of the LEE in the CRESST data set ((18±7) days [87]). The similarity in the decays of the above-ground and the underground LEE hints towards a similar origin of the two population. If these two population had a similar origin, the difference in rates typically observed (roughly 1-3 orders of magnitudes more in above-ground measurements) could be attributed to the faster beginning of data acquisition after cooldown and the generally shorter runs above-ground. Above-ground measurements usually begin a few hours after cooldown and end within a few days, while underground measurements typically commence some days after cooldown and go on for some months. Consequently, the major differences observed in the integrated spectra could be partially attributed to the decaying of LEE components in time. This hypothesis needs further testing, both above-ground and underground.

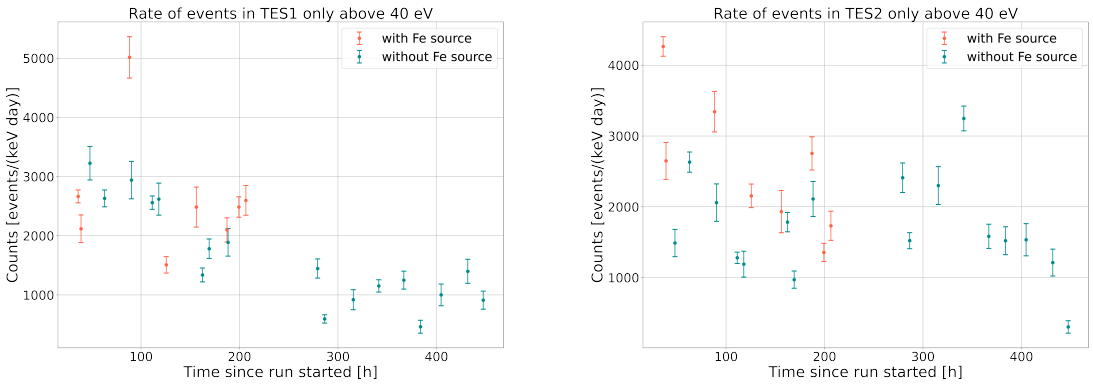

Figure 7.53: Time evolution of the TES1-L only (*left*) and TES2-L only (*right*) event rate of the above-ground LEE in the two experimental setups combined. In red are the rates from the measurement with the ^{55}Fe sources, and in blue are the rates from the measurement without them. Every point of this plot corresponds to a single data file, and the errors are computed for each file singularly. The rates are corrected for the signal survival probability computed file by file.

We also examined the rates of the events appearing in the individual W-TESs, focusing on events above 40 eV to avoid any leakage of absorber events into the single TES events bands.

The event rates in Figure 7.53 do not show a clear time behaviour within the limited timeframe of our measurements.

If these components do not decay in time (or decay much slower than the absorber component), they could become a dominant contribution to the LEE over a long run, and the doubleTES would provide a unique tool for discriminating them.

7.5.4 Conclusions

The test of the second doubleTES detector confirmed the presence of multiple components contributing to the LEE. One of these components generates a signal in only one of the two TESs, consistently appearing at the energy threshold of various detectors across all measurements. Our current calibration method relies on known energy deposits within the crystal bulk to calibrate the entire energy spectrum of the sensors. However, these single TES events seem to originate near a single sensor, indicating they may require a distinct energy calibration or modelling.

Another key observation from this measurement concerns of the observed time

dependence of the absorber events component of the LEE. The decay observed is compatible with the decay of the fast component of the LEE observed in the underground environment of the CRESST experiment. This observation might suggest a potential common origin of the two populations, with the higher event rate typically observed in above-ground measurements potentially attributed to differences in experimental durations rather than inherent differences in the origin of the events. Further tests above-ground and underground are needed and planned for a comprehensive investigation of this possibility.

7.6 Underground Measurement and Outlook

Based on the promising results detailed in this chapter, five complete standard doubleTES modules ($20\times20\times10\,\mathrm{mm}^3$ $CaWO_4$ coupled to SOS wafer with a single TES as LD) have been mounted in the CRESST underground facility for the so-called Run37. To enhance our understanding of the LEE, we have also installed a stack of four SOS doubleTES detectors stacked on top of each other for surface events vetoing. This module aims to lower the energy threshold as much as possible and gather deeper insight into the LEE. Pictures of these modules are shown in Figure 7.54.

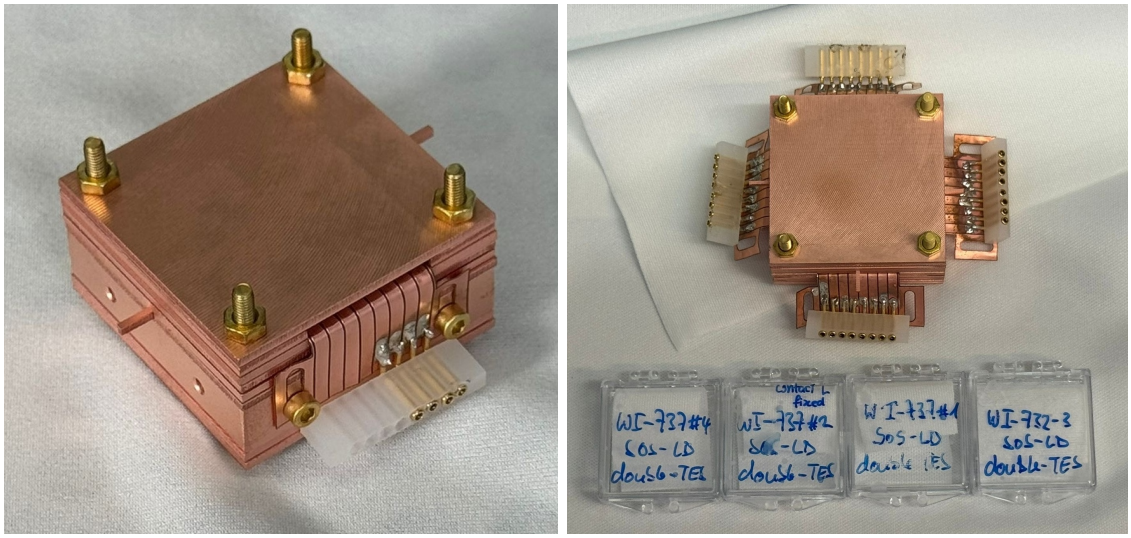

Figure 7.54: Pictures of the two types of module mounted for Run37. *Left:* One of the Standard doubleTES module. *Right:* SOS doubleTES stack.

The doubleTES standard modules do not contain a calibration source, as we intend to employ the energy calibration method proposed by the CRAB collaboration in [145].

This method, previously successful with $CaWO_4$ crystals [146], utilises the nuclear recoils caused by the radiative capture of thermal neutron on W isotopes, which provides a peak at recoil energy of $\sim$112 eV that can be used for calibration.
Conversely, the stack of SOS doubleTES has been equipped with ^{55}Fe sources for energy calibration. Each pair of SOS doubleTES detectors in the stack is equipped with a 0.7 mBq ^{55}Fe source, mounted on a copper wire and fixed between the two crystals.

With the upcoming measurement, we will shed more light on the LEE mystery, thanks to the employment of this newly designed detector module, which has demonstrated an unprecedented capability to discriminate different LEE components.
The described modules were installed inside the CRESST cryostat at LNGS in February 2024, and the cryostat was cooled down at the beginning of March.
Preliminary results are foreseen by the end of 2024.

Chapter 8

Conclusions and Outlook

Dark matter is one of the most investigated mysteries of modern physics and unveiling its nature has motivated numerous experiments in the past few decades. The CRESST experiment is a direct detection dark matter experiment aimed at observing dark matter particles scattering off target nuclei in cryogenic calorimeters operated around 15 mK. The CRESST-III detector modules feature a main (typically scintillating) absorber crystal, equipped with a W-TES, and an associated light detector, also equipped with a W-TES, for particle identification.
This thesis explores the possibility of extending the physics reach of the CRESST experiment in multiple ways.
The W-TES design plays a crucial role in determining the sensitivity to dark matter interactions. The dedicated study conducted demonstrates that the sensitivity of the current sensors design can be improved, particularly targeting the phonon collectors design. Consequently, the TES design for the currently starting CRESST measurement campaign, Run37, has been adjusted based on these findings.
In the near future, the CRESST facility will undergo a major upgrade, which will entail an increase in the number of detectors from $\mathcal{O}(10)$ to $\mathcal{O}(100)$. In light of this, we investigate sputtering as a novel and more efficient TES production method, facilitating mass production of sensors with reproducible performance. A procedure to reliably obtain sputtered superconducting W thin films on various substrates is established. Further studies, specifically focusing on understanding the type and magnitude of the stress stored in the films, may give more insight on the characteristics driving the superconducting properties of these films. Extensive additional investigations could help fine-tune the transition temperature of the sputtered W thin films by adjusting sputtering parameter.
Currently, the main limitation to the sensitivity of numerous dark matter direct detection experiments, including CRESST, is a backgroung of unknown origin, known as the Low Energy Excess. In CRESST it manifests as an increate in events rate at energies below 200 eV. An extensive campaign to study the LEE has been undertaken by CRESST in the past years, yielding valuble insight into this signal. The doubleTES

module has been developed to explore remaining open hypotheses about the LEE's origin. Above-ground tests of doubleTES detectors prototypes presented in this thesis demonstrate the capability of the doubleTES to distinguish events originating in the bulk of the crystal from events originating in the close proximity of one of TES. Various components of the LEE are detected in all measurement campaigns, and one of these components only generates a signal in one of the two TES.
Using a low threshold doubleTES, the energy spectrum below 150 eV is explored, and an absorber events component of the LEE is identified. This component is observed to decay over time with a time of approximately 10 days, compatible with the fast decay observed in the CRESST underground setup. Analyses of the average pulses from different populations confirmed that these events are not compatible with misidentified noise. By removing the calibration source and shielding the cryostat, a major contribution from external radiation to the LEE is ruled out.
Various doubleTES detectors were installed at the LNGS CRESST underground facility in February 2024. This measurement will provide further insight into the LEE.

Bibliography

[1] F. Zwicky, The redshift of extragalactic nebulae, Helvetica Physica Acta **6**, 110–127 (1933)

[2] M. Colless A.M. Dunn, Structure and dynamics of the coma cluster, The Astrophysical Journal **458**, 435 (1996). http://dx.doi.org/10.1086/176827

[3] F. Zwicky, On the Masses of Nebulae and of Clusters of Nebulae, Astrophys. J. **86**, 217 (1937)

[4] K. Begeman, HI rotation curves of spiral galaxies. Ph.D. thesis (2006). Date submitted: 2006 Rights: University of Groningen

[5] V. Rubin J. Ford, W.K., Rotation of the Andromeda Nebula from a Spectroscopic Survey of Emission Regions, APJ **159**, 379 (1970)

[6] V. Rubin et al., Extended rotation curves of high-luminosity spiral galaxies. IV. Systematic dynamical properties, Sa -> Sc., APJL **225**, L107 (1978)

[7] V. Rubin et al., Rotational properties of 21 SC galaxies with a large range of luminosities and radii, from NGC 4605 (R=4kpc) to UGC 2885 (R=122kpc)., APJ **238**, 471 (1980)

[8] T. van Albada et al., Distribution of dark matter in the spiral galaxy NGC 3198., APJ **295**, 305 (1985)

[9] J.F. Navarro et al., The structure of cold dark matter halos, The Astrophysical Journal **462**, 563 (1996). http://dx.doi.org/10.1086/177173

[10] J. Einasto, On the Construction of a Composite Model for the Galaxy and on the Determination of the System of Galactic Parameters, Trudy Astrofizicheskogo Instituta Alma-Ata **5**, 87 (1965)

[11] M. Milgrom, A modification of the Newtonian dynamics as a possible alternative to the hidden mass hypothesis., APJ **270**, 365 (1983)

[12] Chandra X-ray observatory (2021). https://chandra.harvard.edu/photo/2006/1e0657/more.html

[13] D. Clowe et al., A direct empirical proof of the existence of dark matter, The Astrophysical Journal **648**(2), L109–L113 (2006). http://dx.doi.org/10.1086/508162

[14] A. Robertson et al., What does the bullet cluster tell us about self-interacting dark matter?, Monthly Notices of the Royal Astronomical Society **465**(1), 569–587 (2016). http://dx.doi.org/10.1093/mnras/stw2670

[15] A.M. Green, Dark matter in astrophysics/cosmology, SciPost Phys. Lect. Notes p. 37 (2022). https://scipost.org/10.21468/SciPostPhysLectNotes.37

[16] Particle data group, R.L. Workman Others, Chapter 24, Big Bang Nucleosynthesis, Prog. Theor. Exp. Phys. 2022, 083C01, PTEP **2022**, 083C01 (2022)

[17] R.H. Cyburt et al., Big bang nucleosynthesis: Present status, Rev. Mod. Phys. **88**, 015004 (2016). https://link.aps.org/doi/10.1103/RevModPhys.88.015004

[18] B. Ryden, *Introduction to Cosmology* (Addison-Wesley, 2003). https://books.google.de/books?id=z27vAAAAMAAJ

[19] G. Smoot et al., Structure in the COBE differential microwave radiometer first-year maps, Astrophysical Journal Letters **396**, L1 (1992)

[20] Particle data group, R.L. Workman Others, Chapter 29, Cosmic Microwave Background, Prog. Theor. Exp. Phys. 2022, 083C01, PTEP **2022**, 083C01 (2022)

[21] N. Aghanim et al., Planck2018 results: VI. cosmological parameters, Astronomy & Astrophysics **641**, A6 (2020). http://dx.doi.org/10.1051/0004-6361/201833910

[22] T. Padmanabhan, *Structure formation in the universe* (Cambridge university press, 1993)

[23] J.R. Primack. Dark matter and structure formation in the universe (1997)

[24] M. Davis et al., The evolution of large-scale structure in a universe dominated by cold dark matter, APJ **292**, 371 (1985)

[25] M. Davis et al., The end of cold dark matter?, Nature **356**(6369), 489 (1992). https://doi.org/10.1038/356489a0

[26] V. Iršič et al., First constraints on fuzzy dark matter from Lyman-α forest data and hydrodynamical simulations, Physical Review Letters **119**(3) (2017). http://dx.doi.org/10.1103/PhysRevLett.119.031302

[27] E. Aprile et al., Searching for heavy dark matter near the planck mass with xenon1t, Physical Review Letters **130**(26) (2023). http://dx.doi.org/10.1103/PhysRevLett.130.261002

[28] J. Billard et al., Direct detection of dark matter—APPEC committee report*, Reports on Progress in Physics **85**(5), 056201 (2022). http://dx.doi.org/10.1088/1361-6633/ac5754

[29] B. Dev S. Qutub, Constraining non-thermal and thermal properties of dark matter, Frontiers in Physics **2** (2013)

[30] P.A.R. Ade et al., Planck2013 results. XVI. cosmological parameters, Astronomy & Astrophysics **571**, A16 (2014). http://dx.doi.org/10.1051/0004-6361/201321591

[31] S. Profumo. Tasi 2012 lectures on astrophysical probes of dark matter (2013)

[32] D. Bhatia S. Mukhopadhyay, Unitarity limits on thermal dark matter in (non-)standard cosmologies, Journal of High Energy Physics **2021**(3) (2021). http://dx.doi.org/10.1007/JHEP03(2021)133

[33] J.L. Feng, Dark matter candidates from particle physics and methods of detection, Annual Review of Astronomy and Astrophysics **48**(1), 495–545 (2010). http://dx.doi.org/10.1146/annurev-astro-082708-101659

[34] L.J. Hall et al., Freeze-in production of fimp dark matter, Journal of High Energy Physics **2010**(3) (2010). http://dx.doi.org/10.1007/JHEP03(2010)080

[35] R.D. Peccei H.R. Quinn, Constraints imposed by CP conservation in the presence of pseudoparticles, Phys. Rev. D **16**, 1791 (1977). https://link.aps.org/doi/10.1103/PhysRevD.16.1791

[36] M. Dine. TASI Lectures on The Strong CP Problem (2000)

[37] Particle data group, R.L. Workman Others, Chapter 59, Quark Masses, Prog. Theor. Exp. Phys. 2022, 083C01, PTEP **2022**, 083C01 (2022)

[38] I. Garcia Irastorza, An introduction to axions and their detection, SciPost Physics Lecture Notes (2022). http://dx.doi.org/10.21468/SciPostPhysLectNotes.45

[39] O. Buchmueller et al., Search for dark matter at colliders, Nature Physics **13**(3), 217–223 (2017). http://dx.doi.org/10.1038/nphys4054

[40] S. Chatrchyan et al., Search for dark matter and large extra dimensions in monojet events in pp collisions at $\sqrt{s} = 7$ TeV, Journal of High Energy Physics **2012**(9), 94 (2012). https://doi.org/10.1007/JHEP09(2012)094

[41] G. Aad et al., Search for dark matter candidates and large extra dimensions in events with a jet and missing transverse momentum with the ATLAS detector, Journal of High Energy Physics **2013**(4), 75 (2013). https://doi.org/10.1007/JHEP04(2013)075

[42] J.M. Gaskins, A review of indirect searches for particle dark matter, Contemporary Physics **57**(4), 496–525 (2016). http://dx.doi.org/10.1080/00107514.2016.1175160

[43] C. Pérez de los Heros, Status, challenges and directions in indirect dark matter searches, Symmetry **12**(10), 1648 (2020). http://dx.doi.org/10.3390/sym12101648

[44] R.K. Leane. Indirect detection of dark matter in the galaxy (2020)

[45] D. Hooper. TASI lectures on indirect searches for dark matter (2018)

[46] S. Guiriec et al., Time-resolved spectroscopy of the three brightest and hardest short gamma-ray bursts observed with thefermigamma-ray burst monitor, The Astrophysical Journal **725**(1), 225–241 (2010). http://dx.doi.org/10.1088/0004-637X/725/1/225

[47] M. Ahnen et al., Indirect dark matter searches in the dwarf satellite galaxy ursa major ii with the magic telescopes, Journal of Cosmology and Astroparticle Physics **2018**(03), 009–009 (2018). http://dx.doi.org/10.1088/1475-7516/2018/03/009

[48] D.M.H. Leung K.C.Y. Ng. Improving HAWC dark matter constraints with inverse-compton emission (2023)

[49] P.W. Graham et al., Experimental searches for the axion and axion-like particles, Annual Review of Nuclear and Particle Science **65**(1), 485–514 (2015). http://dx.doi.org/10.1146/annurev-nucl-102014-022120

[50] J. Cooley, Dark matter direct detection of classical WIMPs, SciPost Physics Lecture Notes (2022). http://dx.doi.org/10.21468/SciPostPhysLectNotes.55

[51] P.F. de Salas A. Widmark, Dark matter local density determination: recent observations and future prospects, Reports on Progress in Physics **84**(10), 104901 (2021). http://dx.doi.org/10.1088/1361-6633/ac24e7

[52] I.M. Bloch et al., Exploring new physics with O(keV) electron recoils in direct detection experiments, Journal of High Energy Physics **2021**(1), 178 (2021)

[53] W. Wang et al. Direct detection of finite-size dark matter via electron recoil (2023)

[54] J.B. Dent et al., General analysis of direct dark matter detection: From microphysics to observational signatures, Phys. Rev. D **92**, 063515 (2015). https://link.aps.org/doi/10.1103/PhysRevD.92.063515

[55] R.J. Gaitskell, Direct detection of dark matter, Annu. Rev. Nucl. Part. Sci. **54**, 315 (2004)

[56] P. Gondolo et al., Phenomenology of nuclear scattering for a WIMP of arbitrary spin, Physical Review D **104**(6) (2021). http://dx.doi.org/10.1103/PhysRevD.104.063018

[57] Abdelhameed, A. H. et al., A low-threshold diamond cryogenic detector for sub-gev dark matter searches, Eur. Phys. J. C **82**(9), 851 (2022). https://doi.org/10.1140/epjc/s10052-022-10829-5

[58] K. Freese et al., Annual modulation of dark matter: A review (2012). https://api.semanticscholar.org/CorpusID:118453730

[59] D.N. Spergel, Motion of the earth and the detection of weakly interacting massive particles, Phys. Rev. D **37**, 1353 (1988). https://link.aps.org/doi/10.1103/PhysRevD.37.1353

[60] T. Asada et al., Directional dark matter search wih the fine grained nuclear emulsion p. 030 (2015)

[61] N. Agafonova et al., Discovery potential for directional dark matter detection with nuclear emulsions, The European Physical Journal C **78**(7), 578 (2018). https://doi.org/10.1140/epjc/s10052-018-6060-1

[62] K. Miuchi et al., CYGNUS, Journal of Physics: Conference Series **1468**(1), 012044 (2020). https://dx.doi.org/10.1088/1742-6596/1468/1/012044

[63] G. Heusser, Low-radioactivity background techniques, Ann. Rev. Nucl. Part. Sci. **45**, 543 (1995)

[64] A. Ianni, Underground laboratories, SciPost Physics Proceedings (2023)

[65] T. Shutt et al., Measurement of ionization and phonon production by nuclear recoils in a 60 g crystal of germanium at 25 mk, Phys. Rev. Lett. **69**, 3425 (1992). https://link.aps.org/doi/10.1103/PhysRevLett.69.3425

[66] C.E. Aalseth et al., Results from a search for light-mass dark matter with a p-type point contact germanium detector, Physical Review Letters **106**(13) (2011). http://dx.doi.org/10.1103/PhysRevLett.106.131301

[67] I. Arnquist et al. The DAMIC-M experiment: Status and first results (2022)

[68] Sensei collaboration, L. Barak et al., SENSEI: Direct-detection results on sub-gev dark matter from a new skipper CCD, Phys. Rev. Lett. **125**, 171802 (2020). https://link.aps.org/doi/10.1103/PhysRevLett.125.171802

[69] E. Aprile et al., First dark matter search with nuclear recoils from the XENONnT experiment, Physical Review Letters **131**(4) (2023). http://dx.doi.org/10.1103/PhysRevLett.131.041003

[70] P. Agnes et al., Darkside-50 532-day dark matter search with low-radioactivity argon, Physical Review D **98**(10) (2018). http://dx.doi.org/10.1103/PhysRevD.98.102006

[71] R. Ajaj et al., Search for dark matter with a 231-day exposure of liquid argon using DEAP-3600 at SNOLAB, Physical Review D **100**(2) (2019). http://dx.doi.org/10.1103/PhysRevD.100.022004

[72] G.D. for the SABRE collaboration, Dark matter search with the SABRE experiment, Journal of Physics: Conference Series **1342**(1), 012060 (2020). https://dx.doi.org/10.1088/1742-6596/1342/1/012060

[73] D.D.A. Bauer, Dark matter detection with cryogenic detectors, Journal of Physics: Conference Series **120**(4), 042002 (2008). https://dx.doi.org/10.1088/1742-6596/120/4/042002

[74] C. Amole et al., Dark matter search results from the complete exposure of the PICO-60 C_3F_8 bubble chamber, Physical Review D **100**(2) (2019). http://dx.doi.org/10.1103/PhysRevD.100.022001

[75] A. Meregaglia A. Pullia, Searches for dark matter with superheated liquid techniques, Advances in High Energy Physics **2014**, 387493 (2014). https://doi.org/10.1155/2014/387493

[76] G. Angloher et al., Testing spin-dependent dark matter interactions with lithium aluminate targets in CRESST-III, Physical Review D **106**(9) (2022). http://dx.doi.org/10.1103/PhysRevD.106.092008

[77] S. Di Lorenzo, Multiple detector analysis in the CRESST dark matter experiment. Dissertation, GSSI, L'Aquila, Italy (2020)

[78] A. C. et al., Radon measurements in the gran sasso underground laboratory, Health Phys. **72**(4) (1997). https://www.sciencedirect.com/science/article/pii/S0927650509000358

[79] F. Pobell, *Matter and Methods at Low Temperatures* (Springer Berlin, Heidelberg, 1992). DOI https://doi.org/10.1007/978-3-662-08578-3

[80] F. Pröbst et al., Results of CRESST phase I, Nuclear Physics B - Proceedings Supplements **110**, 67 (2002). https://www.sciencedirect.com/science/article/pii/S0920563202014536

[81] G. Angloher et al., Limits on WIMP dark matter using scintillating $CaWO_4$ cryogenic detectors with active background suppression, Astroparticle Physics **23**(3), 325 (2005). https://www.sciencedirect.com/science/article/pii/S0927650505000071

[82] G. Angloher et al., Results on light dark matter particles with a low-threshold CRESST-II detector, The European Physical Journal C **76**(1), 25 (2016). https://doi.org/10.1140/epjc/s10052-016-3877-3

[83] A. Tanzke, Low-threshold detectors for low-mass direct dark matter search with CRESST-III. Ph.D. thesis, Technische Universität München (2017)

[84] R. Strauss et al., Gram-scale cryogenic calorimeters for rare-event searches, Phys. Rev. D **96**, 022009 (2017). https://link.aps.org/doi/10.1103/PhysRevD.96.022009

[85] N. Ferreiro Iachellini. Increasing the sensitivity to low mass dark matter in CRESST-III with a new daq and signal processing (2019). http://nbn-resolving.de/urn:nbn:de:bvb:19-237623

[86] CRESST collaboration, A.H. Abdelhameed et al., First results from the CRESST-III low-mass dark matter program, Phys. Rev. D **100**, 102002 (2019). https://link.aps.org/doi/10.1103/PhysRevD.100.102002

[87] G. Angloher et al., Latest observations on the low energy excess in CRESST-III (2022). https://arxiv.org/abs/2207.09375

[88] CRESST collaboration, G. Angloher et al., Results on sub-gev dark matter from a 10 ev threshold CRESST-III silicon detector, Phys. Rev. D **107**, 122003 (2023). https://link.aps.org/doi/10.1103/PhysRevD.107.122003

[89] G. Angloher et al., Detector development for the CRESST experiment, Journal of Low Temperature Physics (2024). https://doi.org/10.1007/s10909-024-03154-6

[90] E. Fiorini T. Niinikoski, Low-temperature calorimetry for rare decays, Nuclear Instruments and Methods in Physics Research **224**(1), 83 (1984). https://www.sciencedirect.com/science/article/pii/0167508784904496

[91] S.H. Moseley et al., Thermal detectors as X-ray spectrometers, Journal of Applied Physics **56**(5), 1257 (1984). https://doi.org/10.1063/1.334129

[92] K. Pretzl, *Cryogenic Detectors* (Springer International Publishing, Cham, 2020), pp. 871–912. DOI 10.1007/978-3-030-35318-6_19. https://doi.org/10.1007/978-3-030-35318-6_19

[93] F. Pröbst et al., Model for cryogenic particle detectors with superconducting phase transition thermometers, J. Low Temp. Phys. **100**(1), 69 (1995)

[94] M. Born, Born-oppenheimer approximation, Ann. Phys **84**, 457 (1927)

[95] J. Bardeen et al., Theory of superconductivity, Phys. Rev. **108**, 1175 (1957). https://link.aps.org/doi/10.1103/PhysRev.108.1175

[96] S.B. Kaplan, Acoustic matching of superconducting films to substrates, Journal of Low Temperature Physics **37**(3), 343 (1979). https://doi.org/10.1007/BF00119193

[97] J. Liu N. Giordano, Electron-phonon scattering times in thin sb films, Phys. Rev. B **43**, 3928 (1991). https://link.aps.org/doi/10.1103/PhysRevB.43.3928

[98] J.F. DiTusa et al., Role of phonon dimensionality on electron-phonon scattering rates, Phys. Rev. Lett. **68**, 1156 (1992). https://link.aps.org/doi/10.1103/PhysRevLett.68.1156

[99] A. Pippard, CXXII. ultrasonic attenuation in metals, The London, Edinburgh, and Dublin Philosophical Magazine and Journal of Science **46**(381), 1104 (1955). https://doi.org/10.1080/14786441008521122

[100] R. Franz G. Wiedemann, Ueber die Wärme-Leitungsfähigkeit der Metalle, Annalen der Physik **165**(8), 497 (1853). https://onlinelibrary.wiley.com/doi/abs/10.1002/andp.18531650802

[101] F. Petricca, Dark Matter Search with Cryogenic Phonon-Light Detectors. Ph.D. thesis, Ludwig-Maximilians-Universität München (2005)

[102] M. Kurakado, Possibility of high resolution detectors using superconducting tunnel junctions, Nuclear Instruments and Methods in Physics Research **196**(1), 275 (1982). https://www.sciencedirect.com/science/article/pii/0029554X82906541

[103] M. Loidl, Diffusion and detection of quasiparticles. Ph.D. thesis, Technische Universität München (1999)

[104] J. Clarke, Principles and applications of squids, Proceedings of the IEEE **77**(8), 1208 (1989)

[105] E. Pantić, Performance of Cryogenic Light Detectors in the CRESST-II Dark Matter Search. Ph.D. thesis, Universitätsbibliothek der TU München (2008)

[106] M. Galeazzi D. McCammon, Microcalorimeter and bolometer model, Journal of Applied Physics **93**(8), 4856–4869 (2003). http://dx.doi.org/10.1063/1.1559000

[107] M. Wüstrich, Improving particle discrimination and achieving a 4π-veto detector concept for the CRESST experiment. Ph.D. thesis, Technische Universität München (2020)

[108] J.F.M. Rothe, Low-threshold cryogenic detectors for low-mass dark matter search and coherent neutrino scattering. Ph.D. thesis, Technische Universität München (2021)

[109] J. Yen et al., Quasiparticle transport in thick aluminum films coupled to tungsten transition edge sensors, Journal of Low Temperature Physics **184** (2016)

[110] F. Mang. Study of aluminium phonon collectors for CRESST transition edge sensors [unpublished] (2020)

[111] R. Holm W. Meissner, Messungen mit Hilfe von flssigem Helium. XIII, European Physical Journal A (1932). https://api.semanticscholar.org/CorpusID:126976182

[112] O.H. K., The superconductivity of mercury, Comm. Phys. Lab. Univ. Leiden **122**, 124 (1911). https://cir.nii.ac.jp/crid/1572543025917034112

[113] W. Meissner R. Ochsenfeld, Ein neuer effekt bei eintritt der supraleitfähigkeit, Naturwiss. **21**(44), 787 (1933)

[114] A. Rose-Innes E. Rhoderick, *Introduction to Superconductivity*. International series in solid state physics (Elsevier Science & Technology Books, 1978). https://books.google.de/books?id=pCwbAQAAIAAJ

[115] M.M. Zanirato. R&D of dark matter cryogenic detectors for the CRESST experiment: Study of impacts of an aluminium layer as a shield against magnetic fields (2023)

[116] A.H.S. Abdelhameed, Aspects of TES novel reproducibility for cryogenic detectors dedicated to dark matter search. Ph.D. thesis, Technische Universität München (2022)

[117] G. Angloher et al. Probing low WIMP masses with the next generation of CRESST detector (2015)

[118] D.R. Fuchs, New analysis methods for enhanced sensitivity to light dark matter at CRESST-III and studies of discovery potential for next generation cryogenic experiments. Ph.D. thesis, Technische Universität München (2023). https://mediatum.ub.tum.de/1709800

[119] P. Colling et al., Superconducting tungsten films for use as phase transition thermometers for calorimetric detectors (1994)

[120] L. Erik W.D. Schubert, *Tungsten* (Springer New York, NY, 1999). DOI https://doi.org/10.1007/978-1-4615-4907-9

[121] J.W. Gibson R.A. Hein, Superconductivity of tungsten, Phys. Rev. Lett. **12**, 688 (1964). https://link.aps.org/doi/10.1103/PhysRevLett.12.688

[122] R.T. Johnson et al., Superconductivity of tungsten, Phys. Rev. Lett. **16**, 101 (1966). https://link.aps.org/doi/10.1103/PhysRevLett.16.101

[123] W.C. Black et al., Critical magnetic field curve of superconducting tungsten, Journal of Low Temperature Physics **1**(6), 641 (1969). https://doi.org/10.1007/BF00627939

[124] B.B. Triplett et al., Critical field for superconductivity and low-temperature normal-state heat capacity of tungsten, Journal of Low Temperature Physics **12**(5), 499 (1973). https://doi.org/10.1007/BF00654953

[125] S. Basavaiah S.R. Pollack, Superconductivity in evaporated tunsten films, Applied Physics Letters **12**(8), 259 (1968). https://doi.org/10.1063/1.1651982

[126] S. Basavaiah S.R. Pollack, Superconductivity in β-Tungsten Films, Journal of Applied Physics **39**(12), 5548 (1968). https://doi.org/10.1063/1.1656012

[127] J. Bardeen et al., Microscopic theory of superconductivity, Phys. Rev. **106**, 162 (1957). https://link.aps.org/doi/10.1103/PhysRev.106.162

[128] R.H. Willens E. Buehler, THE SUPERCONDUCTIVITY OF THE MONOCARBIDES OF TUNGSTEN AND MOLYBDENUM, Applied Physics Letters **7**(1), 25 (1965). https://doi.org/10.1063/1.1754239

[129] A.E. Aliev, High-T_C superconductivity in nanostructured Na_xWO_{3-y}: sol-gel route, Superconductor Science and Technology **21**(11), 115022 (2008). https://dx.doi.org/10.1088/0953-2048/21/11/115022

[130] A.R. L.P. Gor'kov, Ferromagnetism in superconducting alloys, Jurnal of Experimental and Theoretical Physics **19**(4) (1964)

[131] H.A. Notarys, Effect of tensile stress on the Superconducting Transition Temperature of Al Films, Applied Physics Letters **4**(4), 79 (1964). https://doi.org/10.1063/1.1753971

[132] P.M. Hall, Effect of Stress on the Superconducting Transition Temperature of Thin Films of Tin, Journal of Applied Physics **36**(8), 2471 (1965). https://doi.org/10.1063/1.1714513

[133] M. Mito et al., Large enhancement of superconducting transition temperature in single-element superconducting rhenium by shear strain, Scientific Reports **6**(1), 36337 (2016). https://doi.org/10.1038/srep36337

[134] V. Palmieri et al., The way of thick films toward a flat Q-curve in sputtered cavities (2017)

[135] S. Roth, Sputtered tungsten thin films and composite detectors for the application in the dark matter experiments CRESST and EURECA. Master thesis, Technische Universität München (2007)

[136] T. Ortmann, Characterization of sputtered tungsten thin films for the CRESST experiment using transition measurements and x-ray diffraction. Master thesis, Technische Universität München (2017)

[137] D.W. Hoffman, Perspective on stresses in magnetron sputtered thin films, Journal of Vacuum Science & Technology A **12**(4), 953 (1994). https://doi.org/10.1116/1.579073

[138] G. Angloher et al. DoubleTES detectors to investigate the CRESST low energy background: results from above-ground prototypes (2024)

[139] E. Gatti P.F. Manfredi, Processing the Signals From Solid State Detectors in Elementary Particle Physics, Riv. Nuovo Cim. **9N1**, 1 (1986)

[140] R.S. et al., A prototype detector for the CRESST-III low-mass dark matter search, Nuclear Instruments and Methods in Physics Research Section A: Accelerators, Spectrometers, Detectors and Associated Equipment **845**, 414 (2017)

[141] M. Mancuso et al., A low nuclear recoil energy threshold for dark matter search with CRESST-III detectors, Journal of Low Temperature Physics **193**(3), 441 (2018). https://doi.org/10.1007/s10909-018-1948-6

[142] M. Mancuso et al., A method to define the energy threshold depending on noise level for rare event searches, Nuclear Instruments and Methods in Physics Research Section A: Accelerators, Spectrometers, Detectors and Associated Equipment **940**, 492 (2019). https://www.sciencedirect.com/science/article/pii/S0168900219308708

[143] *Update of X Ray and Gamma Ray Decay Data Standards for Detector Calibration and Other Applications*. Non-serial Publications (INTERNATIONAL ATOMIC ENERGY AGENCY, Vienna, 2007)

[144] G. Angloher et al. Deep-underground dark matter search with a COSINUS detector prototype (2023)

[145] L. Thulliez et al., Calibration of nuclear recoils at the 100 ev scale using neutron capture, Journal of Instrumentation **16**(07), P07032 (2021). https://dx.doi.org/10.1088/1748-0221/16/07/P07032

[146] CRESST Collaboration, G. Angloher et al., Observation of a low energy nuclear recoil peak in the neutron calibration data of the CRESST-III experiment, Phys. Rev. D **108**, 022005 (2023). https://link.aps.org/doi/10.1103/PhysRevD.108.022005

Acknowledgments

These three and a half years of PhD have been a rollercoaster in every possible way, full of ups and downs, but I would do it all over again. In this journey, I grew up and learned many things about physics, the world and myself. I am very thankful to everyone who shared this path with me.
First of all, I want to thank Dr. Federica Petricca for giving me the opportunity to join this incredible MPP group and the CRESST Collaboration. Grazie per essere stata un ottimo capo, e per avermi guidato e supportato in quest anni. Non é stato un percorso facile, ma ho sempre potuto contare sul tuo appoggio e supporto, e per questo ti sono immensamente grata.
I want to thank the entire MPP CRESST group (past and present) for being the great working group you are, always fun and full of ideas. Working here was a blast, and it would not have been the same without you. Thank you Anna, Michele, Dom, Abhi, Alex, Bea, Pedro, Marco, Ele, Ludo, Dieter, Antonio, Federica, Felix, Heerak, Stefano.
I would also like to thank the full CRESST Collaboration, for the fruitful discussions and for all the support.
My biggest gratitude goes to Dr. Michele Mancuso, my mentor, the person who taught me all I know and the best cryogenist I have ever met. Non credo di poter esprimere a parole, in uno spazio ristretto tutti i motivi per cui ti sono grata. Grazie per essere sempre stato presente, per avermi guidato in questo percorso, per avermi insegnato cosi tanto. Grazie soprattutto per avermi insegnato un'attitudine positiva al lavoro, alla ricerca di soluzioni, e non di problemi. Grazie per avermi accolto al mio arrivo a Monaco, per i pranzi, le cene e le birre. Grazie per la tua amicizia, per le litigate, per avermi ascoltato e per non aver mollato, nemmeno quando ti ho fatto esasperare. Non avrei potuto desiderare guida migliore per questo percorso assurdo. Grazie per averlo reso cosi divertente e appassionante. E grazie a Federica, Sebastian e Marcus per avermi fatto sentire sempre un po' a casa.
I would like to thank Dr. Abhijit Garai, for being my second fundamental guide in this journey. Thank you, Abhi, for keeping up with me, guiding me in many ways, and teaching me so much. You succeeded in the impossible task of teaching me how to fit the bond wire through the needle, and this tells everything about what a great teacher you are. Thank you for being so patient with me, always keeping my morale up, and never letting me give up. Thanks for staying longer at LNGS to try to fix the

unbelievable issues we faced. Working with you was a great honour. Thanks also for your friendship; it means a lot. With you, I always felt supported and never afraid. Thank you also for proofreading part of my thesis; it was an extremely kind gesture.
I wish to express immense gratitude to my PhD companions, Dr Anna Bertolini and Dr Dominik Fuchs. Sharing this experience with you guys was incredible. You were the best mates I could have hoped for.
Anna, grazie per aver condiviso tutto il percorso con me, dal nostro primo giorno, ai festeggiamenti per la fine del probation, la nostra prima volta ai lab. Grazie per essere stata la mia incredibile insegnante di CAT, e per tutto il supporto in analisi, e non solo. Senza il tuo aiuto, questa tesi non avrebbe mai preso questa forma (e magari sarebbe andata persa senza un backup online). Grazie per avermi sempre ascoltata, e mai giudicata. Grazie per essere stata una vera amica. Non so davvero come esprimerti la mia immensa gratitudine, ne dirti quanto io possa sentirmi fortunata ad aver condiviso questo percorso con te. Senza di te non ce l'avrei mai fatta.
Dominik, thanks for being you, my colleague, friend and also my "roommate" for a while. You always made me laugh despite everything and dragged me to crazy and amazing adventures. Thanks for welcoming me from the beginning so openly and introducing me to the Bavarian culture. Thank you for the referee pictures. I could always find them in the strangest places, and they would always make me happy. Thanks for all our shared meals, beers, talks, and walks. It meant the world to me.
Thank you, Dieter, for teaching me so much in the lab, sometimes probably not even realising, and for being the person we could always count on when facing any issues. Working with you is inspiring. Thank you, Franz, for sharing a part of your infinite knowledge with me. Talking with you is an amazing experience, and I am still impressed by the things you know every day. Working with you has been an honour and a privilege, and it has taught me so much.
Thanks to the amazing mounting team of Run37, and a special thanks to Valentyna, for bringing light and laughter to every room, and for the great fundamental expertise, and to the MPP crew: Michele, Bea, Ele and Marco, for all the support and for believing in me more than I did. It was a wonderful experience.
I wish to thank all the proofreaders of this work for keeping up with the not-so-pleasant task of reading and commenting on it: Heerak, Pedro, Alex, Bea, Abhi and, of course, Federica.
Grazie Vanessa, la mia coinquilina/collega. Grazie per aver creato una vera casa a Monaco, con un'atmosfera da famiglia. Non é affatto banale e io ti sarò per sempre grata per questo. Grazie per tutto il tempo passato prezioso passato insieme e per il tuo sorriso sempre presente. Grazie per tutte le chiacchierate, sugli argomenti più disparati, sempre durate ore. Grazie per le discussioni sulla fisica, ho imparato moltissimo da te e ho un mondo ancora da imparare. Sei una grandissima fonte di ispirazione per me, un modello da seguire e una spinta a fare sempre meglio.
Un ringraziamento speciale dal profondo del mio cuore va a tutto il team del Gran Sasso,

per avermi accolto, aiutato e soprattutto supportato durante due campagne di misura fallimentari e per tutto il supporto durante il mounting. Grazie per avermi fatto sentire sempre un po' a casa. Un ringraziamento speciale a Stefano, per la follia condivisa al Test Cryostat, e per tutto il lavoro fatto insieme. Sei una fonte infinita di informazioni, sempre condivise nei modi più divertenti. Grazie Paolo, per la fiducia riposta in me, e per avermi sempre supportato. Grazie anche per aver creato un'atmosfera sempre amichevole e aperta nel gruppo.
Thanks to all the MPP colleagues for the great atmosphere in the office, for making it a fun place to be in, for the sofa fights, ice-creams, coffee breaks, lunches together, parties and all the activities outside. Doing my PhD in this institute has been a great privilege, especially for the atmosphere. There are too many of you to mention everyone, but thank you all. A special thank you to Frank Steffen for making this possible and putting so much effort into this IMPRS school; it is fantastic.

However, these three and a half years of PhD are not only work. Therefore, I would like to thank everyone with whom I shared this path. Thanks to all the people I met in Munich who made me feel more at home and welcomed in this city. A special thanks to David, to Fabi and Alex, and to Bea, Selene and Fulvia (é stato un peccato non avervi conosciuto prima).
Grazie alle mie amiche di sempre, per essermi state accanto e per aver condiviso con me anche questo percorso. Non vi ho mai sentito davvero lontane, nonostante la distanza. Grazie Giulia, per ascoltarmi sempre, e per essere sempre al mio fianco. Grazie per tutte le visite e il tempo prezioso passato insieme. Grazie Ali, perché con te é come se ancora passassimo tutti i giovedì pomeriggio insieme a salvare il cuore delle persone. Non ci sono parole per descriverlo, ma grazie. Grazie Ire, per la sensibilità e per tutte le risate. Grazie Bea, per il tuo spirito libero, per essere sempre una grandissima fonte di ispirazione, per ascoltare sempre senza giudicare mai.

Se penso alle persone che devo ringraziare, però, le prime e più importanti sono la mia famiglia. Grazie a mamma e papà, per aver reso tutto questo possibile. Grazie per aver sempre creduto in me e per avermi permesso di inseguire i miei sogni, é un grande privilegio poterlo fare, lo é ancora di più farlo con tutto il supporto e l'appoggio che mi avete dato voi. Vi sono e vi sarò sempre immensamente grata per questo. Questa tesi é più vostra che mia.
Grazie mamma, per l'amore incondizionato, per avere sempre una parola buona e di conforto. Grazie per l'ascolto e per la mano sempre tesa. Grazie per mostrarmi sempre l'importanza dell'affetto e per non farmelo mai mancare.
Grazie papà, per la tua curiosità e per le mille domande, a cui mi piace sempre cercare di rispondere. Grazie per credere sempre in me, e per avermi insegnato a non mollare mai e ad essere sempre curiosa.
Sorella, che dire, dire grazie a te é complicato, non so se ho le parole per esprimerti quanto ti devo. Grazie per essere la sorella che sei, mi sento estremamente fortunata a condividere con te la mia vita. Grazie perché non mi sento mai davvero sola, perché

tu ci sei sempre. Grazie perché sei la mia roccia, e in qualsiasi momento so di poter contare su di te. E grazie perché sai sempre come farmi tornare a sorridere, a sperare e come spingermi a non mollare e a tirare fuori la grinta. Grazie per tutti i momenti passati insieme, e per quelli passati distanti, ma senza mai sentirti lontana. Mi hai insegnato che la distanza fisica non significa niente, e che si possono sentire vicinissime le persone, nonostante siano fisicamente distanti. Grazie. Sei e sarai sempre la mia più grande fonte di ispirazione, quella persona che guardo e penso "io voglio essere cosi". Grazie ai nonni, che avrei voluto avere accanto in questo momento. Grazie a nonna Malvina, per la sua incredibile forza. Grazie a nonno Gio, per la positività e allegria sopra ogni cosa. Grazie a nonno Chicco, per gli occhi buoni e la matematica dopo scuola. Mi avete insegnato tanto e porterò per sempre delle parti di voi dentro di me. Grazie alla mia famiglia non di sangue, per esserci sempre. Grazie a zia Cinzia, zio Fabio, Dani e Eli. Grazie per le cene, per i Natali, per tutte le feste e per tutti i giorni normali. Siete unici.

Infine, ultimo ma non per importanza, grazie a Fran, per essere la mia casa lontano da casa, la mia casa un po' ovunque. Grazie per essermi stato accanto in questi anni pieni di alti e bassi. Grazie per essere rimasto nonostante i miei momenti di pura follia, grazie per avermi sempre supportato, ascoltato, e soprattutto sopportato. Grazie per non avermi mai permesso di mollare, per la forza che mi hai sempre trasmesso. Grazie per aver portato tantissima luce nella mia vita. Grazie per i nostri incredibili viaggi, per tutto il cibo provato, per tutte le avventure. Grazie per il tuo spirito cosi puro, sempre una grande fonte di ispirazione. Grazie, per spingermi sempre ad essere una persona migliore.